Lib
3/578

Indian J Pure & Appl Phys, Vol 21 No 1 pp 1-68
January 1983
CODEN : IJOPAU ISSN : 0019-5596
21(1) 1-68 (1983)

INDIAN JOURNAL OF PURE & APPLIED PHYSICS

107
3.5.83.

Published by
PUBLICATIONS & INFORMATION DIRECTORATE, CSIR
NEW DELHI
in association with
THE INDIAN NATIONAL SCIENCE ACADEMY, NEW DELHI

"There is only one magic which can remove poverty—and that is hard work helped by a clear sense of purpose and discipline."

—*Indira Gandhi*

Satyameva Jayate—Shramaeva Jayate

Indian Journal of Pure & Applied Physics

EDITORIAL BOARD

Prof. D Basu
Indian Association for the Cultivation of Science
Calcutta

Prof. B Buti
Physical Research Laboratory
Ahmedabad

Prof. S C Dutta Roy
Indian Institute of Technology
New Delhi

Dr R Hradaynath
Instruments Research & Development Establishment Dehra Dun

Prof. D Premaswarup
Nagarjuna University
Nagarjuna Nagar

Prof. A N Mitra
Indian National Science Academy
New Delhi/University of Delhi
Delhi

Prof. Probir Roy
Tata Institute of Fundamental Research
Bombay

Prof. E S Raja Gopal
Indian Institute of Science
Bangalore

Prof. G Rajasekaran
Madras University
Madras

Dr A P B Sinha
National Chemical Laboratory
Pune

Prof. C V Vishveshwara
Raman Research Institute
Bangalore

Prof. M S Sodha
Indian National Science Academy
New Delhi/Indian Institute of Technology New Delhi

Shri Y R Chadha, *Ex-officio* Secretary & Chief Editor

EDITORIAL STAFF

Editors

D S Sastry, K S Rangarajan & R P Goel

Assistant Editors

G N Sarma, J B Dhawan & Tarun Banerjee

Scientific Assistant

(Mrs) Poonam Bhatt

Published by the Publications & Information Directorate, CSIR, Hillside Road, New Delhi 110012
Chief Editor: Y R Chadha

The Indian Journal of Pure & Applied Physics is issued monthly. The Directorate assumes no responsibility for the statements and opinions advanced by contributors. The editorial staff in its work of examining papers received for publication is assisted, in an honorary capacity, by a large number of distinguished scientists, working in various parts of India.

Communications regarding contributions for publication in the journal should be addressed to the Editor, Indian Journal of Pure & Applied Physics, Publications & Information Directorate, Hillside Road, New Delhi 110012.

Correspondence regarding subscriptions and advertisements should be addressed to the Sales & Distribution Officer, Publications & Information Directorate, New Delhi 110012.

Annual Subscription	**Single Copy**
Rs. 120.00 £20.00 $45.00	Rs. 12.00 £2.00 $4.50

50% Discount is admissible to research workers and students and 25% discount to non-research individuals, on annual subscription. Payments in respect of subscriptions and advertisements may be sent by cheque, bank draft, money order or postal order marked payable *only* to **Publications & Information Directorate, New Delhi 110012.** Claims for missing numbers of the journal will be allowed only if received within 3 months of the date of issue of the journal plus the time normally required for postal delivery of the journal and the claim.

© 1983 The Council of Scientific & Industrial Research, New Delhi.

Indian Journal of Pure & Applied Physics

VOLUME 21 NUMBER 1 JANUARY 1983

CONTENTS

Solid State Physics

Effect of Trichloroethylene (TCE) Molar Concentration on the Storage Time of MOS Capacitors ... 1
A B Bhattacharyya, L Manchanda & J Vasi*

Electronic & Ionic Processes Occurring in KBr & KI Crystals during Electrolytic Coloration 6
M L Dalal*, S Sivaraman & Y V G S Murti

Chemical Physics

Appearance Energies of Fragment Ions from Cyclohexanone ... 11
Ezzat T M Selim* & M A Rabbih

Vibrational Analysis of Some Linear Symmetrical Metal Dihalide Ions ... 16
B Mohan Srinivasan & R Ramasamy*

Nuclear Physics

The Decay of ^{125}Sb ... 19
K Singh & H S Sahota*

Theoretical & Mathematical Physics

Non-Abelian Gauge Theory of Fields Associated with Dyons ... 25
B S Rajput & Satya Raj Kumar*

Study of Emission of Cerenkov Radiation by Tachyons ... 28
O P S Negi* & B S Rajput

Regge Poles in the Klein-Gordon Equation ... 33
Anuradha Bhargava & L K Sharma*

Electronics

Theory of Open Circuit Voltage Decay in a *p-n* Junction Device ... 36
V K Tewary* & S C Jain

Optics

Scatter Plate Interferometer for Aspherical Surfaces ... 39
M V R K Murty & R P Shukla*

NOTES

Normal Coordinate Analysis & Thermodynamic Functions of Chloromethyl Formate 44
R Prasad*

Effect of Temperature on Dielectric Relaxation Time in Lutidines at Microwave Frequency 47
Om Vir Singh*

Studies on the Metal-Ligand Equatorial & Axial Bond Strengths in Some Copper(II) Complexes of 1-3-Diaminopropane by ESR Technique ... 49
G Ponticelli, M M Ahmed, B A Sastry*, S Md Asadullah & P Satyanarayana

Calculations of the Total Stopping Power of Positrons in Various Absorbers—Proposed Empirical Equation ... 52
S K Gupta, O P Varma, D K Gupta* & R K Tyagi

Electronic & Vibrational Spectra of 3-Amino-2-chloropyridine ... 56
Nitish K Sanyal*, S L Srivastava & (Mrs) Ananda Devi

Continued overleaf

CONTENTS

Laser Raman & Far Infrared Spectra of DL-Phenyl Alanine 59
Vinaya Kumar & P K Verma*

Electronic Absorption Spectrum of 2-Chloro-6-Methyl-Benzonitrile in Vapour Phase... 61
R K Goel*, S K Sharma & S N Sharma

Ellipsometric Determination of the Distribution of Particles in a Residual Layer ... 63
J Ashok* & P L Vara Prasad

Ultrasonic Velocity in Binary Liquid Mixtures: *m*-Xylene, *o*-Xylene, CCl_4 & Toluene in Nitrobenzene 65
S N Jajoo*, V S Deogaonkar & C S Adgaonkar

Ultrasonic Velocity & Adiabatic Compressibility of Triphenyltin Chloride in Acetone at Various Temperatures 67
T N Srivastava*, R P Singh & Bhagwan Swaroop

---

*The author to whom all correspondence is to be addressed is indicated by the (*) mark.

Indian Journal of Pure & Applied Physics
Vol. 21, January 1983, pp 1-5

Effect of Trichloroethylene (TCE) Molar Concentration on the Storage Time of MOS Capacitors

A B BHATTACHARYYA, L MANCHANDA & J VASI*
Centre for Applied Research in Electronics, Indian Institute of Technology, New Delhi 110016

Received 3 *October* 1981; *revised received* 8 *November* 1982

The TCE process has been optimized at 1100°C for maximum storage time. Capacitance versus time plots of MOS capacitors fabricated with different TCE concentrations have been analyzed using the Zerbst method with a suitable modification. This modified technique has been used to scan the bulk lifetime in the depletion region very close to the Si-SiO_2 interface. These bulk lifetime measurements show that a large TCE concentration not only affects the surface of the silicon, but also affects the bulk of the silicon near the interface. These results have been further supported by scanning electron microscope observations of the silicon surface after oxidation.

1 Introduction

It is well known that many high-temperature processing steps in silicon device fabrication result in a decrease of minority carrier lifetime in silicon. This increases the thermal generation rate of carriers in the depletion region of MOS devices and *p-n* junctions. The thermal generation rate is of crucial importance in MOS-based structures such as charge-coupled devices where it directly affects the characteristic parameter known as the storage time. The addition of trichloroethylene (TCE), like other chlorine compounds, during the oxidation results in improved storage times of MOS capacitors[1-9]. It has also been shown that the storage time of MOS capacitors varies significantly with the molar concentration of TCE in the oxygen flow during the growth of the oxide[1]. The addition of small amounts of TCE improves the storage time, whereas large concentrations of TCE reduce the storage time. The mechanism of this variation in storage time has not yet been investigated in detail.

In this paper, we present some results on process optimization for maximum storage time of MOS capacitors fabricated with TCE. We have analyzed capacitance versus time (*C-t*) plots of MOS capacitors fabricated with different molar concentrations of TCE. This analysis has been done using the Zerbst method with a suitable modification[10,11]. This modified Zerbst technique has been used to find the spatial variation of bulk generation lifetime near the interface of MOS capacitors and to explain the variation of storage time. Some experiments have also been performed to separate bulk and surface effects on the MOS capacitor storage times.

2 Theory

The Zerbst analysis is a commonly-used technique for the determination of generation lifetime using MOS capacitance transients[10]. The capacitance of a pulsed MOS capacitor is measured as a function of time, and the quantity $(-qN_D\varepsilon_s/n_iC_{ox})d(C_{ox}/C)^2/dt$ is plotted as a function of $(C_F/C-1)$ or $(W-W_F)$, resulting in the so-called Zerbst plot. Here, N_D is the doping density, n_i the intrinsic concentration, ε_s the dielectric constant of silicon, C_{ox} the oxide capacitance, W the depletion width corresponding to capacitance C at any time t, and W_F the final inversion depletion width corresponding to the inversion capacitance C_F. If the generation lifetime (τ) is constant, the Zerbst plot is a straight line whose slope is inversely proportional to τ. If τ varies with distance from the Si-SiO_2 interface in the silicon, the Zerbst plot is not a straight line. Recently, Manchanda *et al.*[11] have modified the Zerbst technique to compute the variation of lifetime τ with distance. They have shown that the lifetime at a distance $W-W_F$ in the silicon from the Si-SiO_2 interface is proportional to the inverse of the slope of the Zerbst plot at a value $W-W_F$.

In the above modification, the effective generation width had been assumed to be equal to $W-W_F$. This assumption does not have any theoretical basis, but is based simply on the observation that, in equilibrium, the depletion width becomes W_F and the net generation is zero. Recently it has been shown by Rabbani and Lamb[12] that $W-W_F$ underestimates the effective generation width and they have suggested a new value for the effective generation width (W_g) given by:

$$W_g=\sqrt{W^2-(W_F^2/2)}-W_F/\sqrt{2} \qquad \ldots(1)$$

With the above value of W_g, the total generation rate G can be written as

$$G=\int_0^{W_g}\frac{n_i}{2\tau[x+W-\sqrt{W^2-(W_F^2/2)}]}dx \qquad \ldots(2)$$

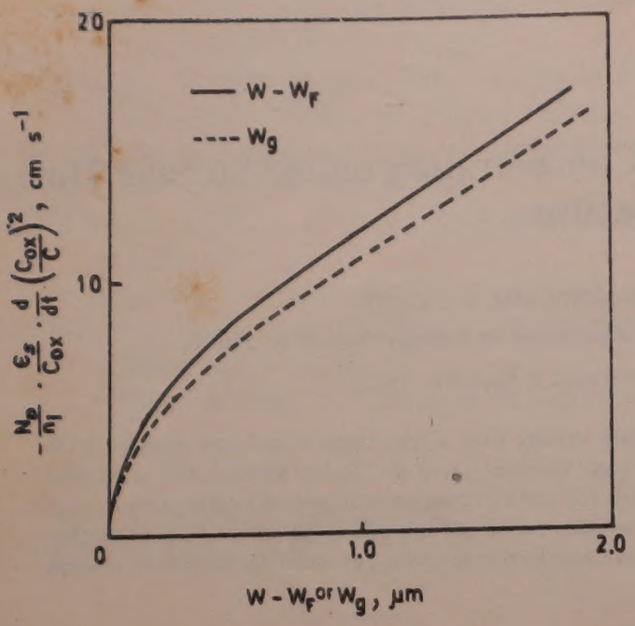

Fig. 1(a)—Zerbst plots with respect to effective generation widths $W - W_F$ and W_g

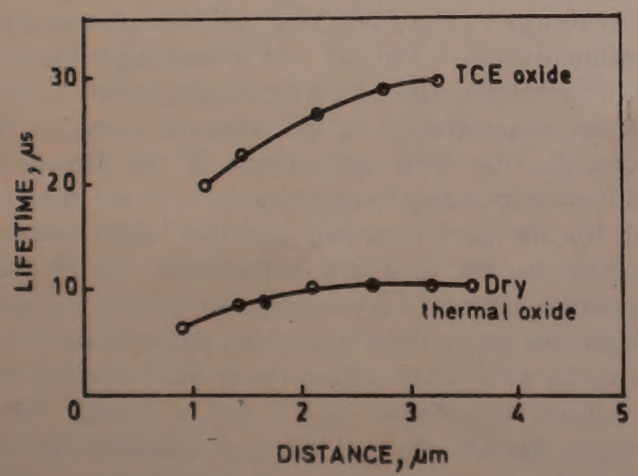

Fig. 1(b)—Minority carrier lifetime versus distance from the Si-SiO_2 interface

Differentiating with respect to W_g we obtain

$$\frac{dG}{dW_g} = \frac{n_i}{2\tau[W - (W_F/\sqrt{2})]} \quad \ldots(3)$$

This shows that if G is plotted as a function of W_g, the slope of this curve at any value of W_g is inversely related to the bulk lifetime at a distance $W - (W_F/\sqrt{2})$ from the Si-SiO_2 interface. Fig. 1(a) shows Zerbst plots with respect to $W - W_F$ and with respect to W_g. This new effective generation width affects the slope variation of the Zerbst plot for small values of W. We have used this new Zerbst method rather than the one developed earlier[11] for the computation of the spatial variation of bulk lifetime near the Si-SiO_2 interface of MOS capacitors. Fig. 1(b) shows the spatial variation of bulk lifetime for MOS capacitors fabricated with dry thermal oxide and TCE oxide.

3 Fabrication and Measurement of Storage Time of Capacitors

It is known that the electrical properties of MOS capacitors fabricated with TCE oxides are significantly dependent on the molar concentration of TCE used during the growth of the oxide. The optimum TCE molar concentration may be different for the various improvements such as increase of storage time, degree of passivation, and decrease in interface state density. We have optimized this process for maximum storage time. In this section, we describe the fabrication process of MOS capacitors and measurement of storage time of these capacitors.

For optimization purposes, oxides were grown on (100) *n*-type 1-10 ohm-cm CZ silicon wafers obtained from Monsanto. The wafers were cleaned following standard cleaning procedures[13]. A double-wall quartz tube system was used for dry thermal oxidation (oxidation in pure O_2). TCE oxidation was done in the same system but without the double-wall action. For TCE oxidation, electronic grade TCE at 20 ± 0.5°C was used as the source. Nitrogen was used as the carrier gas for TCE and this was mixed with oxygen at the inlet of the oxidation tube.

All oxidations were done at 1100°C. For TCE oxidation, for the first 5 min, oxidation was done in pure O_2 only, since chlorine can etch the silicon surface thereby forming etch pits. The thin oxide so grown prevents chlorine from coming directly in contact with silicon. After this, TCE was added to the oxygen and oxidation continued for another 40 min. The TCE concentration was varied from 0.17% to 1.00% by changing the N_2 flow rate from 20 cc/min to 140 cc/min through the bubbler containing TCE, and this was added to 1000 cc/min flow of O_2. All these oxides were annealed *in situ* for 15 min in N_2 at the same temperature. After this, aluminium evaporation was done through a metal mask. The wafers were then annealed in N_2 for 15 min at 450°C for reduction of interface-state density. The thickness of the oxide grown was calculated from the accumulation capacitance. For this purpose, the electrodes were defined with photolithography to get a well-defined area. The thickness of SiO_2 for different TCE molar concentrations varied from 950 Å to 1250 Å.

The transient capacitance technique essentially consists of the application of a deep depleting voltage step to a MOS capacitor initially biased in accumulation or inversion and recording the capacitance as a function of time. For a given pulse height, the time taken by the capacitor to go from deep depletion to the final inversion state is known as the storage time. For the *C-t* measurements, a PAR 410 *C-V* plotter was used, and the transient capacitance variation plotted on an x-y recorder.

4 Results and Discussion

Optimum TCE concentration—To determine the optimum TCE flow for maximum storage time, capacitance versus time measurements were performed with a 0 to −15 V pulse applied to the capacitor. There was a large variation of storage time observed across the wafer. Measurements were done on about 50 capacitors on each wafer. Because of the large variation in storage time across the wafer, histograms were plotted for fraction of capacitors versus the storage time interval. The time interval corresponding to the maximum fraction of capacitors (peak position) was taken as a measure of storage time on the wafer. Fig. 2 shows the histograms of storage time variation for dry thermal oxide and 0.5% TCE oxide. The addition of TCE not only shifts the peak position, but also improves the maximum storage time. Fig. 3 shows the variation of storage time interval corresponding to peak position in the histogram versus the TCE molar concentration during the oxidation. This shows that

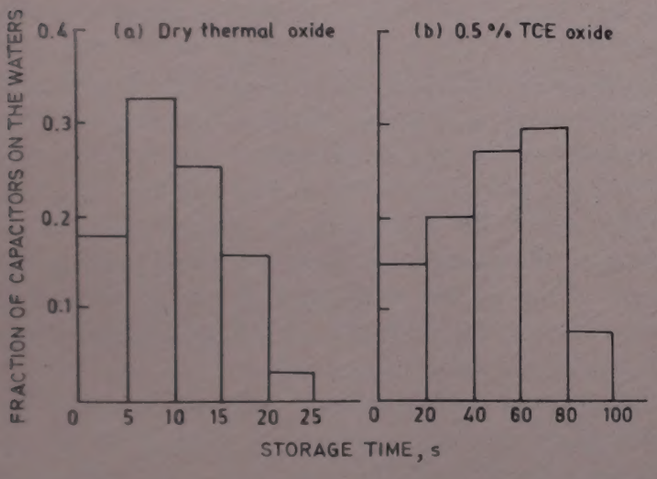

Fig. 2—Histograms showing the variation of storage time of MOS capacitors. (a) Dry thermal oxide (b) 0.5% TCE oxide

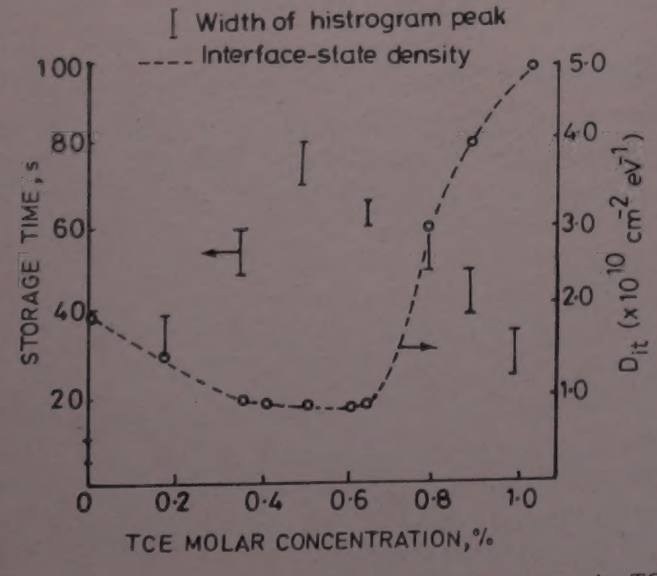

Fig. 3—Storage time and interface-state density versus the TCE molar concentration

0.5% molar concentration of TCE in O_2 gives the maximum storage time for oxidation at 1100°C. The interface-state density was also measured on capacitors fabricated with different molar concentrations of TCE. The interface-state density D_{it} was determined using the quasistatic technique[14]. The dotted line in Fig. 3 shows the variation of D_{it} at the middle of the band-gap. For 0.5% TCE, the interface-state density is minimum ($< 10^{10}$ $cm^{-2}eV^{-1}$).

The spatial variation of bulk lifetime—As seen from Fig. 3, the addition of small amounts of TCE improves the storage time, the maximum being observed for 0.5% molar concentration of TCE. The interface-state density varies from 2×10^{10} $cm^{-2}eV^{-1}$ to 5×10^{10} $cm^{-2}eV^{-1}$ at the middle of the band-gap, with the minimum again at 0.5% TCE. It is possible that surface generation via the interface states is responsible for the variation in storage time. However, it can be shown[13] that interface-state densities as large as 5×10^{11} $cm^{-2}eV^{-1}$ reduce the storage time by less than 10%, which is much smaller than the observed variation in storage time. Therefore, the variation seems to be due to the effect of TCE on the bulk of silicon near the interface.

It is well known that the addition of TCE quenches stacking faults, getters their nuclei and also getters metallic impurities, so the improvement for small TCE concentration can be ascribed to the reduction in the density and size of stacking faults and also to the gettering of metallic impurities[15-18]. But these two factors cannot explain the reduction of storage time for TCE concentrations larger than 0.5%. Large concentrations of TCE should getter more metallic impurities. We observed that the stacking fault density and length also reduced for 1% TCE oxide. The stacking fault length was approximately 4 μm for 0.5% TCE oxide and approximately 2 μm for 1% TCE oxide, and the stacking fault density was also less for the latter. Therefore, large concentrations of TCE seem to be affecting the bulk of the silicon near the surface. After removing the oxides, we observed the surface of silicon with a scanning electron microscope. As shown in Fig. 4, the surface is quite smooth for 0.5% TCE oxide, but there are etch pits on the surface for the 1% TCE oxide. These etch pits, which make the surface rough, seem to be responsible for the reduction of storage time.

This was confirmed by scanning the bulk lifetime across the depletion width of MOS capacitors fabricated with dry thermal oxide, 0.5% TCE oxide and 1% TCE oxide. Fig. 5 shows the three Zerbst plots. These plots have been constructed from *C-t* plots obtained by pulsing the capacitor from inversion to deep depletion to minimize the effect of interface states. The Zerbst plot (b) for 0.5% TCE is more linear,

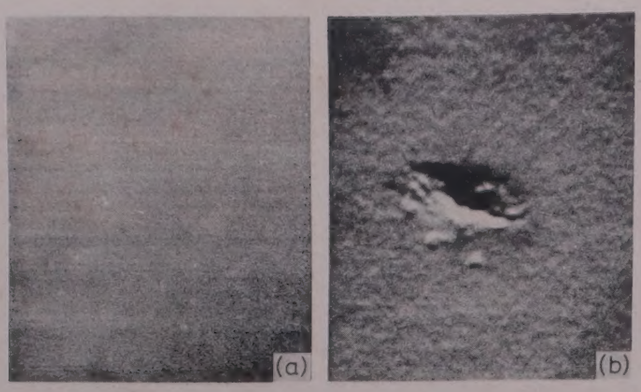

Fig. 4(a)—SEM micrograph of silicon surface after etching the 0.5% TCE oxide (magnification × 2000)

Fig. 4(b)—SEM micrograph of silicon surface after etching the 1% TCE oxide (magnification × 13000)

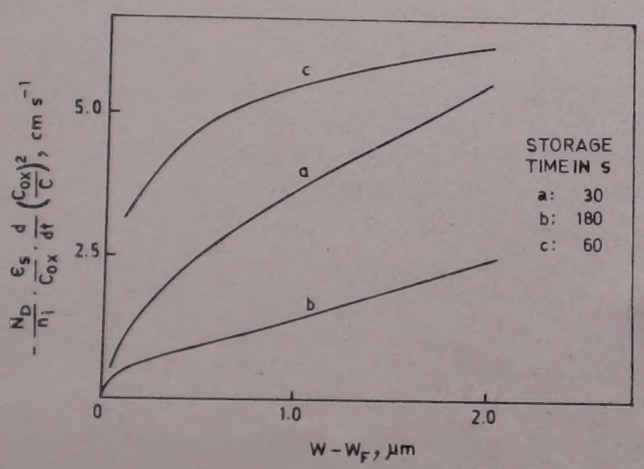

Fig. 5—Zerbst plots for MOS capacitors fabricated with (a) dry thermal oxide, (b) 0.5% TCE oxide, and (c) 1% TCE oxide

whereas the Zerbst plot (c) for 1% TCE oxide is more nonlinear compared to that for dry thermal oxide (a). There is a large change in the slope for the first 0.5 μm from the Si-SiO_2 interface for 1% TCE oxide, indicating that in this region there is a large reduction of lifetime, whereas deep into the bulk, the lifetime is even slightly larger than that for 0.5% TCE oxide as indicated by the smaller slope of the Zerbst plot. These results show that the addition of a small amount of TCE improves the bulk lifetime near the interface (as can be seen from the slopes of curves a and b), whereas a very large concentration of TCE seems to be degrading the silicon quality very close to the interface, although deeper into the bulk, the lifetime is high. The Zerbst plot for 1% TCE oxide gives the impression of large surface generation, although it is from a C-t plot obtained by pulsing a capacitor from inversion to deep depletion.

The following experiments were performed to check whether this is an interface or a bulk effect. As seen from Eq. (1), the minimum distance from the Si-SiO_2 interface where the bulk lifetime can be measured is

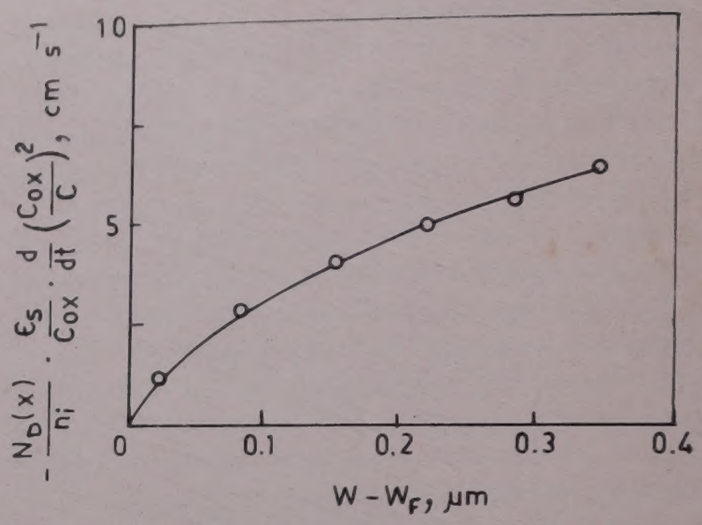

Fig. 6—Zerbst plot of a MOS capacitor fabricated with 1% TCE oxide grown on a low resistivity (0.1-0.5 ohm-cm) wafer

$W_F/\sqrt{2}$. If W_F is small, the bulk lifetime can be scanned for small values of depletion width. In order to obtain small values of W_F, MOS capacitors were fabricated on low resistivity (0.1-0.5 ohm-cm) silicon. Oxidation was done with 1% TCE. Fig. 6 shows the Zerbst plot with doping variation taken into account. The Zerbst plot does *not* show a large intercept, indicating that the variation in Fig. 5(c) is probably due to the small lifetime of carriers near the interface. Both the plots show a large value of slope in the first 0.4 μm near the interface. We cannot compare the magnitude of the slopes of the Zerbst plots (and therefore the actual values of lifetime) shown in Figs 5(c) and 6 because two different wafers have been used.

Therefore it seems that the etch pits observed by scanning electron microscopy are responsible for the reduction of lifetime in the first 0.5 μm region of silicon near the interface. The increase in the interface-state density at large TCE concentrations is also likely to be due to the roughening of the surface by the etch pits.

Acknowledgement

The partial financial support of the Department of Electronics, Government of India, New Delhi, during this work is acknowledged.

References

1 Declerck G J, Hattori T, May G A, Beaudouin J & Meindl J D, *J Electrochem Soc (USA)*, **122** (1975) 436.

2 Grabbs W H, Das M B, Stach J & Tressler R E, *150th Meeting of the Electrochem Soc, Las Vegas*, 1976, Abstract No. 325.

3 Singh B R & Balk P, *J Electrochem Soc (USA)*, **125** (1978) 453.

4 Monkowski J, *Solid-State Technol (USA)*, **12** (July) (1979) 58.

5 Monkowski J, Tressler R E & Stach J, *Thin Solid Films (Switzerland)*, **65** (1980) 153.

6 Robinson P H & Heiman F P, *J Electrochem Soc (USA)*, **118** (1971) 141.

7 Scot C R, *Solid-State Technol (USA)*, **22** (May) (1978) 80.

8 Janssens E J & Declerck G J, *J Electrochem Soc (USA)*, **125** (1978) 1696.

9 Wang K L & Connery R J, 152*nd Meeting of the Electrochem Soc, Washington*, 1978, Abstract No. 264.

10 Zerbst M, *Z Agnew Phys (Germany)*, **22** (1966) 30.

11 Manchanda L, Vasi J & Bhattacharyya A B, *Solid-State Electron (UK)*, **23** (1980) 1015.

12 Rabbani K S & Lamb D R, *Solid-State Electron (UK)*, **21** (1978) 1171.

13 Manchanda L, *The effect of trichloroethylene on electronic properties of Si-SiO_2 structures*, Ph D thesis, Indian Institute of Technology, Delhi, 1980.

14 Kuhn M, *Solid-State Electron (UK)*, **13** (1970) 873.

15 Hattori T, *J Electrochem Soc (USA)*, **123** (1976) 945.

16 Hattori T, *Appl Phys Lett (USA)*, **30** (1977) 312.

17 Monkowski J, *Solid-State Technol (USA)*, **22** (August) (1979) 113.

18 Hattori T, *Solid-State Technol (USA)*, **22** (November) (1979) 85.

Indian Journal of Pure & Applied Physics
Vol. 21, January 1983, pp 6-10

Electronic & Ionic Processes Occurring in KBr & KI Crystals during Electrolytic Coloration

M L DALAL*, S SIVARAMAN† & Y V G S MURTI‡

Received 22 December 1981; revised received 22 July 1982

The processes occurring in KBr and KI crystals during electrolytic coloration have been studied. The dependence of the current density and temperature of electron injection on applied electric field has also been investigated. It is concluded that the start of electron injection and hence of coloration does not depend on applied voltage or the current, and that a certain minimum amount of charge is to be transported to and deposited on the pointed cathode for the initiation of the electron injection.

1 Introduction

Since the early work of Pohl and his group[1-3] at Göttingen, not much work has been done on the problem of electrolytic coloration of alkali halides. The evolution of the electrical current through the alkali halide crystals during the process of electrolytic coloration has been studied by Koikov *et al.*[4], Heiland[2] and Montojo and Sanchez[5]. It has been known for quite sometime that the evolution of current (and colour centres) through the crystal during electrolytic coloration exhibits four zones or stages as a function of time[4,5]. Zone I is due purely to the ionic transport and there is no contribution of electronic current[4,5]. Zone II corresponds to the electron injection from the cathode into the crystal.

In agreement with the views of Heiland[2], Uchida and Nakai[6], Hadley[7], Paramo and Sanchez[8] assumed that due to the ionic transport in the crystal, a new alkali metal cathode is formed and the electrons emitted from this new cathode are injected into the crystal and migrate towards the anode. In order to gain more insight into the nature of the physical phenomena taking place during electrolytic coloration, the present work was undertaken.

2 Experimental Procedure

KI and KBr crystals employed for the present study were grown by the Czochralski technique using Sarabhai M Merck G R grade materials. Small pieces ($\sim 10 \times 5 \times 4$ mm^3) were cleaved from a single bulk crystal.

A cleaved crystal was placed between a pointed platinum cathode and a flat platinum anode. The electric field applied across the crystal was kept on throughout the experimental run. The crystal was heated linearly at a constant rate (the respective heating rates are plotted with the current) and the current was recorded simultaneously using a Servogor 2-pen recorder. The temperature was monitored by a thermocouple placed in a small cavity made in the stainless steel anode head very near to the crystal. With this arrangement, the difference in temperature between the faces was less than 5°C at elevated temperatures (of the order of 700°C). Different specimens were used for each run.

3 Results

Figs 1 and 2 represent the characteristic dependence of current density J on time t for KI crystals. The applied field ranges from 53 to 402 V/cm and the heating rate varies from 5.1 to 7.1 K/min. It can be seen that the current remains constant for quite sometime and then suddenly starts rising sharply. The constant current region corresponds to zone I. The point I of sudden rise in current can be considered as the onset of the electron injection and hence of colour centre creation in the crystal. Before this point the crystal is found completely transparent but no longer remains so after the current starts rising. As shown in Figs 1 and 2, the length of the constant current region decreases as the applied voltage increases.

Similar results are obtained for KBr crystals. Figs 3 and 4 describe the behaviour of J versus t for KI and KBr crystals respectively, and the corresponding heating rates are also shown. The applied field in this case ranges from 47 to 597 V/cm whereas the heating rate lies between 5.6 and 8.9 K/min. It can be seen from Figs 3 and 4 that as the voltage applied across the crystal increases the time required for the start of electron injection decreases. It can be noticed from Figs 1-4 that all the curves possess, in general, the same

*Physics Department, S N Govt P G College, Khandwa 450001
†Physics Department, University of Saugar, Sagar 470003
‡Physics Department, Indian Institute of Technology, Madras 600036

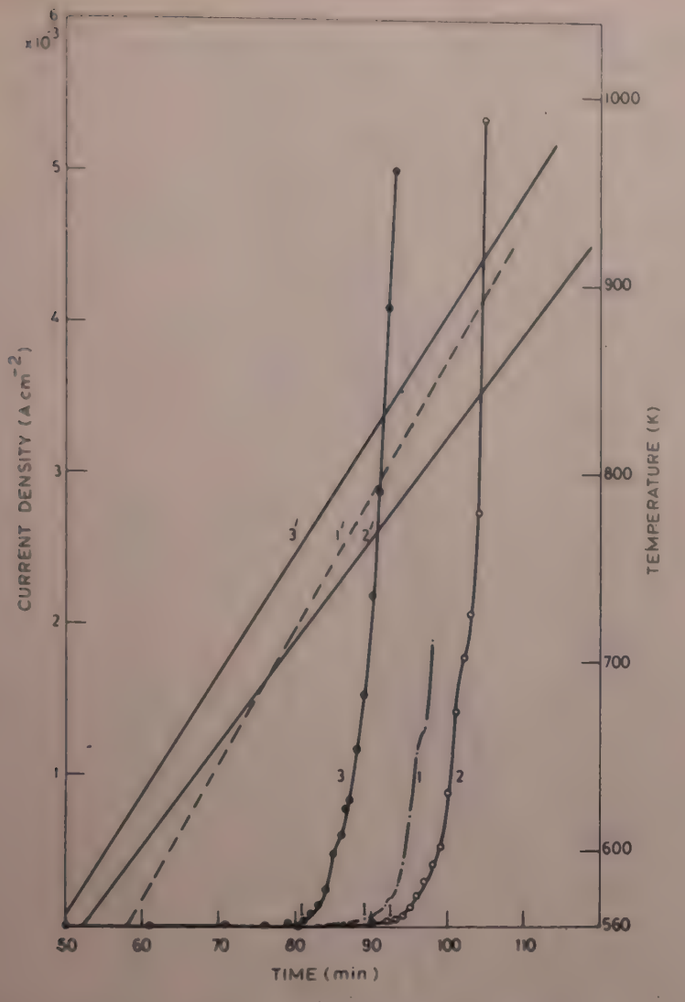

Fig. 1—Evolution of electrical current density through KI crystals when heated linearly from room temperature

Curve No.	Field (E) V/cm	Curve No.	Corresponding heating rate (β) K/min
1	53	1′	7.1
2	74	2′	5.5
3	104	3′	6.4

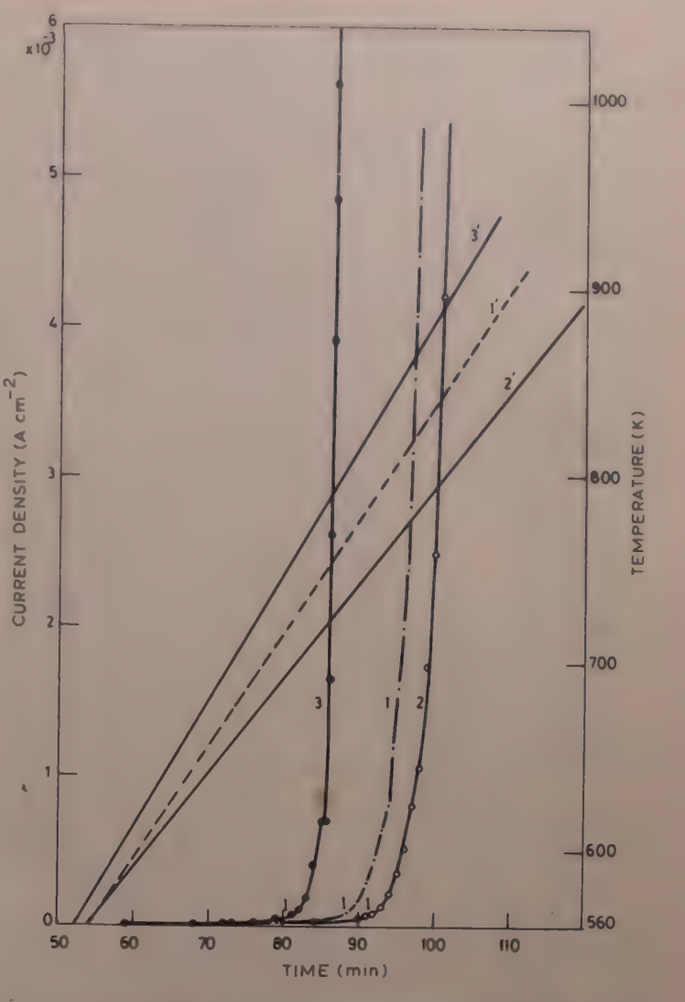

Fig. 2—Evolution of electrical current density through KI crystals when heated linearly from room temperature

Curve No.	Field (E) V/cm	Curve No.	Corresponding heating rate (β) K/min
1	162	1′	6.1
2	256	2′	5.1
3	402	3′	6.8

shape and structure, irrespective of the voltage applied, for both KI and KBr.

4 Discussion

4.1 Dependence of T_I on E

Fig. 5 shows the dependence of the temperature of electron injection (T_I), i.e., the temperature at which coloration starts, on the electric field (E) applied across the crystal. It can be seen that for low fields T_I is higher for KBr than for KI for the same field value, but at high fields T_I is less in the case of KBr than in KI. Paramo and Sanchez[8] have found that, for all field values, T_I is always less in KI than in KBr (when compared for the same field). This observed discrepancy can be explained as follows. Since the start of electron injection, and hence of coloration, depends on several factors like the transport of charges by ions and their concentration, nature of the background impurities and the characteristics of the pointed electrode, these factors may alter the temperature of injection. We believe that the discrepancy is on account of impurities.

As far as the fixation of the lowest limit of applied electric field is concerned, it should be mentioned here that the injection of electrons does not depend solely on the applied field but a certain amount of charge transfer to the pointed cathode is essential.

4.2 Dependence of ET_I on $1/T_I$

According to Ref. 8.

$$C_I \propto ET_I e^{-w/kT_I}$$

or $$ET_I \propto C_I e^{w/kT_I}$$

where C_I is the concentration of potassium ions accumulated at the pointed cathode at temperature T_I. The plot of $\ln(ET_I)$ versus $1/T_I$ should be linear. Our present results on KI and KBr show such a behaviour

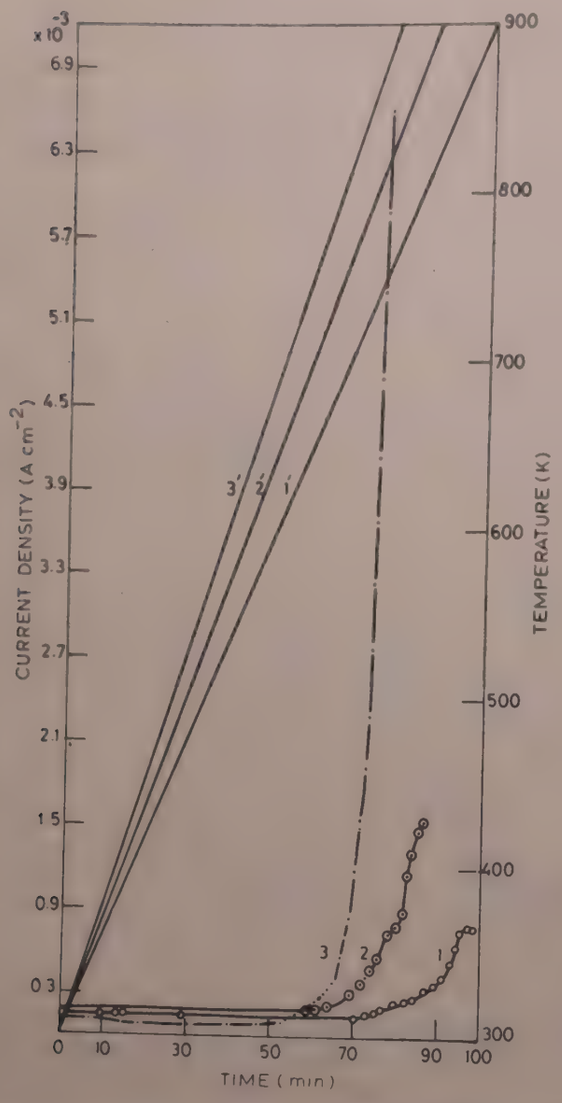

Fig. 3—Evolution of electrical current density through KBr crystals when heated linearly from room temperature

Curve No.	Field (E) V/cm	Curve No	Corresponding heating rate (β) K min
1	47	1	6.0
2	65	2	7.0
3	94	3	7.7

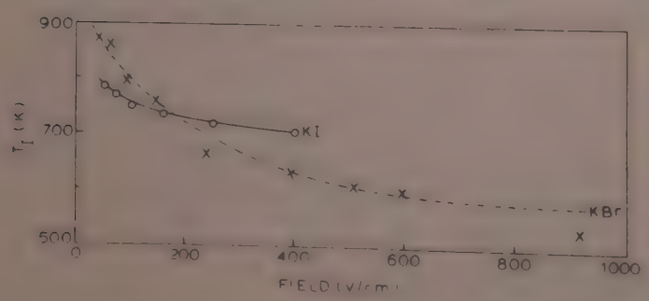

Fig. 5—The variation of temperature of injection T_I (at which coloration starts) as a function of applied field E

as shown in Fig. 6. The activation energy (W) comes out to be 1.16 and 0.79 eV for KI and KBr respectively, quite different from the values obtained by Paramo and Sanchez[8] as 0.84 and 0.66 eV respectively for the two cases. This is understandable since the activation

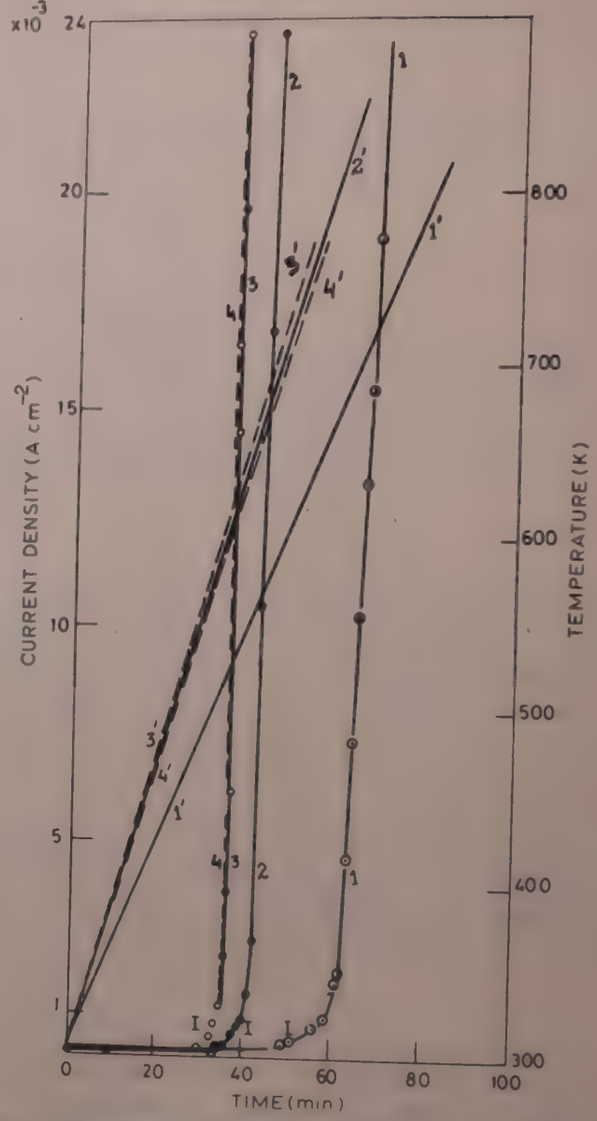

Fig. 4—Evolution of electrical current density through KBr crystals when heated linearly from room temperature

Curve No.	Field (E) V/cm	Curve No.	Corresponding heating rate (β) K min
1	238	1′	6.2
2	393	2′	8.6
3	509	3′	8.9
4	597	4′	8.5

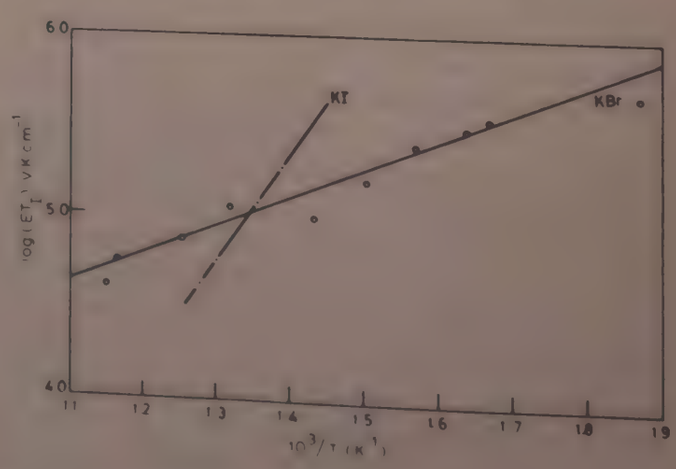

Fig. 6—Relationship between $\log(ET_I)$ and $10^3/T$ [The experimental values of E and T_I are taken from Fig. 5]

energy involved is that corresponding largely to extrinsic ionic conductivity region of the crystal which is known to be considerably structure-sensitive. The values of W obtained in the present work are larger than the cation vacancy migration energies h_m (0.63 and 0.65 eV in KI and KBr respectively) possibly because of the role of impurity-vacancy association. It may be mentioned that in the event of near complete association of such complexes, the activation energy for conductivity in the extrinsic domain will be nearly given by $(h_m + \frac{1}{2}h_a)$ where h_a is the binding enthalpy of the impurity-vacancy pairs.

4.3 Relationship between J_I and E

The variation of electron injection current density (J_I) as a function of E is shown in Fig. 7. It is seen that for both KI and KBr the injection current decreases as the field increases. It can be seen further that the J_I values in the case of KBr are higher than in KI. Paramo and Sanchez[8] observed just the opposite result. The main factor affecting the current, as discussed in Sec. 4.2, may be the background impurities.

The reduction in J_I due to an increase in E suggests that neither the current nor the applied field is responsible for the electron injection or the coloration, but only the density of charges accumulated at the pointed cathode. Along with the results described in Sec. 4.1, the results discussed in this section are suggestive of the requirement of a minimum charge accumulation at the cathode for the coloration.

4.4 Thermionic Emission

If the hypothesis, that a new alkali metal cathode is formed at the pointed cathode due to the transport of the ions and that electrons are injected from this new cathode into the crystal because of thermionic emission, is true, then the well known Richardson-Dushman equation must be obeyed.

To test the validity and relevance of the Richardson-Dushman equation in the present work, a plot of $\ln[(\Delta J/T_I^2)/E]$ versus $10^3/T$ is made. It is observed that KI conforms in a better way than KBr, which shows a considerable scatter in the experimental values. The values of the work function (φ) obtained in the present work from least-squares fit are 2.84 and 1.43 eV for KI and KBr respectively. The φ value for KBr agrees well with that of Paramo and Sanchez[8] (1.53 eV). On the other hand, the value of φ obtained in the present work for KI is much higher than the reported values[8].

4.5 Necessary Condition for Electron Injection into Crystals

Table 1 shows the amount of charge and the number of cations transported to the pointed cathode as obtained in the present work. It can be seen that the number of cations (potassium ions) transported to the cathode during zone I (from $t = 0$ to $t = t_I$) is observed to be of the order of 5.62×10^{17} and 3.17×10^{18} for KI and KBr crystals respectively. These values are obtained by calculating the area under the current-time curve from $t = 0$ to $t = t_I$, the time at which the injection of electrons starts. The curves chosen for the estimation of charge were recorded at 53, 74, 104, 162, 256 and 402 V/cm for KI crystal, whereas those for KBr were recorded at 47, 65, 94 and 143 V/cm. It can be noticed that more number of cations are necessary to reach the cathode in the case of KBr than in KI. This explains why a higher temperature is needed to colour KBr electrolytically than KI. The values obtained by Montojo and Sanchez[5] in KBr are also included in Table 1.

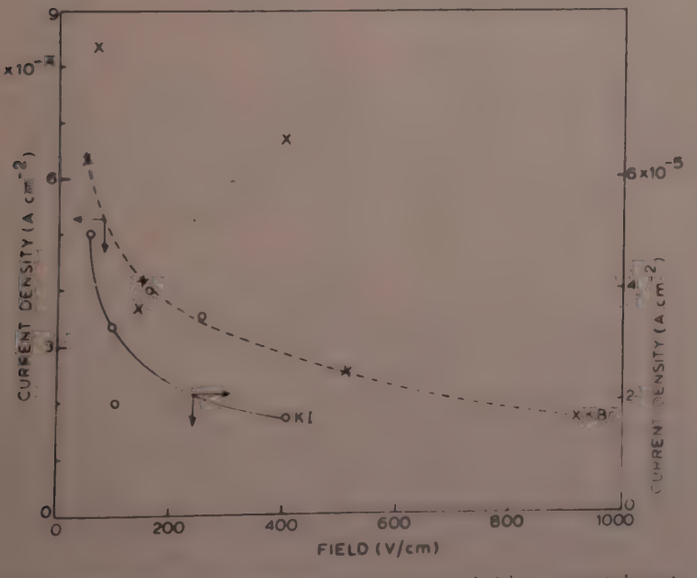

Fig. 7—Relationship between current density J_I (the current density at point I) and the applied field E [(a) and (b) refer to the LHS and RHS scales respectively]

Table 1—Charge Transported to the Pointed Cathode

Crystal	Charge $Q = \int_{t=0}^{t=t_I} I\,dt$ A.sec	Average Q A.sec	Average No. of cations transported to cathode $n = Q/e$	Author
KI	0.10			
	0.09			
	0.08			
	0.11	0.09	5.62×10^{17}	Present work
	0.11			
	0.06			
KBr	0.54			
	0.54			
	0.39	0.50	3.12×10^{18}	Present work
	0.54			
KBr		0.34×10^{-4}	2.12×10^{14}	Montojo and
		0.40×10^{-4}	2.52×10^{14}	Sanchez

5 Conclusion

The above discussion of the results obtained in the present work leads us to the plausible conclusion that neither the voltage nor the current is a decisive factor for the start of electrolytic coloration. On the other hand a necessary amount of charge is to be transported to and deposited on the pointed electrode in order to initiate electrolytic coloration.

Acknowledgement

One of the authors (MLD) expresses his gratefulness to the University Grants Commission, New Delhi for sponsoring him as a teacher research fellow under the Faculty Improvement Programme, and to the Education Department of the Government of Madhya Pradesh for financial support. Thanks are also due to Prof. C Ramasastry and Prof. R Srinivasan, Heads of the Department of Physics, Indian Institute of Technology, Madras, for their respective terms, for allowing to use their facility and for the interest shown by them in the work.

References

1 Pohl R W, *Proc Phys Soc London (GB)*, **49** (1937) 3.
2 Heiland G, *Z Phys (Germany)*, **128** (1950) 144.
3 Uchida Y, Ueta M & Nakai Y, *J Phys Soc Jpn (Japan)*, **6** (1951) 107.
4 Koikov S N, Semushkin G B & Tsikin A N, *Collection: The physics of dielectrics and semiconductors*, Tr. LPI, Leningrade (1967) as cited by G A Andreev *et al.*, in *Sov Phys-Solid State (USA)*, **9** (1968) 2564.
5 Montojo M T & Sanchez C, *J Phys & Chem Solids (GB)*, **35** (1974) 1437.
6 Uchida Y & Nakai Y, *J Phys Soc Jpn (Japan)*, **8** (1953) 795.
7 Hadley W B, *Proc Int Symp on Colour Centres in Alkali Halides*, Rome, 1968, 114.
8 Paramo N & Sanchez C, *J Phys Soc Jpn (Japan)*, **30** (1971) 1106.

Indian Journal of Pure & Applied Physics
Vol. 21, January 1983, pp 11-15

Appearance Energies of Fragment Ions from Cyclohexanone

EZZAT T M SELIM* & M A RABBIH
Nuclear Physics Department, Atomic Energy Establishment, Cairo, Egypt

Received 12 *February* 1982

Electron impact mass spectrometry is used to study appearance energies for ions with $m/z = 98$ (parent ion), 70, 69, 55 and 42 obtained from cyclohexanone at and near threshold. Appearance energies for fragment ions at threshold are measured, for the first time, at 11.75, 11.17, 12.64 and 12.00 eV for ions with $m/z = 70$, 69, 55 and 42 respectively. Metastable peaks have been detected at $m/z = 50.0$, 48.6, 43.2 and 25.2. Mechanisms for the formation of the fragment ions at threshold are proposed. Heats of formation for the ions are calculated and compared with the values reported previously for the same ions but from different precursors. Probable processes which may be responsible for some of the higher appearance energies for the fragment ions are suggested.

1 Introduction

The mass spectrum and fragmentation of cyclohexanone were studied by many workers[1-3]. Also, the ionization energy of cyclohexanone is measured at threshold only by Higasi *et al.*[4] and by Watanabe *et al.*[5] However, appearance energy (AE) of fragment ions produced from cyclohexanone ($C_4H_6O^+$, $C_4H_5O^+$,...) and accordingly heats of formation (ΔH_f) for these ions are not available in the literature.

The purpose of the present work is to study ionization energy of $C_6H_{10}O^+$ parent ion and AEs of fragment ions having $m/z = 70$, 69, 55 and 42 obtained from cyclohexanone at and near threshold. ΔH_f values for the fragment ions are calculated and compared with similar ions obtained from different precursors. Also, metastable peaks are detected at 50 eV only, in order to define the probable paths for formation of the fragment ions.

Electron impact energy distribution difference (EDD) technique has been used for determining ionization energy and AEs as well as the structure in ionization efficiency (IE) curves. This technique[6-10] is proved to be useful for the present type of study.

2 Experimental Technique

The IE curves are obtained using Atlas CH-4 mass spectrometer by measuring the ion intensity with electron energy varied in steps of 0.10 eV. These measured IE curves are treated by the EDD technique using the value[10] of b equal to 0.60 (b is a constant characteristic for the EDD technique). Metastable peaks are measured at 50 eV only. The details of the experimental technique, calibration of energy scale and problems encountered in the study have been reported previously[8].

3 Results and Discussion

The mass spectrum of cyclohexanone is studied at 50 and 12 eV. The parent ion abundance increases from 35.83% to base peak with decreasing electron energy from 50 to 12 eV. The most intense peak at 50 eV is for the fragment ion with $m/z = 55$ while that for the parent ion is at 12 eV.

The IE curves for the five ions measured for 3 eV above threshold are shown in Figs 1 and 2. The initial portion of each curve is drawn on a greater scale on the original one. The results obtained together with those reported previously, where available (for comparison purpose), are given in Table 1, which also reports the heat of formation for the ions at threshold only. The limits of error, quoted in Table 1, are the standard deviations for five measurements.

3.1 Parent Ion $C_6H_{10}O^+$ ($m/z = 98$)

The IE curve for the parent ion exhibits a tail at threshold. The ionization energy at threshold is

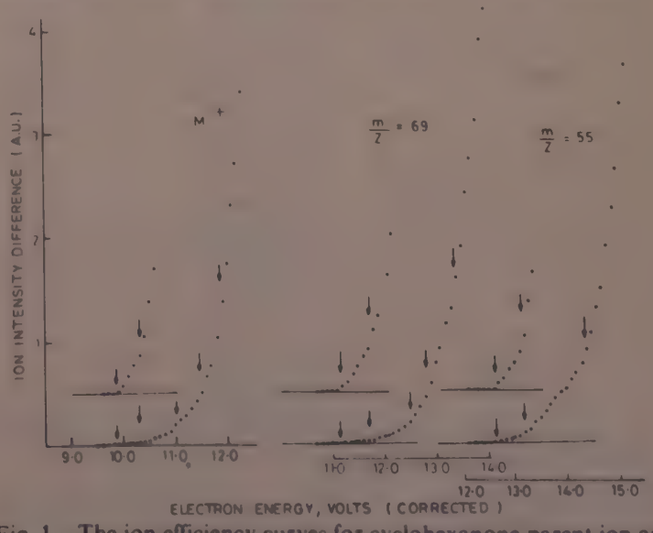

Fig. 1—The ion efficiency curves for cyclohexanone parent ion and fragment ions with $m/z = 69$ and $m/z = 55$

measured at 9.85 eV. This value is in very good agreement with previously reported electron impact values[4], but is higher by about 0.70 eV than the photoionization value reported by Watanabe and his coworkers[5]. The large difference between photoionization and electron impact ionization energy values is due to either: (a) photoionization value is due to adiabatic transition but electron impact values are due to vertical transitions (transition probability to the lowest vibrational state is small) or (b) electron impact values are corresponding to an electronic excited state of the ion but photoionization value is corresponding to the electronic ground state of the ion.

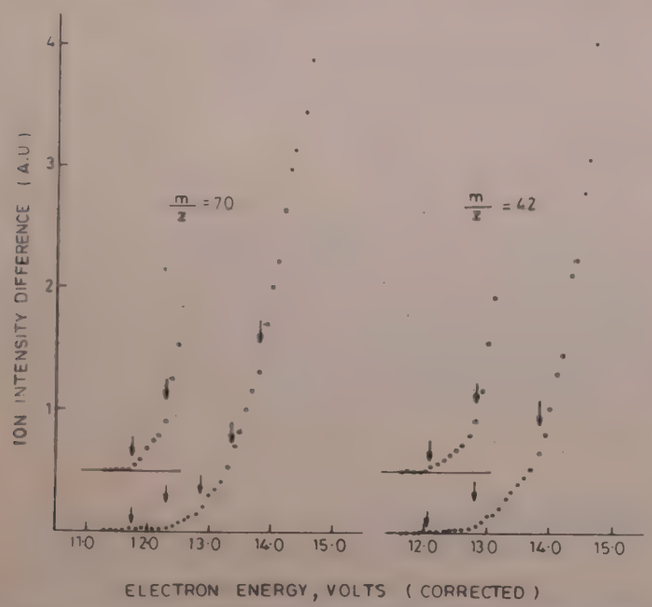

Fig. 2— The ion efficiency curves for fragment ions with $m/z = 70$ and $m/z = 42$

The first ionization energy of cyclohexanone very probably corresponds to a removal of a fairly localized electron, namely, one of the nonbonding *p* electrons of the oxygen atom. No information concerning the excited and superexcited states of cyclohexanone is available; so, one cannot report conclusions concerning higher ionization energies (due to C—O and C—C electrons) and autoionization levels in the parent ion. However, two levels are measured at 11.10 and 11.80 eV and correspond well to AEs of $C_4H_5O^+$ (11.17 eV) and $C_4H_6O^+$ (11.75 eV) fragment ions respectively. So, it is possible that these two levels at 11.10 and 11.80 eV are predissociated and may be responsible for the appearance of the two fragment ions.

Table 1—Appearance Energies and Heats of Formation for Ions with $m/z = 98$, 70, 69, 55 and 42

	Ionization & appearance energy (eV)		Heat of formation* (kJ mol^{-1})	
m/z	Present work	Previous work	Present work	Literature
98	9.85 ± 0.04	9.14[5], 9.91[4], 9.83[4]	723.4	703[11], 657[11,‡]
	10.30 ± 0.06			
	11.10 ± 0.07			
	11.45 ± 0.09			
	11.80 ± 0.09			
70	11.75 ± 0.08		855†	812[11†]
	12.30 ± 0.07			
	12.85 ± 0.09			
	13.35 ± 0.09			
	13.80 ± 0.10			
69	11.17 ± 0.06		747†, 869‡	812[11,‡], 824[12,‡]
	11.70 ± 0.08			
	12.50 ± 0.08			
	12.80 ± 0.07			
	13.35 ± 0.09			
55	12.64 ± 0.08		802†, 965‡	795[13,†], 925[11,‡]
	13.15 ± 0.08			
	14.35 ± 0.09			
42	12.00 ± 0.10		990‡, 827†	958[11,‡], 791[14,†]
				841[15,†], 858[16]
	12.80 ± 0.08			
	13.80 ± 0.11			

*ΔH_f values for molecules and neutral radicals used in the calculation of ΔH_f values for ions are taken from Ref. 17. ΔH_f for $C_6H_{10}O$ molecule is taken from Ref. 18.

†Oxygenated ions

‡Non-oxygenated ions

3.2 $C_4H_6O^+$ ($m/z = 70$) Fragment Ion

The AE at threshold for $C_4H_6O^+$ fragment is measured at 11.75 eV. No similar values are available in the literature to compare with. The fragment ion is formed directly by opening the ring and loss of CO or C_2H_4 molecule. It has been found[18], however, that in many cases, a cyclic ketone dissociates to form (P-28) ion by elimination of C_2H_4 in the same way as from cycloparaffins. A metastable peak at $m/z = 50.0$ is observed in the present mass spectrum, indicating the formation of $C_4H_6O^+$ or $C_5H_{10}O^+$ fragment from the parent[18] ion. The mechanism of formation of $C_4H_6O^+$ is shown in Reaction 1.

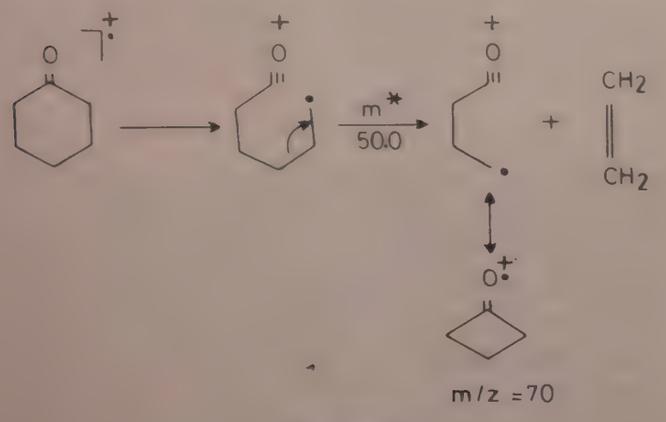

Reaction 1

The $C_4H_6O^+$ ion may be formed as a trivalent oxonium or cyclobutanone ion. The calculated ΔH_f value is 855 kJ mol^{-1}. Franklin *et al.*[11] reported the value 812 kJ mol^{-1} for ΔH_f for linear $C_4H_6O^+$. If one assumes that the formed ion is $C_5H_{10}^+$, the calculated ΔH_f for this ion will be too high to account for the formation of even cyclic $C_5H_{10}^+$ with ΔH_f equal to 941 kJ mol^{-1}, as reported by Franklin *et al.*[11]

Four higher AEs are obtained from $C_4H_6O^+$ IE curve at 12.30, 12.85, 13.35 and 13.80 eV. The AE at 12.85 eV has similars in the IE curves with $m/z = 69$ and $m/z = 42$ which suggest that the origin of all higher AEs around 12.85 eV is the same and is probably due to preionization. The higher AE at 13.80 eV is explained tentatively as due to the following process with $\Delta H_{reaction} = 13.56$ eV:

$$C_6H_{10}O^+ \rightarrow C_4H_6O^+ + C_2H_2 + H_2$$

3.3 $C_4H_5O^+$ or $C_5H_9^+$ ($m/z = 69$) Fragment Ion

The AE of the fragment ion with $m/z = 69$ is measured at 11.17 eV. The ion is either formed from parent ion with rearrangement process and loss of C_2H_5 radical to form $C_4H_5O^+$ fragment or from parent ion also but with loss of CHO radical to form $C_5H_9^+$ fragment. The following two mechanisms (see Reaction 2) illustrate this.

Beynon *et al.*[18] favour the fragmentation of the parent ion by loss of C_2H_5 radical to form $C_4H_5O^+$. A

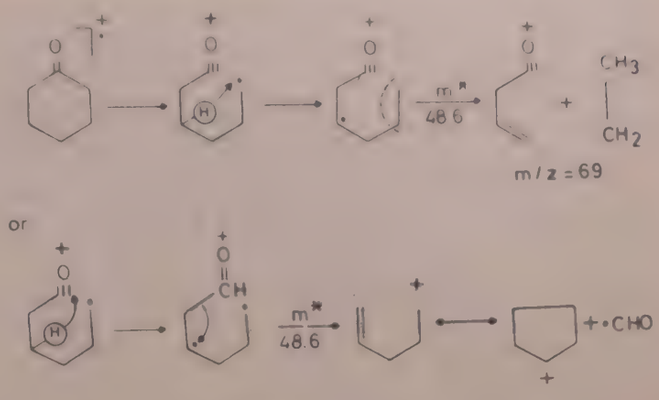

Reaction 2

metastable peak at $m/z = 48.6$ is obtained in our mass spectrum confirming the formation of ion with $m/z = 69$ from the parent ion. It is worth noting that the process of formation of $m/z = 69$ fragment ion by rearrangement requires less activation energy than the process forming $C_4H_6O^+$ ion. This is reflected in the relative intensity of $m/z = 69$ fragment ion which is greater than that of $C_6H_6O^+$ fragment either at 50 or 12 eV indicating greater stability of $m/z = 69$ fragment ion.

Assuming the formed ion is $C_4H_5O^+$, the calculated ΔH_f will be equal to 747 kJ mol^{-1} while ΔH_f value corresponding to $C_5H_9^+$ fragment is equal to 839 kJ mol^{-1}. Franklin *et al.*[11] reported the value 812 kJ mol^{-1} for cyclo $C_5H_9^+$ fragment while Lossing and Treager[12] calculated the value to be 824 kJ mol^{-1} from the ionization energy of cyclo $C_5H_9^+$ radical.

Four higher AEs are measured for $m/z = 69$ fragment ion at 11.70, 12.50, 12.80 and 13.35 eV. Assuming the ion formed is $C_5H_9^+$, the second AE at 12.50 eV can be tentatively attributed to the following process with $\Delta H_{reaction} = 12.46$ eV:

$$C_6H_{10}O^+ \rightarrow C_5H_9^+ + CO + H$$

3.4 $C_3H_3O^+$ or $C_4H_7^+$ ($m/z = 55$) Fragment Ion

The fragment ion with $m/z = 55$ is the most abundant peak in the spectrum at 50 eV. As reported by Beynon *et al.*[18] the ion can be formed from the fragment $C_4H_6O^+$ by loss of CH_3 radical as shown by Reaction 3:

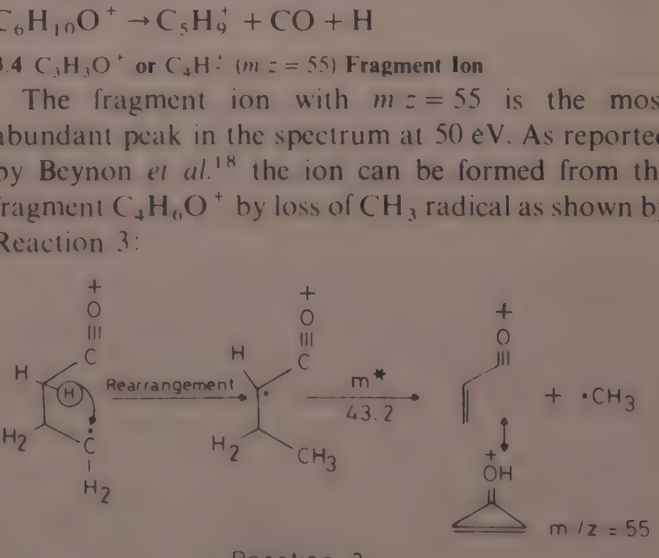

Reaction 3

The detection of a metastable peak at $m/z = 43.2$ in the present mass spectrum confirms the previous mechanism, indicating the formation of $C_3H_3O^+$

The detection of a metastable peak at $m/z = 43.2$ in the present mass spectrum confirms the previous mechanism, indicating the formation of $C_3H_3O^+$ fragment from $C_4H_6O^+$ and not directly from parent ion by loss of C_3H_7 radical as shown by Reaction 4.

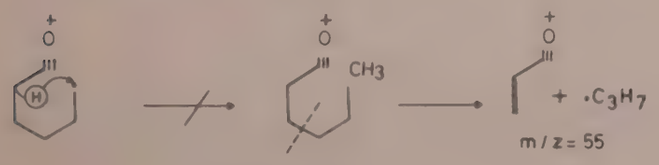

Reaction 4

However, Benz and Henneberg[19] reported that the fragment ion at $m/z = 83$ may be formed at 70 eV from the parent ion by loss of CH_3 radical. A metastable peak is observed by us at $m/z = 70.3$ confirming the formation of this ion from the parent ion. In our opinion, the fragment ion with $m/z = 55$ may be formed also as non-oxygenated ion $C_4H_7^+$ from $m/z = 83$ ion by loss of CO as shown by Reaction 5.

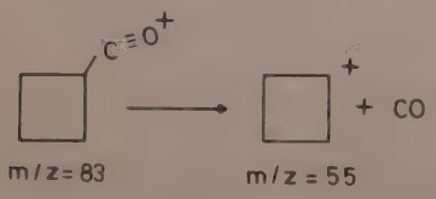

Reaction 5

The AE for $C_3H_3O^+$ fragment ion is measured at 12.64 eV and the calculated heat of formation is equal to 802 kJ mol^{-1}. This value is in excellent agreement with the ΔH_f value 795 kJ mol^{-1} for linear $CH_2 = CHCO^+$ ion obtained much earlier by Majer *et al.*[13]

The third AE at 14.35 eV is tentatively explained as due to the following process with $\Delta H_{reaction}$ equal to 14.37 eV:

$$C_6H_{10}O^+ \rightarrow C_3H_3O^+ + C_2H_2 + H_2 + CH_3$$

If one assumes that the formed ion is cyclo-$C_4H_7O^+$, the calculated ΔH_f value will be equal to 965 kJ mol^{-1} which is in reasonable agreement with the ΔH_f value for cyclo-$C_3H_4CH_3^+$ reported by Franklin *et al.*[11]

3.5 $C_3H_6^+$ or $C_2H_2O^+$ ($m/z = 42$) Fragment Ion

The fragment ion with $m/z = 42$ has either $C_3H_6^+$ or $C_2H_2O^+$ structure. A metastable peak at mass 25.2 has been detected which indicates that the ion is formed from $C_4H_6O^+$ ion ($m/z = 70$) by loss of CO or C_2H_4 as depicted in Reaction 6.

However, Hofman[20] studied the mass spectrum of cyclobutanone and concluded from accurate mass determination that the fragment ion with $m/z = 42$ is due to ketene structure ($C_2H_2O^+$).

The AE of $m/z = 42$ fragment ion is measured at 12.00 eV. Assuming that the ion at threshold has $C_3H_6^+$

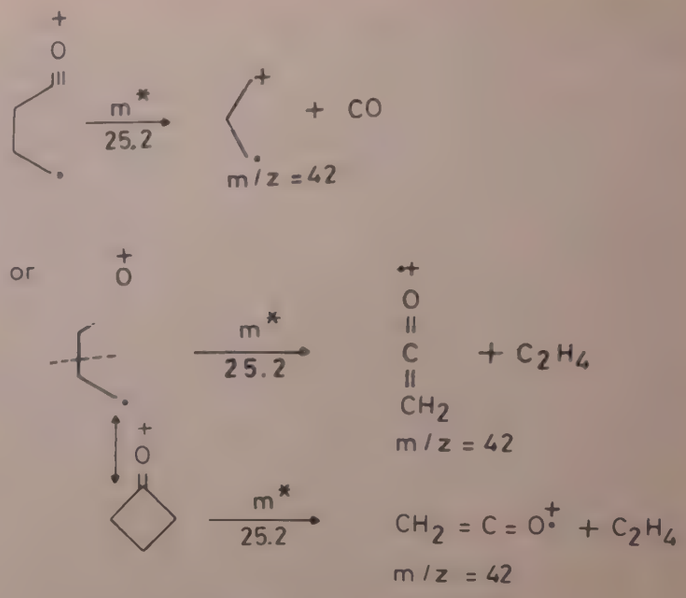

Reaction 6

structure, the calculated ΔH_f value for the ion is equal to 990 kJ mol^{-1}. Since the process of formation of $C_3H_6^+$ from $C_4H_6O^+$ is a simple bond cleavage process, the process does not need reverse activation energy but one cannot rule out the necessity of small kinetic shift energy. The value 990 kJ mol^{-1} may be compared with the value 958 kJ mol^{-1} for ΔH_f for linear $C_3H_6^+$ reported by Franklin *et al.*[11] On the other hand, if the ion formed at threshold is the ketene ion ($C_2H_2O^+$), the calculated ΔH_f value is equal to 827 kJ mol^{-1}. This value is compared with Δ_f values for $C_2H_2O^+$ reported in the literature as 790.8 (Ref. 14), 841 (Ref. 15) and 858 (Ref. 16) kJ mol^{-1}.

Whether the formed ion is $C_3H_6^+$ or $C_2H_2O^+$, the higher AE measured at 13.80 eV may be tentatively explained as due to the two following processes with $\Delta H_{reaction}$ equal to 13.48 and 13.43 eV respectively:

$$C_6H_{10}O^+ \rightarrow C_3H_6^+ + CO + C_2H_2 + H_2$$

or

$$C_6H_{10}O^+ \rightarrow C_2H_2O^+ + C_2H_4 + C_2H_2 + H_2$$

References

1 Barber M & Elliot R M, *12th Annual Conference on Mass Spectrometry*, (ASTM Committee E-14, Montreal), 1964.
2 Williams D H, Budzikiewicz H, Pelah Z & Djerassi C, *Monatsh Chem (Austria)*, **95** (1964) 166.
3 Seibel J & Gaumann T, *Z Anal Chem (Germany)*, **197** (1963) 33.
4 Higasi K, Nozoe T & Omura I, *Bull Chem Soc Jpn (Japan)*, **30** (1957) 408.
5 Watanabe K, Nakayama T & Mottl J, *J Quant Spectrosc Radiat Transfer (GB)*, **2** (1962) 369.
6 Collin J H, Winters R E & Engerholm G G, *J Chem Phys (USA)*, **49** (1968) 2469.
7 Collegos R J & Klaver R F, *J Sci Instrum (GB)*, **44** (1967) 427.
8 Selim E T M, *Indian J Pure & Appl Phys*, **14** (1976) 547.
9 Selim E T M, *Indian J Pure & Appl Phys*, **18** (1980) 31.
10 Rabbih M A, Selim E T M & Fahmey M A, *Indian J Pure & Appl Phys*, **19** (1981) 962.

11 Franklin J L, Dillard J C, Rosenstock H M *et al., Ionization potentials, appearance potentials and heats of formation of gaseous positive ions*, NSRDS-NBS. Document No. 26 (US Government Printing Office, Washington D.C.), 1969.
12 Lossing F P & Traeger J C, *Int J Mass Spectrom & Ion Phys (Netherlands)*, **19** (1976) 9.
13 Majer J R, Patrick G R & Robb J C, *Trans Faraday Soc (GB)*, **57** (1961) 14.
14 Gallegos E J & Kiser R W, *J Am Chem Soc (USA)*, **83** (1961) 773.
15 Dorman F H, *J Chem Phys (USA)*, **42** (1965) 65.
16 Murad E & Inghram M G, *J Chem Phys (USA)*, **41** (1964) 404.
17 Wagman D D, Evans W H, Parker V B, *et al., NBS Tech Note* 270-3 (US Government Printing Office. Washington, D.C. 20402) 1968.
18 Beynon J H, Saunders R A & Williams A E, *The mass spectra of organic molecules* (Elsevier, Amsterdam), 1968.
19 Benz W & Henneberg D, *Massenspectrometric Organischer Verbindungen* (Deutsche Demokratische Republik, Leipzig), 1969.
20 Hofman H J, *Tetrahedron Lett (GB)*, (1964) 2329.

Indian Journal of Pure & Applied Physics
Vol. 21, January 1983, pp 16-18

Vibrational Analysis of Some Linear Symmetrical Metal Dihalide Ions

B MOHAN SRINIVASAN
Department of Physics, Coimbatore Institute of Technology, Coimbatore 641 014
and
R RAMASAMY*
Department of Physics, PSG Autonomous College of Arts & Science, Coimbatore 641 014

Received 1 *May* 1982

The force constants of metal dihalide ions ($CuCl_2^-$, $CuBr_2^-$, CuI_2^-, $AgCl_2^-$, AgI_2^-, $AuCl_2^-$ and $AuBr_2^-$) have been evaluated by the *F-G* matrix method, using the revised vibrational frequencies. These force constants have been used to calculate the mean amplitudes of vibration, the Bastiansen-Morino shrinkage effect and the centrifugal stretching coefficients of these ions, for the first time. The results have been discussed.

1 Introduction

The metal dihalide ions belong to the linear symmetrical triatomic system with ($D_{\infty h}$) symmetry. These ions, according to the relevant selection rules[1], give rise to four vibrational degrees of freedom, forming three fundamental frequencies. They are distributed under three separate species as $\Sigma_g^+ + \Pi_u + \Sigma_u^+$ where the gerade mode is Raman active only and symmetric with respect to the centre of symmetry whereas the ungerade modes are infrared active only and asymmetric with respect to the centre of symmetry. The vibrations under the symmetry species Σ_g^+ and Σ_u^+ are nondegenerate and parallel while the remaining vibration under the species Π_u is doubly degenerate and perpendicular. The mean amplitudes of vibration and shrinkage effect have been evaluated by Nagarajan[2] for some metal halide molecules. In the present investigation, the force constants, the mean amplitudes of vibration of bonded and nonbonded atom pairs, the shrinkage constants and the centrifugal stretching coefficients of some metal halides in the ionic state have been evaluated for the first time using the revised frequencies[3,4].

2 Results and Discussion

2.1 Molecular Parameters and Force Constants

The observed frequencies and the bond-lengths of metal halide ions under investigation are presented in Table 1. The frequencies of the first five ions and the last two are taken from Refs 3 and 4 respectively. The bond lengths are taken from Ref. 5. The valence force constants of the ions calculated by the *F-G* matrix method are listed in Table 2. The stretching (f_r), bending (f_α) and interaction (f_{rr}) force constants are observed to decrease towards the higher member of the halogen group in all the three metal halide ions under investigation.

2.2 Mean Amplitudes of Vibration

Cyvin[6] was the first to introduce symmetry coordinates in the evaluation of mean-square amplitudes of vibration from molecular vibrational analysis. According to his method[7-9], for linear symmetrical triatomic molecules the secular equations giving the normal frequencies in terms of the mean square amplitude quantities(σ) may be constructed with the help of Σ and G matrices as follows:

Σ_g^+ species : $\Delta_1 = \Sigma_{11}\mu_i^{-1}$

Π_u species : $\Delta_2 = \Sigma_{22}(4\mu_j + 2\mu_i)^{-1}$

Σ_u^+ species : $\Delta_3 = \Sigma_{33}(2\mu_j + \mu_i)^{-1}$

where μ_i and μ_j are the reciprocal masses of the atoms i

Table 1 — Vibrational Frequencies & Equilibrium Bond Lengths of some Linear Symmetrical Metal Dihalide Ions

Ion	Bond length (A)	Frequencies, cm^{-1}		
		ν_1	ν_2	ν_3
$CuCl_2^-$	2.25	300	109	405
$CuBr_2$	2.25	193	81	322
CuI_2	2.40	148	65	279
$AgCl_2$	2.36	268	88	333
AgI_2	2.78	133	49	215
$AuCl_2$	2.31	329	112	350
$AuBr_2$	2.51	209	79	254

Table 2 — Valence Force Constants (in mdyne A) of some Linear Symmetrical Metal Dihalide Ions

Ion	f_r	f_{rr}	f_α
$CuCl_2$	2.3542	1.0149	0.0590
$CuBr_2$	1.4465	−0.0520	0.0471
CuI_2	1.1379	−0.3180	0.0320
$AgCl_2$	2.7796	1.7849	0.0975
AgI_2	1.1061	0.0180	0.0535
$AuCl_2$	6.8672	5.6935	0.2212
$AuBr_2$	3.1658	1.9031	0.1622

and j respectively, and the analytical expressions for the symmetrized mean-square amplitude matrices (Σ) in terms of the mean-square amplitude quantities (σ) are given as follows:

$$\Sigma_{11} = \sigma_r + \sigma_{rr} \quad \Sigma_{22} = \sigma_\theta \text{ and } \Sigma_{33} = \sigma_r - \sigma_{rr}$$

Here σ_r is the mean-square amplitude quantity due to the bonded atom pair i-j, σ_{rr} the quantity due to the interaction between the bonds and σ_θ the quantity due to the bending of the molecule. In the above equations, Δ is related to the vibrational frequency, as

$$\Delta_i = \left(\frac{h}{8\pi^2 \nu_i}\right) \coth \frac{h\nu_i}{2kT}$$

where k is the Boltzmann constant and T the temperature in degrees Kelvin. Since the secular equations are singular on account of the greater symmetry of the molecular system, symmetrized mean-square amplitude matrices Σ_{11}, Σ_{22} and Σ_{33} are easily evaluated. These matrices yield the mean-square amplitude quantities σ_r, σ_{rr} and σ_θ. The calculated numerical values of these quantities in $(\text{Å})^2$ are presented in Table 3, for the ions under investigation at the temperature of 300 K. For a molecule of the type under investigation, the expressions for the generalized mean-square amplitude quantities in terms of the symmetrized mean-square amplitude matrices, according to Cyvin[10] are:

$$\langle \Delta z^2 \rangle = \frac{\Sigma_{11} + \Sigma_{33}}{2} \text{ and } \langle \Delta x^2 \rangle = \langle \Delta y^2 \rangle = \frac{\Sigma_{22}}{4}$$

for the bonded atom pair i-j and $\langle \Delta z^2 \rangle = 2\Sigma_{11}$ for the non-bonded atom pair i-i. By symmetry of the molecular system, the mean-square perpendicular amplitudes of vibration for the nonbonded atom pair and mean cross-products for the bonded as well as nonbonded atom pairs vanish. Table 4 contains the calculated numerical values of the generalized mean-square amplitude quantities in $(\text{Å})^2$ for the bonded and non-bonded atom pairs of the metal dihalide ions studied. The corresponding values of the mean amplitudes of vibration for both the bonded and non-bonded atom pairs are presented in Table 5. Referring to Table 3, it can be observed that the mean-square amplitude of vibration due to the bending of the molecule is, in general, very much greater than that due to the bonded atom pair and the quantity due to the interaction of two atom pairs is small. With regard to the mean amplitudes of vibration of bonded and non-bonded atom pairs given in Table 5, it can be seen that the mean amplitudes of vibration for bonded as well as non-bonded atom pairs are in the increasing order towards the higher members of the halogen group for all the three groups of metal halide ions. This shows that the replacement of end atoms with atoms of higher atomic weight to the molecular system causes an increase in the mean amplitudes of vibration for the bonded and non-bonded distances. It can be noted that the reverse is the case for the corresponding force constants (Table 2). Though electron diffraction studies have been made for some dihalides[11-15], experimental values of the mean amplitudes of vibration of the ions under investigation are not

Table 3—Mean Square Amplitude Quantities (in Å^2) of some Linear Symmetrical Metal Dihalide Ions at 300 K

Ion	σ_r	σ_{rr}	σ_θ
$CuCl_2^-$	0.004831	−0.000447	0.135100
$CuBr_2^-$	0.007170	−0.005020	0.179814
CuI_2^-	0.005947	−0.001084	0.249513
$AgCl_2^-$	0.005703	−0.000257	0.161996
AgI_2^-	0.006916	−0.000908	0.294468
$AuCl_2^-$	0.004066	−0.000387	0.117639
$AuBr_2^-$	0.004385	−0.000469	0.097389

Table 4—Generalized Mean Square Amplitude Quantities (in Å^2) of some Linear Symmetrical Metal Dihalide Ions

Ion	Mean square amplitude quantity	Bonded atom pair (i—i)	Non-bonded atom pair (i—i)
$CuCl_2^-$	$\langle \Delta x^2 \rangle = \langle \Delta y^2 \rangle$	0.033781	0
	$\langle \Delta z^2 \rangle$	0.004831	0.008768
$CuBr_2^-$	$\langle \Delta x^2 \rangle = \langle \Delta y^2 \rangle$	0.044953	0
	$\langle \Delta z^2 \rangle$	0.007170	0.004299
CuI_2^-	$\langle \Delta x^2 \rangle = \langle \Delta y^2 \rangle$	0.062376	0
	$\langle \Delta z^2 \rangle$	0.005947	0.009695
$AgCl_2^-$	$\langle \Delta x^2 \rangle = \langle \Delta y^2 \rangle$	0.040492	0
	$\langle \Delta z^2 \rangle$	0.005703	0.010892
AgI_2^-	$\langle \Delta x^2 \rangle = \langle \Delta y^2 \rangle$	0.073617	0
	$\langle \Delta z^2 \rangle$	0.006916	0.012016
$AuCl_2^-$	$\langle \Delta x^2 \rangle = \langle \Delta y^2 \rangle$	0.017937	0
	$\langle \Delta z^2 \rangle$	0.004066	0.007359
$AuBr_2^-$	$\langle \Delta x^2 \rangle = \langle \Delta y^2 \rangle$	0.024345	0
	$\langle \Delta z^2 \rangle$	0.004385	0.007832

Table 5—Mean Amplitudes of Vibration (in Å) of Bonded and Non-bonded Atom Pairs in some Linear Symmetrical Metal Dihalide Ions at 300 K

Ion	Distance	Mean amplitude of vibration
$CuCl_2^-$	Cu—Cl	0.06951
	Cl...Cl	0.09360
$ClBr_2^-$	Cl—Br	0.08470
	Br...Br	0.06557
CuI_2^-	Cu—I	0.07712
	I...I	0.09848
$AgCl_2^-$	Ag—Cl	0.07552
	Cl...Cl	0.10436
AgI_2^-	Ag—I	0.08316
	I...I	0.10960
$AuCl_2^-$	Au—Cl	0.06375
	Cl...Cl	0.08578
$AuBr_2^-$	Au—Br	0.06622
	Br...Br	0.08849

Table 6—Bastiansen-Morino Shrinkage Effect (in A) in some Linear Symmetrical Metal Dihalide Ions

Ion	Shrinkage effect $\delta = 2\langle \Delta x_i^2 \rangle / r_{ij}^e$
$CuCl_2^-$	0.03002
$CuBr_2^-$	0.03995
CuI_2^-	0.05198
$AgCl_2^-$	0.03432
AgI_2^-	0.05256
$AuCl_2^-$	0.01552
$AuBr_2^-$	0.01939

Table 7—Centrifugal Stretching Coefficients (in kHz) in some Linear Symmetrical Metal Dihalide Ions

Ion	D_J	D_K	D_{JK}
$CuCl_2^-$	0.2476	0.2476	−0.4953
$CuBr_2^-$	0.0232	0.0232	−0.0464
CuI_2^-	0.0042	0.0042	−0.0084
$AgCl_2^-$	0.3956	0.3956	−0.7912
AgI_2^-	0.0037	0.0037	−0.0073
$AuCl_2^-$	0.5450	0.5450	−1.0900
$AuBr_2^-$	0.0318	0.0318	−0.0636

available to make a comparison with the results obtained in the present investigation. However, the values reported in the present investigation would be useful for the interpretation of the electron diffraction studies when undertaken.

2.3 Bastiansen-Moriono Shrinkage Effect

Using the values of the interbond distances presented in Table 1 and the mean-square perpendicular amplitudes of vibration given in Table 4, the Bastiansen-Morino shrinkage effects[16-19] have been calculated at 300 K and are given in Table 6. The shrinkage effects, as in the case of mean amplitudes of vibration are in the increasing order towards the higher members of the halogen group of all the dihalide ions studied. Though these values are small, they are real. These values are to be added to those of the observed non-bonded distances from electron diffraction experiments in order to obtain the correct values at the equilibrium position. To the knowledge of the authors, experimental values for the shrinkage effect of these dihalides from electron diffraction studies are not available to compare with the values obtained in the present investigation.

2.4 Centrifugal Stretching Coefficients

The centrifugal stretching coefficients of the metal dihalide ions under study have been evaluated by the method suggested by Kivelson and Wilson[20] and Cyvin *et al.*[21]. The numerical values calculated are given in Table 7. As the ions are linear in structure, the coefficients D_J, D_K and D_{JK} alone exist and R_5, R_6 and δ_J vanish. Since the centrifugal distortion effect is due to the rotation-vibration interaction of the molecule, the moment of inertia of the molecule is the most important factor which decides the values of the centrigugal stretching coefficients. Also, according to the theory[21], the centrigugal stretching coefficients are inversely proportional to the fourth power of the moment of inertia of the molecule or ion. Thus, the centrifugal stretching coefficients are extremely sensitive to the variations in moment of inertia. This is observed in the values of the centrigugal stretching coefficients given in Table 7. The values rapidly decrease towards the higher member of the halogen group for all the three metal halide ions. It has not been possible to compare these results with the experimental results, since, to the knowledge of the authors, such values are not available in the literature. But, these values will be useful for the microwave investigations on these ions.

References

1 Herzberg G, *Infrared and Raman Spectra of polyatomic molecules* (Van Nostrand, New York) 1945, 119.

2 Nagarajan G, *J Mol Spectrosc (USA)*, **13** (1964) 361.

3 Walters D N & Basak B, *J Chem Soc A (GB)*, (1971) 2733.

4 Braunstein P & Clark R J H, *J Chem Soc Dalton (GB)*, (1973) 1845.

5 *Table of interatomic distances and configuration in molecules and ions*, Special publication No. 11 (Chemical Society, London) 1958.

6 Cyvin S J, *Spectrochim Acta (GB)*, **15** (1959) 825, 835.

7 Cyvin S J, *Acta Polytech Scand (Finland)*, **6** (1960) 279.

8 Cyvin S J, *Spectrochim Acta (GB)*, **15** (1959) 341.

9 Cyvin S J, *Spectrochim Acta (GB)*, **15** (1959) 958.

10 Cyvin S J, *Spectrochim Acta (GB)*, **17** (1961) 1219.

11 Braune H & Knocke S, *Z Phys Chem Wiesbaden (Germany)*, **B23** (1933) 163.

12 Gregg A H, Hampson G C, Jenkins G I, Jones P L F & Sutton L E, *Trans Faraday Soc (GB)*, **33** (1937) 852.

13 Akishin P A & Spiridonov V P, *Kristallografiya (USSR)*, **2** (1957) 475.

14 Akishin P A, Spridonov V P, Sobolev G A & Naumov V A, *Zh Fiz Khim (USSR)*, **31** (1957) 461, 648, 1871; **32** (1958) 58.

15 Akishin P A, Spiridonov V P & Sabolev G A, *Dokl Akad Nauk (USSR)*, **118** (1958) 1134.

16 Almenninger A, Bastiansen O & Munthe-Kass T, *Acta Chem Scand (Denmark)*, **10** (1956) 261.

17 Almenningen A, Bastiansen O & Traetteberg M, *Acta Chem Scand (Denmark)*, **13** (1959) 1699.

18 Bastiansen O & Traetteberg M, *Acta Crystallogr (Denmark)*, **13** (1960) 1108.

19 Morino Y, *Acta Crystallogr (Denmark)*, **13** (1960) 1107.

20 Kivelson D & Wilson E B (Jr), *J Chem Phys (U S A)*, **20** (1952) 1575, **21** (1953) 1229.

21 Cyvin S J, Cyvin B N & Hagen G, *Z Naturforsch a (Germany)*, **23** (1968) 1649.

Indian Journal of Pure & Applied Physics
Vol. 21, January 1983, pp 19-24

The Decay of ^{125}Sb

K SINGH & H S SAHOTA*
Physics Department, Punjabi University, Patiala 147002

Received 27 *April* 1982

The 2.7 yr beta decay of $^{125}Sb \rightarrow {}^{125}Te$ has been studied using Ge(Li), Si(Li) and Ge detectors and the directional correlation technique. New lines at 58, 111, 642, 693 and 729 keV have been detected and fitted in the decay scheme in the already existing levels, besides the one suggested at 729 keV. The intensities of 20, 109, 111, 116, 172, 178 and 198 keV transitions have been measured more precisely than before. The γ-γ directional correlation measurements in the 208-463, 204-176 and 321-176 keV cascades have enabled to assign a unique spin 7/2 to the 525 keV level. The multipole mixing ratios for the 204, 208 and 321 keV transitions have been found as $M1 + (14.75 \pm 3.55)\% E2$, $M1 + (4.5 \pm 2.0)\% E2$ and $E1 + (2.70 \pm 0.75)\% M2$, respectively.

1 Introduction

Although the beta decay of 2.7 yr ^{125}Sb to the excited levels of ^{125}Te has been studied extensively by several investigators employing different nuclear spectroscopic techniques[1], there are uncertainties about the presence and multipole character of some of the γ-transitions. The 82, 111, 123, 178, 199 and 489 keV transitions were reported by Mazets and Sergeenkov[2]. The transitions at 111 and 123 keV were observed by Inamura[3]. Stone *et al.*[4] and Nagpal and Gaucher[5] rejected the presence of all these transitions. Later, Gupta *et al.*[6] found evidence for a 199 keV line but ruled out the 111 keV line. Thus the presence of several weak γ-rays is still controversial. There are some uncertainties and differences[3,7,8] in the spin assignments for 525, 635 and 671 keV levels.

In view of the above inconsistencies and uncertainties, the present authors have re-examined the directional correlations of the (208-463), (204-176) and (321-176) keV gamma-gamma cascades. The present measurements were undertaken to determine more accurately the spin of the 525 keV level and the multipole mixing parameters of the 204, 208 and 321 keV transitions.

2 Experimental Details

The isotope ^{125}Sb was procured from the Bhabha Atomic Research Centre, Bombay, as $SbCl_3$ and SbOCl in HCl solution. For the energy and intensity measurements with Ge(Li), Si(Li) and intrinsic Ge detectors, a point source was formed by drying the solution on a thin perspex strip. For directional correlation measurements, the supplied material was poured into 2 mm × 4 mm cylindrical perspex holders.

3 Measurements and Results

The γ-ray singles spectra for the low energy region recorded with intrinsic Ge and Si(Li) detectors are shown in Figs 1 and 2 respectively. For the higher energy region, the singles spectra were taken at 10 and 25 cm and a typical spectrum with 64-cc Ge(Li) detector is shown in Fig. 3. For energy calibration, only the intense internal lines and a few external standard lines were used. The results of the present investigations are presented in Table 1. The present measurements discard the presence of 82, 123 and 489 keV transitions reported by Mazets and Sergeenkov[2] and the 145 and 146 keV transitions reported by Walters and Meyer[9]. The transitions at 111 and 178 keV reported by Inamura[3] and Mazets and Sergeenkov[2] respectively are observed in the low energy spectra with intrinsic Ge detector. Out of the 20, 491, 497 and 693 keV transitions reported by Waltersand Meyer[9], the 20, 497 and 693 keV were observed by us in low and high energy spectra respectively. The 729 keV lines observed in the high energy region can be placed as 729 → 0 keV transition. Also a new line of 58 keV observed with both the detectors in low energy region can be placed between 729 and 671 keV levels. This gives support to 729 keV level suggested by Barrette *et al.*[10] in Coulomb excitation. All these new transitions are shown in Fig. 4 by dashed lines.

4 Discussion

4.1 The Gamma-Gamma Directional Correlation Measurements

Since the half-lives of 321 and 463 keV levels involved in the present measurements are 0.71 ns and 12.8 ps respectively, no attenuation of the directional correlation coefficients in liquid or solid form of the source is expected. The directional correlations in ^{125}Sb decay were performed using two 5.1 cm × 5.1 cm NaI(Tl) detectors covered with the anti-Compton graded shields of Al, Cu and Pb. A slow-fast coincidence assembly ($2\tau = 30$ ns) was used.

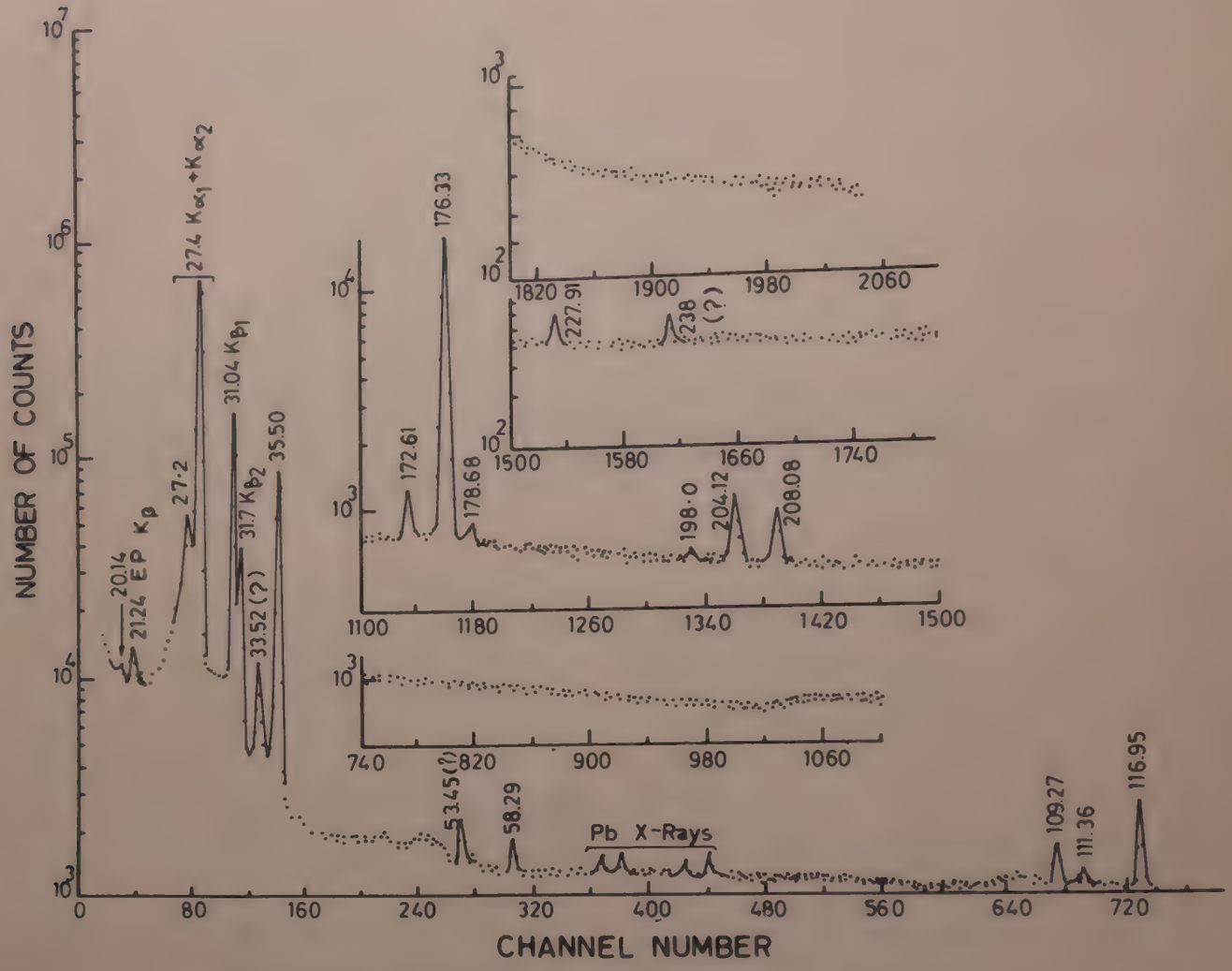

Fig. 1—Intrinsic Ge spectra of ^{125}Sb in the energy region of 5-250 keV

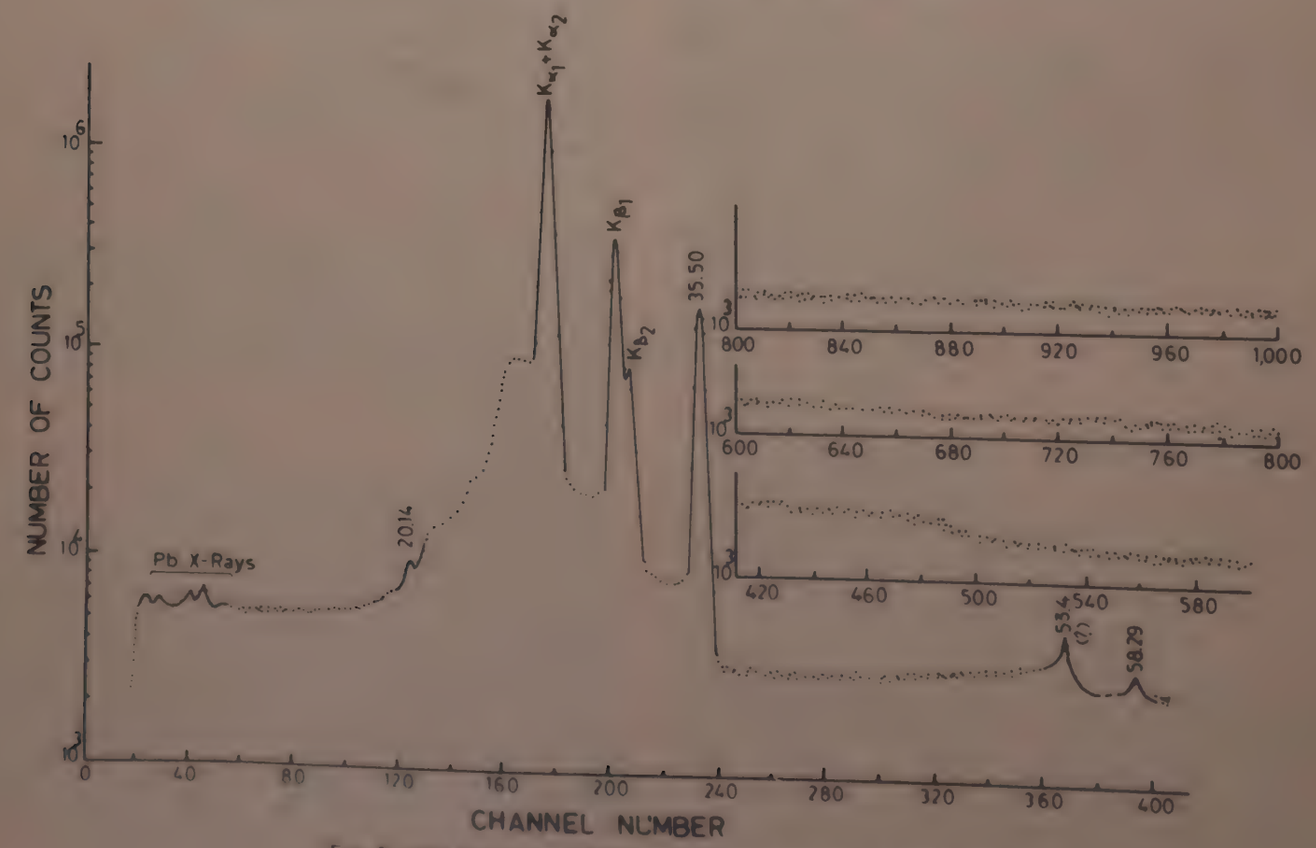

Fig. 2 Si(Li) spectra of ^{125}Sb in the energy region 5-100 keV

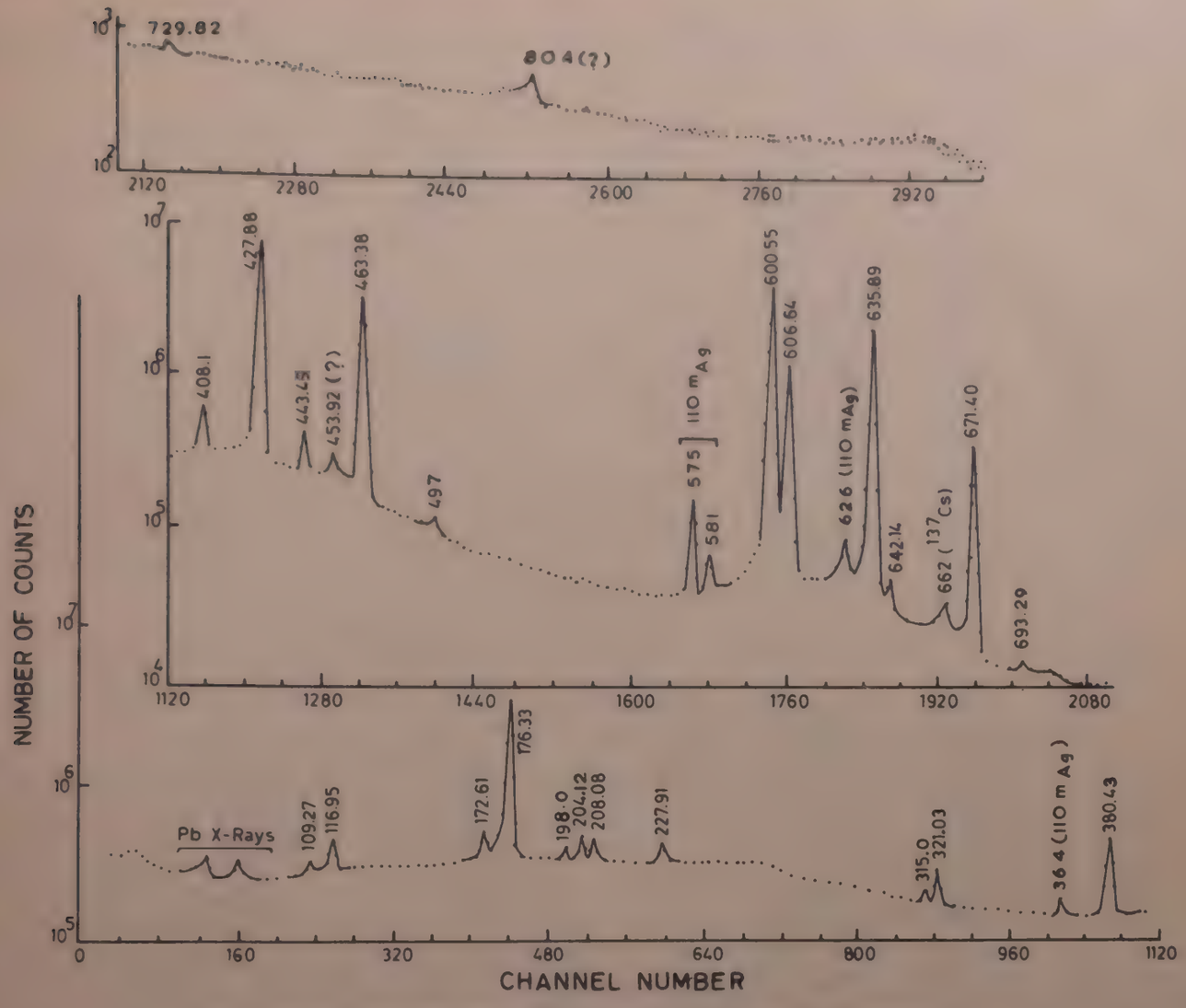

Fig. 3—Singles γ-ray spectrum of ^{125}Sb observed with 64.1-cc Ge(Li) detector

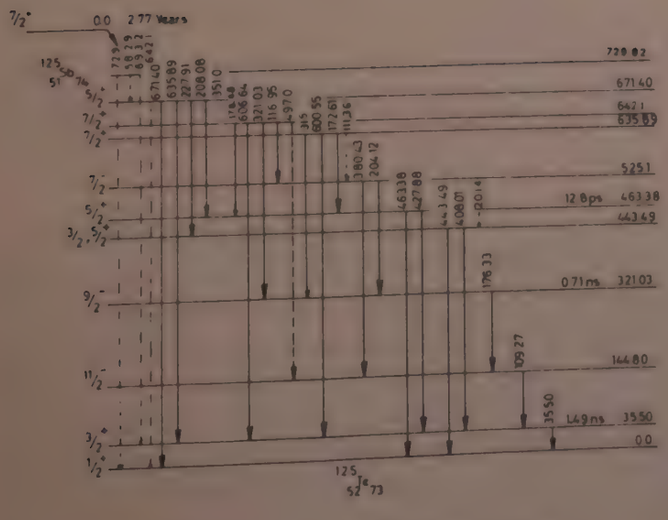

Fig. 4—Decay scheme of ^{125}Sb to ^{125}Te

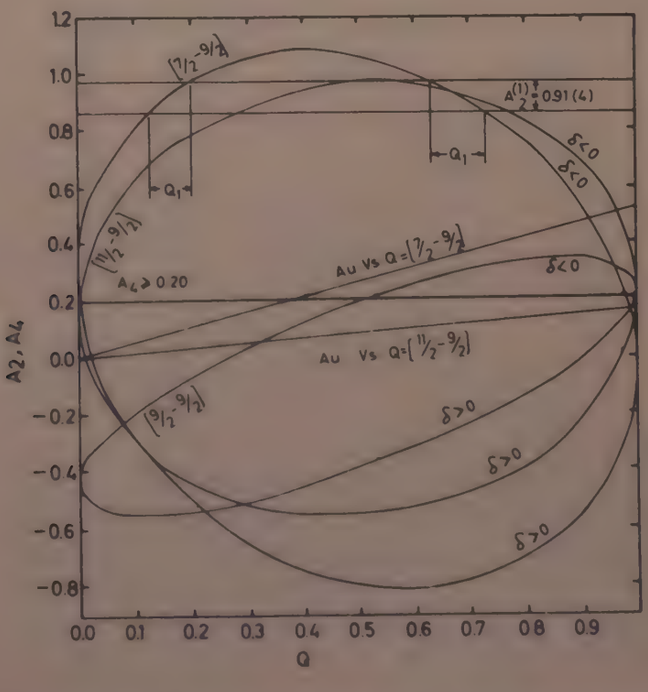

Fig. 5 A plot of A_2 and A_4 versus Q for the multipole admixture in the 204 keV transition from (204-176) keV correlation measurements and spin of the 525 keV level

Table 1—Comparison of the Observed γ-Ray Energies and Intensities in the Decay of $^{125}Sb \rightarrow {}^{125}Te$ with Literature values

Energy* (keV)	Relative intensity			
	Present study	Nagpal and Gaucher[5]	Walters and Meyer[9]	Gehrke *et al.*[16]
20.14	0.068 ± 0.002	—	0.067 ± 0.003	—
35.50	14.53 ± 0.35†	—	14.50 ± 0.44	—
58.29	0.091 ± 0.004	—	—	—
109.27	0.232 ± 0.005†	—	—	—
111.36	0.0042 ± 0.0003	—	0.0030 ± 0.0003	—
116.36	1.060 ± 0.010	1.13 ± 0.01	0.866 ± 0.014	0.910 ± 0.029
172.61	0.86 ± 0.02	0.90 ± 0.10	0.62 ± 0.01	—
176.33	24.5 ± 0.8	24.9 ± 2.0	23.06 ± 0.07	23.9 ± 0.7
178.68	0.130 ± 0.005	—	0.091 ± 0.002	—
198.0	0.081 ± 0.004	—	0.044 ± 0.001	—
204.12	1.14 ± 0.04	1.15 ± 0.10	1.097 ± 0.014	1.15 ± 0.04
208.08	0.82 ± 0.02	0.85 ± 0.08	0.802 ± 0.014	0.829 ± 0.025
227.91	0.44 ± 0.02	0.44 ± 0.04	0.448 ± 0.014	—
315.0	0.013 ± 0.002	—	0.014 ± 0.001	—
321.03	1.30 ± 0.05	1.41 ± 0.10	1.393 ± 0.014	1.422 ± 0.016
380.43	6.02 ± 0.25	5.27 ± 0.40	5.16 ± 0.03	5.10 ± 0.05
408.1	0.61 ± 0.03	0.62 ± 0.06	0.62 ± 0.02	—
427.88	100	100	100	100
443.49	1.12 ± 0.05	1.03 ± 0.10	1.03	—
463.38	35.50 ± 0.07	35.4 ± 2.8	35.50 ± 0.07	35.26 ± 0.37
497.0	0.015 ± 0.003	—	0.012 ± 0.003	—
600.55	60.50 ± 0.10	61.5 ± 4.9	60.39 ± 0.10	60.6 ± 0.6
606.64	17.2 ± 0.3	16.4 ± 1.2	17.052 ± 0.034	17.12 ± 0.17
635.89	39.1 ± 0.2	37.3 ± 0.3	38.45 ± 0.07	38.6 ± 0.4
642.14	0.160 ± 0.009	—	—	—
671.40	5.9 ± 0.3	6.0 ± 0.5	6.11 ± 0.13	6.18 ± 0.06
693.29	0.0015 ± 0.0006	—	—	—
729.82	0.0025 ± 0.0007	—	—	—

*Energy calibration was provided internally using γ-energies of prominent lines from the work of Walters and Meyer[9].
†This γ-ray is in transient equilibrium with the ^{125}Sb decay.

Table 2—Directional Correlation Coefficients for Various Cascades in ^{125}Te

Cascade energy (keV)	Inamura[3]	Verma[15]	Present study	Mixing ratio
(208-463)	$A_{22} = 0.062 \pm 0.032$ $A_{44} = -0.013 \pm 0.076$	$A_{22} = 0.107 \pm 0.048$ $A_{44} = -$	$A_{22} = 0.092 \pm 0.027$ $A_{44} = 0.018 \pm 0.044$	$\delta_{208} = 0.217 \pm 0.047$
(321-176)	$A_{22} = -0.169 \pm 0.027$ $A_{44} = 0.018 \pm 0.034$	$A_{22} = -0.188 \pm 0.018$ $A_{44} = -0.014 \pm 0.038$	$A_{22} = -0.238 \pm 0.016$ $A_{44} = 0.042 \pm 0.028$	$\delta_{321} = 0.166(23)$
(204-176)	$A_{22} = -0.364 \pm 0.048$ $A_{44} = 0.100 \pm 0.075$	$A_{22} = -0.481 \pm 0.036$ $A_{44} = 0.064 \pm 0.028$	$A_{22} = -0.36 \pm 0.02$ $A_{44} = 0.047 \pm 0.032$	$\delta_{204} = 0.416(57)$

The coincidence counts recorded at 90°, 135° and 180° were corrected for chance coincidence counts by introducing an appropriate delay in one of the fast channels. The true coincidences thus obtained were further corrected for the finite solid angle corrections by the method of Yates[11].

4.2 The (208-463) keV Cascade

This cascade can have the interfering contribution of (208-428) keV cascade. To minimize this contribution, the 208 and 463 keV energies were selected with the settings of single channel analyzer (SCA) above 205 keV and 463 keV respectively. The correlation coefficients after solid angle corrections are shown in Table 2.

The 463 keV being $(5/2^+ \text{-} 1/2^+)$ transition may be taken as pure $E2$. The analysis of (208-463) keV cascade yields: $A_2(208) = -0.173 \pm 0.051$.

From Arns-Wiedenbeck[12] plot for spin sequence (5/2-5/2), $A_2(208)$ gives two values of Q, the quadrupole

content in 208 keV transitions, namely
$0.025 \leq Q_1 \leq 0.065, \quad 0.87 \leq Q_2 \leq 0.924$

The lower value of Q is compatible with the predominantly $M1$ character for the 208 keV transition as obtained for the conversion coefficient [$\alpha_k = 0.091(9)$] of the present study. Also the present conversion coefficients [$\alpha_k = 0.0033(4)$] and [$\alpha_k = 0.0039(3)$] for 671 and 636 keV transitions assign pure $E2$ and $M1 + E2$ mixed character to the respective transitions yielding $5/2^+$ character for the 671 keV level. Therefore, the 208 keV transition is taken as $M1 + (4.5 \pm 2.0)\% E2$. This result favours a positive δ value for its mixing ratio as $\delta_{208} = 0.216 \pm 0.017$ and $5/2^+$ spin is assigned to the 671 keV level.

4.3 The (321-176) keV Cascade

Because the energies involved in this cascade are such so as to lie in the low energy region of back-scattered Compton contributions of high energy γ-rays, the Compton scattered contribution of high energy γ-rays is eliminated with the subtraction of continuous background lying under the desired peak. Thus the (321-176) keV correlation was free from (172-428) keV and (172-463) keV cascades. Multipole mixing ratio analysis of the measured correlation was made by using $Q_2 = 0.28 \pm 0.02$ of the $9/2^-$ ($M1$, $E2$) $11/2^-$ transitions from the work of Mazets and Sergeenkov[2]. A quadrupole content $0.02 \leq Q \leq 0.035$ or $0.93 \leq Q \leq 0.95$ for $\delta_{176} < 0$ is obtained. The higher Q value is not supported by the present measurement of $\alpha_k = 0.126 \pm 0.033$ which gives pure $M1$ character for 176 keV transition. Thus the 321 keV transition is $E1 + (2.75 \pm 0.75)\% M2$.

4.4 The (204-176) keV Cascade

The 176 keV gate selected in the present measurements contains also the contributions due to the 172 keV γ-ray and mostly by degraded photons (DP) of 428 and 463 keV. Therefore, in addition to the (204-176) keV genuine counts, the coincidence counts due to the following interfering cascades are also included:

(i) (172-428$_{DP}$, 172-463$_{DP}$) keV cascade

(ii) (172-428, 172-463) keV cascade

(iii) (208-428$_{DP}$, 208-463$_{DP}$) keV cascade.

To eliminate the contribution due to (i) above, only the half region of the gated spectrum was taken to calculate the correlation coefficients for the (204-176) keV cascade. To eliminate the contribution due to (ii) continuous background counts were subtracted from the counts under the desired peak. The contribution from (iii) was estimated to be 15% and a correction was applied accordingly.

The analysis of (204-176) keV cascade yields $A_2(204) = 0.91(4)$. Considering all the three spin values (viz. 7/2, 9/2 and 11/2) for the 525 keV level, the $A_2(204)$ corresponds to the following mixing ratios:
$0.112 \leq Q_{204} \leq 0.183, \ 0.650 \leq Q_{204} \leq 0.741$
for spin sequence 7/2-9/2 and
$0.283 \leq Q_{204} \leq 0.416, \ 0.541 \leq Q_{204} \leq 0.775$
for spin sequence 11/2-9/2.

The mixing ratio analysis [Fig. 5] clearly excludes the possibility of $9/2^-$-$9/2^-$ spin sequence, because the partial A_2 coefficient for the 204 keV transition does not intersect the ellipse corresponding to this spin sequence. To find the most suitable assignment between 7/2 or 11/2 spins, the nature of the 380 keV transition depopulating the 525 keV level is also considered. Auble[13] listed the results of the (116-380) keV directional correlation measurements as
$A_{22} = 0.10 \pm 0.01, \quad A_{44} = 0.01 \pm 0.01$
From the theoretical tables of Ferentz and Rosensweig[14], for a spin sequence $7/2^- \rightarrow 7/2^- \rightarrow 11/2^-$ for this cascade,
$A_2(116\,E1), \ A_2(380\,E2) = 0.0952; \ A_{44} = 0$
These values are in perfect agreement with the experimental values. The K-conversion coefficient for the 116 keV transition from present measurements [$\alpha_k = 0.076(9)$] confirms the $E1$ character for this transition. Thus the 525 keV level is confirmed as $7/2^-$.

5 Conclusions

The high-resolution, precisely calibrated, semi-conductor detectors have enabled us to measure the intensities of several low energy lines below 250 keV with better accuracy than achieved before. The 20, 58, 111, 178 and 198 keV γ-rays have been confirmed, for the first time, due to the use of different detectors most suitable for the work, (e.g. it is difficult to clearly see 20 keV as a separate line even with intrinsic Ge detector as the escape peaks of K_α and K_β X-rays of ^{125}Te fall in this region, but with Si(Li) detector there is no such problem). With the presence of 58 and 693 and 729 keV γ-rays the 729 keV level stands confirmed as the three γ-rays can be thought of as $729 \rightarrow 671$, $729 \rightarrow 35$ and $729 \rightarrow 0$ de-excitations. The 642 keV γ-ray is seen for the first time as $7/2^+ \rightarrow 1/2^+$ $M3$ de-excitation. Besides this, the 525 keV spin has been uniquely determined as $7/2^-$. The multipole character of 204, 208 and 321 keV transitions has been determined more precisely than before.

Acknowledgement

The authors are grateful to Prof C S Khurana, Head, Physics Department, for providing the necessary facilities and encouragement. One of the authors (KS)

is thankful to CSIR, New Delhi, for the award of a junior research fellowship.

References

1 Tamura T, Matismoto Z & Ohshima M, *Nuclear Data Sheets*, **32** (1981) 497.

2 Mazets E P & Sergeenkov V Yu, *Izv Akad Nauk SSSR Ser Fiz* (*USSR*), **30** (1966) 1185.

3 Inamura T, *J Phys Soc Jpn* (*Japan*), **24** (1968) 1.

4 Stone N J, Frankel R B & Shirley D A, *Phys Rev* (*USA*), **172** (1968) 1243.

5 Nagpal T S & Gaucher R E, *Can J Phys* (*Canada*), **48** (1970) 2978.

6 Gupta J B, Singhal N C & Hamilton J H, *Z Phys* (*Germany*), **261** (1973) 137.

7 Mann K C, Payne F A & Chaturvedi R P, *Can J Phys* (*Canada*), **42** (1964) 1700.

8 Andrew H R, Knott T F, Greenebaum B & Pipkin F M, *Phys Rev* (*USA*), **169** (1968) 978.

9 Walters W B & Meyer R A, *Phys Rev C* (*USA*), **14** (1976) 1925.

10 Barrette J, Barrette M, Haroutunian R *et al.*, *Phys Rev C* (*USA*), **11** (1975) 282.

11 Yates M L J, *Finite solid angle corrections in alpha, beta and gamma ray spectroscopy*, edited by K Siegbahn (North-Holland, Amsterdam), 1968, 1691.

12 Arns A G & Wiedenbeck M L, *Phys Rev* (*USA*), **111** (1958) 1631.

13 Auble R L, *Nucl Data Sheets*, **7** (1972) 465.

14 Ferentz M & Rosenzweig N, *Tables of angular correlation coefficients, in alpha, beta and gamma ray spectroscopy*, edited by K Siegbahn (North-Holland, Amsterdam), 1968, 1687.

15 Verma H R, *The decay characteristics of some radioactive nuclei*, Ph D thesis, Panjab University, Chandigarh, 1979.

16 Gehrke R J, Helmer R G & Greenwood R C, *Nucl Instrum Methods*, (*Netherlands*), **147** (1977) 405.

Indian Journal of Pure & Applied Physics
Vol. 21, January 1983, pp 25-27

Non-Abelian Gauge Theory of Fields Associated with Dyons

B S RAJPUT & SATYA RAJ KUMAR*
Department of Physics, Kumaun University, Naini Tal 263002

Received 31 *March* 1982

A suitable Lorentz invariant non-Abelian gauge theory of the fields associated with dyons has been constructed to describe the dual dynamics between colour isocharges and topological charges. It has been shown that the generalized particle current is gauge covariant and not conserved in non-Abelian theory. It has also been shown that in this theory the unphysical string variables and unphysical charged fields are not needed and that any extra constraint to maintain the dual symmetry of field equation and Lagrangian is also not needed.

Starting with the idea of Cabibbo and Ferrari[1] of two four-potentials, Rajput *et al.*[2-5] have made attempts to develop the consistent quantum field theory of generalized electromagnetic fields produced by particles (dyons), each carrying the generalized charge as a complex quantity (real and imaginary parts) with electric and magnetic charges. In two recent papers, Rajput and Joshi[6,7] have undertaken the study of the gauge invariant properties of generalized four-potential describing the generalized electromagnetic fields and it has been shown that the generalized fields associated with dyons cannot be described by Abelian gauge theory and that the sensible gauge theory for dyons is non-Abelian one.

Non-Abelian gauge theory can be viewed as the Einstein theory of gravitation in a higher-dimensional, unified space[8] which consists of four-dimensional space time and n-dimensional internal group space. In such a theory, the field has n-fold internal multiplicity and the multiplet $F^j (j = 1, \ldots n)$ of gauge field transforms as a basis of adjoint representation of n-dimensional non-Abelian gauge symmetry group. The generalized field equations for non-Abelian gauge fields of dyons can then be written as:

$$\{\partial^\nu \delta^{jk} + q f^{jkl} (V^*)^{l\nu}\} G^k_{\mu\nu} = J^j_\mu \equiv j^j_\mu - i\kappa^j_\mu \qquad \ldots(1)$$

where $\mu, \nu = 0, 1, 2, 3$, are the variables representing the external degree of freedom associated with four-dimensional space time; $j, k, l = 1, \ldots n$, represent the internal degree of freedom associated with n-dimensional internal group space; f^{jkl} are the group structure constants; $\{V^j_\mu\} (= \{A^j_\mu\} - i\{B^j_\mu\})$ is the generalized four-potential (A^j_μ and B^j_μ being the electric and magnetic four-potentials) and J^j_μ is the generalized four-current with j^j_μ and κ^j_μ as electric and magnetic four-current multiplets. The generalized charge on the dyon is $q (= e - ig)$ where e and g are electric and magnetic charges and $G^j_{\mu\nu}$ is given by:

$$G^j_{\mu\nu} \equiv F^j_{\mu\nu} - i F^{(d)j}_{\mu\nu} + q f^{jkl} V^k_\mu V^l_\nu \qquad \ldots(2)$$

where

$$F^j_{\mu\nu} = \partial_\nu V^j_\mu - \partial_\mu V^j_\nu$$

and

$$F^{(d)j}_{\mu\nu} = 1/2\, \varepsilon_{\mu\nu\gamma\rho} F^{j\gamma\rho}$$

With the generalized field equation [Eq. (1)], the locking of external four-dimensional space with internal charge space is not essential in contrast to the result of Boulware *et al.*[9] and the equation defines a suitable theory of non-Abelian dyons. Further, it is Lorentz and gauge invariant and reduces to the field equations derived earlier[6] in the Abelian limit (for $n = 1$) when structure constants f^{jkl} in Eq. (1) vanish, reducing it into usual form where left hand side becomes linear and the right hand side contains only electric charge and current density corresponding to $g = \kappa_\mu = B_\mu = 0$. It may also be shown[10] that the known explicit point monopoles are the solutions of Eq. (1) for the suitable currents.

Generalized four-current of Eq. (1) may be written as follows:

$$J^j_\mu(x) = q\bar{\psi}_{1/2}(x)\gamma_\mu T^j \psi_{1/2}(x) \qquad \ldots(3)$$

where the matrices T satisfy the following commutation relations in group space;

$$(T^j, T^k) = f^{jkl} T_l \qquad \ldots(4)$$

and $\psi_{1/2}(x)$ is the wavefunction of massless fermions. This generalized current is not conserved in ordinary space contrary to Abelian case, but the generalized conservation law of this current may be written in terms of gauge covariant derivative defined as:

$$\nabla^\nu = \partial^\nu + q \vec{V}^{*\nu} X \qquad \ldots(5)$$

where the cross product X and the vector sign $\rightarrow$ are denoted in internal space. Then Eq. (1) may be written as:

$$\nabla^\nu \vec{G}_{\mu\nu} = \vec{J}_\mu$$

which gives the required conservation as:

$$\nabla^\mu \vec{J}_\mu = 0 \qquad \ldots(6)$$

In the non-Abelian theory the local gauge transformation may be generalized into the following

form:

$$\vec{V}_\mu(x) \equiv \vec{V}_\mu(x) + \vec{V}'_\mu(x) \qquad \ldots(7)$$

where

$$\vec{V}'_\mu(x) = (\partial_\mu + q\vec{V}^*_\mu X)\Lambda_q \equiv \nabla_\mu \vec{\Lambda}_q$$

i.e.

$$\vec{V}'^j_\mu = q f^{jkl} V^{*k}_\mu(x)\Lambda^l_q(x) + \partial_\mu \Lambda^j_q(x)$$

and the gauge term $\Lambda^j_q(x)$ is given by the following equations in terms of electric and magnetic gauge terms:

$$\Lambda^j_q(x) = \Lambda^j_e(x) - i\Lambda^j_g(x)$$

With these results it readily follows that the local gauge changes in the generalized fields and current for the invariance of field equations in this non-Abelian gauge theory are given as follows in the group space:

$$\vec{G}'_{\mu\nu}(x) = q[\vec{G}^*_{\mu\nu}(x) X \vec{\Lambda}_q(x)]$$

and

$$\vec{J}'_\mu(x) = q[\vec{J}_\mu(x) X \vec{\Lambda}_q(x)] \qquad \ldots(8)$$

from which we get

$$\nabla^\mu \vec{J}'_\mu = 0 \qquad \ldots(9)$$

which ensures the gauge covariance of the generalized current. In other words the generalized particle current, though not conserved in non-Abelian theory, is gauge covariant and consequently Eq. (1) is invariant to a non-trivial local gauge group, contrary to Abelian theory[6]. Further, we do not need any extra constraint to maintain the dual symmetry of Eq. (1) in non-Abelian theory in contrast to the result of Brandt and Neri[10]. Rather, the following condition of proportionality of the electric and magnetic four-potentials, gauge terms and four-current densities with the corresponding charges, which has been used to derive Eqs (1) and (8), is sufficient to maintain this dual symmetry:

$$\frac{B^j_\mu}{A^j_\mu} = \frac{\Lambda^j_q}{\Lambda^j_e} = \frac{\kappa^j_\mu}{\mathcal{J}^j_\mu} = -\frac{g}{e} \qquad \ldots(10)$$

which does not lead to the constancy of these ratios but simply gives the proportionality of electric and magnetic constituents of generalized four-potential, four-current, gauge changes and generalized charge on one dyon. For another dyon this ratio need not be the same and hence no duality transformation can wash out the magnetic charges, magnetic potentials and magnetic current of all the dyons simultaneously. As such, the presence of pole (magnetic charge) in the present theory is not a formal one but has far reaching consequences. It has already been shown in an earlier paper[7] that a pure rotation in charge space or its arbitrary combination with a transformation containing simultaneously space and time reflections is an invariant transformation of field equation, corresponding Lagrangian density and the equation of motion and that these equations are also invariant under the combination of pure reflection in charge space with space reflection or time reflection (not both).

Suitable Lagrangian density yielding the field equation [Eq. (1)] of the non-Abelian gauge theory can be written in the form:

$$\mathcal{L} = -1/4 G^{j2}_{\mu\nu} - i\bar{\psi}^j_{1/2}\gamma^\mu(\partial_\mu - iqV^j_\mu T^j)\psi^j_{1/2} \qquad \ldots(11)$$

where to simplify the matter the massless fermions have been considered. This equation shows that the generalized source density couples with the electric and magnetic four-potentials in the symmetric way. This Lagrangian is dual invariant[10] subject to constraint (10). The corresponding Hamiltonian density may be written as follows:

$$H(x) = \sum_{\alpha=1}^{3}\left[1/2 G^{j2}_{\alpha,0} - \psi^j_{1/2} i\gamma^\alpha(\partial_\alpha - iqV^j_\alpha T^j)\psi^j_{1/2}\right] \qquad \ldots(12)$$

The second-quantized reduced expansions of spatial and temporal parts of the generalized four-potential have been derived[6] in the following terms of irreducible representations of Poincare group for zero mass system:

$$\vec{V}^j(x) = (8\pi^2)^{-1/2}\sum_{\alpha=\pm1}\int\frac{d\vec{p}}{p}[(1-\lambda)g^j(\vec{p},\lambda)\vec{\sigma}(p,\lambda) \times \exp\{i(\vec{p}.\vec{x}-pt)\} + (1+\lambda)g^{*j}(\vec{p},\lambda)\vec{\sigma}^*(\vec{p},\lambda) \times \exp\{-i(\vec{p}.\vec{x}-pt)\}] \qquad \ldots(13)$$

and

$$V^j_0(x) = \frac{q}{8\pi^3}\int\frac{dp}{p^3}[f^j(\vec{p})\exp\{i(\vec{p}.\vec{x}-pt)\} + k^{*j}(\vec{p})\exp\{-i(\vec{p}.\vec{x}-pt)\}]$$

where the symbol $\rightsquigarrow$ denotes the vector quantity in the external usual space time; the vector $\vec{\sigma}(\vec{p},\lambda)$ is given by:

$$\vec{\sigma}(\vec{p},\lambda) = \begin{bmatrix} \dfrac{p_1(p_1+i\lambda p_2)}{p(p+p_3)} - 1 \\ \dfrac{p_2(p_1+i\lambda p_2)}{p(p+p_3)} - i\lambda \\ \dfrac{(p_1+i\lambda p_2)}{p} \end{bmatrix} \qquad \ldots(14)$$

and $g(\vec{p},\lambda)$ and $g^*(\vec{p},\lambda)$ are the annihilation and creation operators of photon of helicity λ; $f(\vec{p})$ and $k^*(\vec{p})$ are annihilation and creation operators of massless scalar particles with positive and negative energies. Using the Bose commutation rules:

$$[g^j(\vec{p},\lambda), g^{*l}(\vec{p}',\lambda')] = p\delta_{jl}\,\delta(\vec{p}-\vec{p}')$$

$$[f^j(p), f^{*l}(p')] = [k^j(p), k^{*j}(p')] = p\delta(p-p')\delta_{jl}$$

and another commutation vanishing, we get the following equal-time commutation relations:

$$[V^j_\mu(x), V^l_\nu(x')] = 0; \quad [V^j_m(x), V^{*l}_0(x')] = 0$$

$$[V^j_m(x), V^{*l}_n(x')]$$

$$= 4\pi i \delta_{jl}\left[\delta_{mn} + i\varepsilon_{mnr}\frac{\nabla r}{\nabla} - \frac{\nabla_m \nabla_n}{\nabla^2}\right]\Delta(x - x')$$

where

$$\Delta(x - x') = \frac{1}{(2\pi)^3}\int \frac{d\vec{p}}{p} \sin i\vec{p}.(x - x')$$

In Abelian limit these relations reduce to the local commutation rules derived by Rajput and Joshi[6] in an earlier paper.

Using the reduced expansions and the corresponding reduced expansions[6] for the second-quantized operators $\bar{\psi}_{1/2}(x)$ in the expansions (11) and integrating once the volume in space, we get the following expression for the total-field Hamiltonian:

$$H_T = H_\gamma + H_M + H_I \qquad \ldots(15)$$

where H_γ, H_M and H_I, given by the following equations, are respectively the electromagnetic free-field Hamiltonian, Dirac free-field Hamiltonian, and the interaction Hamiltonian in internal group space:

$$H_\gamma = 4\pi \int d\vec{p}[g^{*j}(\vec{p}, -1)g^j(\vec{p}, -1) + g^j(\vec{p}, +1)g^{*j}(\vec{p}, +1)] \qquad \ldots(16a)$$

$$H_M = \int dp[f^{*j}(\vec{p})f^j(\vec{p}) - k^j(\vec{p})k^{*j}(\vec{p})] \qquad \ldots(16b)$$

$$H_I = \frac{qq^*}{8\pi^3}\int \frac{d\vec{p}}{p^4}[f^j(\vec{p})f^{*j}(\vec{p}) + k^{*j}(\vec{p})k^j(\vec{p})] \qquad \ldots(16c)$$

In deriving expressions 16(a-c), the reduced expansions of generalized four-potential and the field operators $\psi^j_{1/2}(x)$ in terms of Lomont-Moses realization of irreducible representation of Poincare group for zero mass system, have been used in the Hamiltonian density and the volume integration on ordinary space (x_μ) has been carried out. Dirac Hamiltonian H_M is the contribution of second term of Hamiltonian given by Eq. (12), i.e. the term $-i\bar{\psi}^j_{1/2}\gamma_\mu\partial_\mu\psi^j_{1/2}$ in which the combinations of spin 1/2 field amplitudes of Dirac particle appearing in the reduced expansions of $\bar{\psi}^j_{1/2}$ and $\psi^j_{1/2}$, behave as creation and annihilation operators $f^j(p)$, $f^{*j}(p)$; $k^j(p)$ and $k^{*j}(p)$ in the external space. Interaction Hamiltonian H_I may be interpreted as the contribution of the term $(\vec{J}_0 . \vec{V}_0)$, where the other term $(\vec{J}.\vec{V}^T)$ vanishes in zero mass system since no charge or current sources are associated with the transverse part. As such, photons' creation and annihilation operators do not contribute to interaction Hamiltonian H_I. Eq. (16c) also shows that the interaction depends on the square of the modulus of generalized charge which vanishes only when $e = g = 0$. The appearance of qq^* in H_I shows that the interaction between generalized charges q_i and q_j depends on electric and magnetic coupling parameters $\alpha_{ij}(= e_ie_j + g_ig_j)$ and $\mu_{ij}(= e_ig_j - e_jg_i)$ respectively.

Though the generalized particle current given by Eq. (3) is not conserved in the non-Abelian theory, the following conserved Notherian current corresponding to global gauge group can be constructed from it:

$$\mathcal{J}^j_\mu = J^j_\mu - qf^{jkl}V^{*kv}G^l_{\mu\nu} \qquad \ldots(17)$$

subject to the constraint given by Eq. (10).

Then the field Eq. (1) may be written in the following usual form:

$$\partial^\nu G^j_{\mu\nu} = \mathcal{J}^j_\mu \qquad \ldots(18)$$

This generalized Notherian current $\mathcal{J}_\mu$ receives the contribution from both the particle sources and the gauge fields and it is non-vanishing even if the generalized particle current J_μ is vanishing. Furthermore, this conserved current is not gauge covariant because of non-covariance of $\vec{G}_{\mu\nu}$. Constraint (10) is the condition of consistency of non-Abelian field Eqs (1) and (18), the gauge transformation (7) and covariance Eq. (8). This constraint requires the following condition for the matrices T:

$$T^j = T^{(d)j}$$

in agreement with the results of Thebaud[11]. Any extra constraint need not be imposed to maintain the dual symmetry in this non-Abelian theory. This gauge theory of non-Abelian monopoles has a built-in dual structure and may describe the dual dynamics between colour isocharges and the topological charges of non-Abelian symmetry in terms of two potentials in a dual symmetric way. A similar attempt has recently been made by Cho[12] but his theory suffers from the serious shortcoming that one of the dual potentials describes the corresponding field with a space-like potential and contains unphysical string singularities. On the contrary, in the present theory the electric and magnetic quantities appear more symmetrically and do not contain the unphysical string variables and the unphysical charged fields. In our forthcoming paper, we shall use the built-in duality described here, for undertaking the study of the problem of quark confinement.

References

1 Cabibbo N & Ferrari E, *Nuovo Cimento (Italy)*, **23** (1962) 1147.
2 Rajput B S & Prakash Om, *Indian J Phys*, **50** (1976) 929; **53A** (1979) 274; **54A** (1980) 11.
3 Rajput B S & Prakash Om, *Indian J Pure & Appl Phys*, **16** (1978) 593.
4 Rajput B S & Joshi D C, *Indian J Pure & Appl Phys*, **18** (1980) 988.
5 Rajput B S & Joshi D C, *Pramana (India)*, **13** (1979) 637.
6 Rajput B S & Joshi D C, *Hadronic J (USA)*, **4** (1981) 1805.
7 Rajput B S & Joshi D C, *Phys Rev D (USA)*, (1981) in press.
8 Cho Y M, *J Math Phys (USA)*, **16** (1975) 2029.
9 Boulware D G, Brown L S, Cahn R N *et al.*, *Phys Rev D (USA)*, **14** (1976) 2708.
10 Brandt R A & Neri F, *Nucl Phys B (Netherlands)*, **145** (1978) 221.
11 Thebaud L R, *Phys Rev D (USA)*, **14** (1976) 1693.
12 Cho Y M, *Phys Rev D (USA)*, **21** (1980) 1080.

Indian Journal of Pure & Applied Physics
Vol. 21, January 1983, pp 28-32

Study of Emission of Cerenkov Radiation by Tachyons

O P S NEGI* & B S RAJPUT
Department of Physics, Kumaun University, Naini Tal 263002

Received 31 *March* 1982

The emission of Cerenkov radiation by tachyons has been examined by using the reduced expansions of superluminal electromagnetic fields in terms of standard helicity representation of Poincare group. It has been shown that the tachyons emit Cerenkov radiation through their coupling only with subluminal electromagnetic fields and that a charged tachyon can emit Cerenkov radiation only in the media in which it travels with a velocity lower than that of light while in the usual medium in which its velocity is more than that of light, it will never emit Cerenkov radiation.

1 Introduction

There have been controversies about the possibilities of developing a self-consistent quantum field theory of tachyons and making the predictions for the experiments involving electromagnetic Cerenkov radiation by tachyons. In an attempt to construct a self-consistent theory of tachyons, in two recent papers[1,2], we have derived the reduced expansions of fields associated with tachyons in terms of standard helicity representations of Poincare group[3,4] by using real tachyonic transformations of Antippa[5] and used them to develop the Lorentz invariant second quantized field theory of tachyons of spin-1 and spin-$\frac{1}{2}$ respectively[2,6].

The resolution of controversies about the emission of Cerenkov radiation by tachyons is equally important since most of the experimental work for the detection of tachyons has actually been aimed to detect such a radiation supposedly emitted by tachyons[7-11]. First experimental evidence for the existence of tachyons was stated by Clay and Crouch[12] on the assumption that they emit Cerenkov radiation and that the charged tachyons could give signals in a scintillation counter. The formula used by these workers was shown[13] to be invalid and no quantitative predictions could be made for experiments involving electromagnetic Cerenkov emission of tachyonic elementary particles. All the experiments were uncritically founded on the extension of the usual Cerenkov effect formulae suggested by Sommerfeld[14] in prerelativistic time when he postulated the Maxwell's equations to be valid even for superluminal source. Such a groundless and unjustified extension led to the difficulties and inconsistencies and all these experiments failed to detect tachyons since these were founded on a wrong hypothesis. On similar grounds the formulae derived by Lapedes and Jacobs[15] and Schulman[16] are invalid.

In our earlier papers[17,18], it has been shown that in superluminal (SPL) frames the superluminal electromagnetic (SPL-EM) fields obey the differential equations which differ from Maxwell's equations and that the force acting on a charged tachyon in SPL frame is not a Lorentz force. In the light of these facts, the results[19-22] of emission of Cerenkov radiation by a charged tachyon, derived on the assumption of invariance of Maxwell's equations under SPL Lorentz transformations and the Coulombian nature of the field of a SPL charge, are not correct. The analysis of Cerenkov radiation[23-25] is based on the extension of usual formulae for the differential energy loss through Cerenkov radiation from bradyons by assuming the covariance of vacuum under generalized Lorentz transformations.

Without making any such unfounded assumptions in the present paper, we have re-examined the question of emission of Cerenkov radiation by tachyons by using our reduced expansions of SPL-EM fields[1] in terms of standard helicity representations of Poincare group. Using the reduced expansions of transverse SPL-EM fields in space-momentum and energy-time representations respectively, it has been shown that the tachyons emit the Cerenkov radiation through their coupling with subluminal (SBL) EM fields but not with SPL fields. It has also been shown that if any Cerenkov radiation is emitted at all by the tachyons moving along the tachyon-corridor (T-C) in vacuum due to its coupling with SBL-EM fields transverse with respect to T-C, it is emitted only in the positive direction of T-C. The strength of Cerenkov radiation thus emitted has been shown to be much less than that expected from the calculations of Alvager and Kreistler[8].

Starting with the expression of force acting on a charged tachyon moving along T-C due to its coupling with transverse SPL-EM fields propagating along T-C,

it has been shown that a charged tachyon can emit the Cerenkov radiation only in the medium in which it travels with a velocity lower than that of light while in the usual medium in which its velocity is more than that of light, it will never emit the Cerenkov radiation. It has also been shown that a charged tachyon induces the Cerenkov radiation in a medium in which the phase velocity of SPL-EM fields exceeds the velocity of the tachyon. In the derivation of all these results, we have chosen the direction of propagation of tachyons and the SPL-EM fields along T-C. The description of Cerenkov radiation in the case when the tachyons or the superluminal fields do not move along T-C is more complicated, and has not been attempted in this paper.

2 Reduced Expansions of SPL-EM Fields

The reduced expansions of the transverse SPL-EM fields and potential associated with spin-1 tachyons have been derived in the following form[1] in terms of standard helicity representation of Poincare group by using real SPL Lorentz transformations[5]:

$$\mathbf{E}^T(x) = \frac{i}{4\pi^{3/2}} \sum_{\lambda=\pm 1} \frac{\lambda}{2^{1/2}} \int_{|\mathbf{p}|\geq k} d\mathbf{p} [\hat{f}(\mathbf{p}, \lambda)\boldsymbol{\sigma}(\mathbf{p}, \lambda) \times \exp\{i(\mathbf{p}.\mathbf{x} - \omega x_3)\} - \hat{h}^*(\mathbf{p}, \lambda)\boldsymbol{\sigma}^*(\mathbf{p}, \lambda) \times \exp\{-i(\mathbf{p}.\mathbf{x} - \omega x_3)\}] \quad \ldots(1)$$

$$\mathbf{H}^T(x) = \frac{1}{4\pi^{3/2}} \sum_{\lambda=\pm 1} \frac{1}{2^{1/2}} \int_{|\mathbf{p}|\geq k} \frac{d\mathbf{p}}{\omega(k, \mathbf{p})} p [\hat{f}(\mathbf{p}, \lambda)\boldsymbol{\sigma}(\mathbf{p}, \lambda) \times \exp\{i(\mathbf{p}.\mathbf{x} - \omega x_3)\} + \hat{h}^*(\mathbf{p}, \lambda)\boldsymbol{\sigma}^*(\mathbf{p}, \lambda) \times \exp\{-i(\mathbf{p}.\mathbf{x} - \omega x_3)\}] \quad \ldots(2)$$

$$\mathbf{A}^T(x) = \frac{1}{4\pi^{3/2}} \sum_{\lambda=\pm 1} \frac{\lambda}{2^{1/2}} \int_{|\mathbf{p}|\geq k} \frac{d\mathbf{p}}{\omega(k, \mathbf{p})} [\hat{f}(\mathbf{p}, \lambda)\boldsymbol{\sigma}(\mathbf{p}, \lambda) \times \exp\{i(\mathbf{p}.\mathbf{x} - \omega x_3)\} + \hat{h}^*(\mathbf{p}, \lambda)\boldsymbol{\sigma}^*(\mathbf{p}, \lambda) \times \exp\{-i(\mathbf{p}.\mathbf{x} - \omega x_3)\}] \quad \ldots(3)$$

where

$$\boldsymbol{\sigma}(\mathbf{p}, \lambda) = \begin{bmatrix} \frac{p_1(p_1 + i\lambda p_2)}{p(p + p_3)} - 1 \\ \frac{p_2(p_1 + i\lambda p_2)}{p(p + p_3)} - i\lambda \\ \frac{p_1 + i\lambda p_2}{p} \end{bmatrix} \quad \ldots(4)$$

and $\hat{f}(\mathbf{p}, \lambda)$ and $\hat{h}^*(\mathbf{p}, \lambda)$ are the representations of amplitude of wavefunction of positive and negative energy with helicity $\lambda = \pm 1$ and

$$d\mathbf{p} = p^2 dp \sin\theta d\theta d\varphi$$

and

$$\mathbf{p}.\mathbf{x} = p_1 x_1 + p_2 x_2 + p_3 t \quad \ldots(5)$$

Energy eigenvalue $\omega(k, \mathbf{p})$ is given by the following equation in terms of mass k and momentum $\mathbf{p}$:

$$\omega = (|\mathbf{p}|^2 - k^2)^{1/2} \quad \ldots(6)$$

the reality of which requires

$$|\mathbf{p}| \geq k \quad \ldots(7)$$

Using these reduced expansions (1) and (2), the Lorentz-invariant second-quantized theory of spin-1 tachyons has been constructed[6] in terms of non-Hermitian field operators and it has been shown that the tachyons are not localized in space and that the spin-statistics relationship need not be inverted for the Lorentz invariance[26] of the theory.

Restricting the propagation of spin-1 tachyons along T-C fixed along the Z-axis, i.e. $\sigma_3 = 0 \Rightarrow \mathbf{p} = (0, 0, p)$, and keeping in mind the reciprocity principle[5] (according to which the roles of time and space and those of energy and momentum are interchanged) under SPL Lorentz transformations, the reduced expansions (1), (2) and (3) may be written in the following forms in time-energy representation:

$$\mathbf{E}^T(x) = \frac{i}{4\pi^{3/2}} \sum_{\lambda=\pm 1} \frac{\lambda}{2^{1/2}} \int d\omega [\hat{f}(\omega, \lambda)\boldsymbol{\sigma}(\lambda) \times \exp\{-i(\omega t - \mathbf{p}.\mathbf{x})\} - \hat{h}^*(\omega, \lambda)\boldsymbol{\sigma}^*(\lambda) \times \exp\{i(\omega t - \mathbf{p}.\mathbf{x})\}] \quad \ldots(8)$$

$$\mathbf{H}^T(x) = \frac{1}{4\pi^{3/2}} \sum_{\lambda=\pm 1} \frac{1}{2^{1/2}} \int \frac{d\omega}{p} \omega [\hat{f}(\omega, \lambda)\boldsymbol{\sigma}(\lambda) \times \exp\{-i(\omega t - \mathbf{p}.\mathbf{x})\} + \hat{h}^*(\omega, \lambda)\boldsymbol{\sigma}^*(\lambda) \times \exp\{i(\omega t - \mathbf{p}.\mathbf{x})\}] \quad \ldots(9)$$

$$\mathbf{A}^T(x) = \frac{1}{4\pi^{3/2}} \sum_{\lambda=\pm 1} \frac{\lambda}{2^{1/2}} \int \frac{d\omega}{p} [\hat{f}(\omega, \lambda)\boldsymbol{\sigma}(\lambda) \times \exp\{-i(\omega t - \mathbf{p}.\mathbf{x})\} + \hat{h}^*(\omega, \lambda)\boldsymbol{\sigma}^*(\lambda) \times \exp\{i(\omega t - \mathbf{p}.\mathbf{x})\}] \quad \ldots(10)$$

where

$$\boldsymbol{\sigma}(\lambda) = \begin{pmatrix} -1 \\ -i\lambda \\ 0 \end{pmatrix} \quad \ldots(11)$$

Applying the reinterpretation principle[27] in which a tachyon that appears to be moving backward in time

corresponds to an antitachyon moving in opposite direction, we get

$$\hat{f}^*(\omega, \lambda) = \hat{h}^*(\omega, \lambda) \quad \ldots(12)$$

Then reduced expansions (8), (9) and (10) will give the Hermitian field operators for which causality will not be violated in energy-time (ω-t) representation.

3 Possibility of Emission of Cerenkov Radiation by Tachyons

Tachyons are simply ordinary particles which are instantaneously at rest in inertial frames whose velocities are superluminal with respect to an ordinary observer. They behave as bradyons in SPL frame. SPL-EM fields given by reduced expansions (1) and (2) couple with the tachyons according to the usual Maxwell's equations while these reduced expansions when viewed upon from a SBL frame do not satisfy the usual Maxwell's equations[18]. One must, therefore, be careful to distinguish between SBL- and the SPL-EM fields in tachyon theories based on the existence of the SPL reference frame and the tachyon-bradyon reciprocity. In SBL frames, SPL-EM fields obey the field equations which differ from the Maxwell's equations and are not invariant. Tachyons interact among themselves via SPL-EM fields as observed in SBL reference frame and the force exerted on a charged tachyon by SBL-EM fields has the form of SPL rather than of ordinary force. We, therefore, disagree with Lemke[19,20] since SPL-EM fields cannot be identified with the ordinary SBL fields. We have also shown[18] that the force acting on a charged tachyon in a SPL-EM field is not a Lorentz force and that the electrically charged tachyon interacting with SPL fields behaves neither as a pure electric charge nor as a pure magnetic charge. In the light of these facts, the results of Lemke[19,20] of emission of Cerenkov radiation by charged tachyons, derived on the assumptions of invariance of the Maxwell's equations under SPL Lorentz transformations and the Coulombian nature of field of a SPL charge, are not correct. Similar is the case with the results of Wimmel[21,22], who has also assumed the invariance of the Maxwell's equations under SPL Lorentz transformations.

Let us re-examine the question of emission of Cerenkov radiation by tachyons in vacuum using the reduced expansions (1) and (2) of the transverse SPL-EM fields. We get the intensity of energy flow per unit area per second, i.e. Poynting vector $\hat{S}$ as:

$$\hat{S} = \sum_{\lambda=\pm 1} \int_{\mathbf{p}\lambda} \frac{d\mathbf{p}}{2\omega} [\hat{f}(\mathbf{p}, \lambda), \hat{h}^*(\mathbf{p}, \lambda)] \quad \ldots(13)$$

From the commutation rule of operators $\hat{f}(\mathbf{p}, \lambda)$ and $\hat{h}^*(\mathbf{p}, \lambda)$ as discussed earlier[18] on the theory of second quantization of spin-1 tachyons, we get

$$[\hat{f}(\mathbf{p}, \lambda), \hat{h}^*(\mathbf{p}, \lambda)] = 0 \quad \ldots(14)$$

and hence Eq. (11) gives

$$\hat{S} = 0 \quad \ldots(15)$$

which shows that the rate of energy flow per unit area due to SPL radiation field is zero. In other words, the tachyons do not emit any type of radiation in position-momentum representation. As such, the possibility of emission of Cerenkov radiation from a space-like particle does not arise in this representation.

The SPL-EM fields given by Eqs (8) and (9) in time-energy representation behave as SBL ones so far as their Hermitian nature is concerned. In this representation the commutation rule of the field operator is given by the equation

$$[\hat{f}(\omega, \lambda), \hat{f}^*(\omega', \lambda')] = \delta(\omega - \omega')\delta_{\lambda\lambda'} \quad \ldots(16)$$

and then the Poynting vector $\hat{S}$ becomes:

$$\hat{S} = \sum_{\lambda=\pm 1} \int d\omega \left(\frac{\mathbf{p}}{p}\right) \delta(\omega - \omega')\delta_{\lambda\lambda'} = 2\hat{k} \quad \ldots(17)$$

were $\hat{k}$ is a unit vector in the direction of T-C. This equation shows that the energy flow per unit area per second due to SPL radiation field is not zero. In other words, a tachyon will emit Cerenkov radiation through its coupling with SPL-EM fields in time-energy representation. But it has been pointed out that the SPL-EM fields in time-energy representation behave as SBL ones and as such the tachyons emit the Cerenkov radiation in vacuum through their coupling to SBL-EM fields but not to SPL fields. In other words, the tachyons in free space will not emit SPL photons, i.e. the quanta of SPL-EM fields via the Cerenkov effect just as a bradyon in free space cannot emit ordinary photon, i.e. quanta of SBL-EM fields. It may also be shown, using the tachyon-bradyon reciprocity, that a bradyon will emit Cerenkov radiation through its coupling with SPL-EM field in position-momentum representation.

The non-emission of Cerenkov radiation in vacuum by a charged tachyon can be seen from a kinematical point of view also. We have shown in our earlier paper[18] that under the real SPL Lorentz transformations, the space coordinate along the direction of relative motion (T-C) gets interchanged with time. In other words if the Z-axis is chosen along T-C, the space $\{x_\mu\} = (it, x, y, z)$ of the frame K is mapped on to the space $\{X_\mu\} = (iz, x, y, t) = (iT, X, Y, Z)$ of the frame K', where the frame K' moves with SPL velocity along the Z-axis relative to the frame K. Similar mapping takes place for the components of EM four-potential $\{A_\mu\}$ under real SPL Lorentz transformations, i.e.

$$\{A_\mu\} = (i\varphi, A_1, A_2, A_3) \to (iA_3, A_1, A_2, \varphi) = (i\varphi, B_1, B_2, B_3) = \{B_\mu\} \quad \ldots(18)$$

The energy-time representation discussed above is given in space $\{X_\mu\}$ in terms of four-potential $\{B_\mu\}$. In this space, the reduced expansions (8), (9) and (10) for the transverse fields in time-energy representation satisfy the following relations of transverse SBL fields:

$$\mathbf{E} = -\frac{\partial \mathbf{B}}{\partial T}, \quad \mathbf{H} = (\nabla \times \mathbf{B}) \qquad \ldots(19)$$

where the differential operator ∇ has been defined in the space $\{X_\mu\}$. These equations, when viewed upon from SBL frame K (i.e. transformed to space $\{x_\mu\}$, will have the following forms:

$$E_x = \frac{\partial A_x}{\partial z} + \frac{\partial A_z}{\partial x}; \quad H_x = \frac{\partial \varphi}{\partial y} - \frac{\partial A_y}{\partial t}$$

$$E_y = \frac{\partial A_y}{\partial z} + \frac{\partial A_z}{\partial y}; \quad H_y = \frac{\partial \varphi}{\partial x} - \frac{\partial A_x}{\partial t}$$

$$E_z = \frac{\partial \varphi}{\partial z} - \frac{\partial A_z}{\partial t}; \quad H_z = (\nabla \times \mathbf{A})_z \qquad \ldots(20)$$

which are similar neither to corresponding equations for electric charge source nor to those for magnetic charge source.

The force acting on the electrically charged tachyon when it interacts with transverse SPL-EM field in space $\{X_\mu\}$ may be written as:

$$F = e\frac{\partial \mathbf{B}}{\partial T} + e\mathbf{w} \times (\nabla \times \mathbf{B}) \qquad \ldots(21)$$

where $\mathbf{w}$ is the velocity in space $\{X_\mu\}$ and may be written as $d\mathbf{X}/dT$. If we restrict the motion of the charged tachyon along T-C which is the direction of Z-axis in space $\{x_\mu\}$, $\mathbf{w}$ may then be written as

$$\mathbf{w} = \left(0, 0, \frac{dt}{dz}\right) \qquad \ldots(22)$$

which behaves as inverse velocity in $\{x_\mu\}$ space and may be written as $\overleftarrow{v}$.

Using mapping (18) and substituting the reduced expansion (3) after writing it in space $\{X_\mu\}$ into Eq. (21) of the force and then differentiating with respect to tachyon energy ω given by Eq. (6), we get

$$\frac{d\mathbf{F}}{d\omega} = 0 \qquad \ldots(23)$$

where we have used the following value of the inverse velocity:

$$|\overleftarrow{v}| = \frac{dt}{dz} = \frac{\omega}{p} = \text{Phase velocity of tachyon} \qquad \ldots(24)$$

which is always less than unity. Eq. (23) also shows that the charged tachyons do not emit any Cerenkov radiation through their coupling to SPL-EM fields. Non-zero value of $dF/d\omega$ is obtained only when the inverse velocity given by Eq. (24) becomes more than unity. In other words, the charged tachyon can emit the Cerenkov radiation only in a SPL medium in which it travels with velocity lower than that of light, while in the usual medium in which its velocity is more than unity (in the unit of c), i.e. inverse velocity $|\overleftarrow{v}|$ is less than unity, it will never emit Cerenkov radiation.

4 Discussion

Using the reduced expansions (1) and (2) we have shown by Eq. (15) that in vacuum tachyons do not emit any type of radiation through their coupling with SPL-EM fields in space-momentum representation and consequently the possibility of emission of Cerenkov radiation from a space like particle does not arise in this representation. The similar non-emission of Cerenkov radiation by tachyons in vacuum has been shown by Recami and Mignani[23-25] by assuming the covariance of vacuum under SPL Lorentz transformations and by Marchildon *et al.*[28] by assuming the covariance of energy-momentum conservation equations. In our derivations no such assumptions have been made.

Eq. (17) shows that the tachyons will emit Cerenkov radiation in the direction of T-C through their coupling with SPL-EM fields in time-energy representation. But it has already been shown[1] that the SPL-EM fields in time-energy representation behave as SBL ones in view of their Hermitian nature, localizability, Maxwell's equations and space-time reciprocity. It may, therefore, be concluded that the tachyons emit the Cerenkov radiation through their coupling to SBL-EM fields but not to SPL fields. Eq. (17) also shows that the Cerenkov radiation due to coupling of tachyons in otherwise vacuum with SBL-EM fields is emitted only along T-C when both the tachyon and the field propagate along T-C and the field is transverse with respect to this direction. In all other directions no Cerenkov radiation in emitted by tachyons in any case in the vacuum. We may, therefore, conclude that if any Cerenkov radiation is emitted at all by the tachyons moving along T-C in vacuum due to its coupling with SBL-EM fields, it is emitted only in the positive direction of T-C. But the coupling of tachyons to the ordinary SBL-EM fields determines the tachyon-bradyon interactions. The strength of this coupling must be very small in order to avoid experimentally unacceptable manifestations of the existence of preferred direction[29] and to avoid the observable violations of rotational invariance due to virtual tachyons in bradyon physics[28]. As such the strength of Cerenkov radiation, given by Eq. (17) as the result of coupling of tachyon with SBL-EM fields, will be much less than that expected on the basis of calculations considering a particle of unit tachyonic charge[8].

The non-emission of Cerenkov radiation in vacuum by a charged tachyon has also been shown from the kinematical point of view by deriving the force given by Eq. (21) on a charged tachyon moving along T-C due to

its coupling with transverse SPL-EM fields propagating along T-C. It has been shown by Eq. (23) that the charged tachyons do not emit any Cerenkov radiation through their coupling to SPL-EM fields unless their inverse velocity given by Eq. (24) becomes more than unity (i.e. the velocity of tachyons becomes less than the velocity of light). In other words the charged tachyon can emit the Cerenkov radiation only in a medium in which it travels with the velocity lower than that of light while in the usual medium in which its velocity is more than unity (in the unit of c), it will never emit the Cerenkov radiation. Cerenkov radiation emitted in this way is therefore a function of velocity of the tachyons. As such, we agree with Lemke[20] that the charged tachyons produce Cerenkov radiation only in the media and frequency regions in which the index of refraction is < 1 (only in such media the tachyon can travel with the velocity less than that of light), and with Recami and Mignani[23,24] that the tachyons do not produce Cerenkov radiation in the usual media where the index of refraction is > 1.

Since the phase velocity of the particle is defined as $v_{ph} = \frac{\omega}{p}$, Eq. (24) supports the results of Lemke[30] that a charged tachyon induces the Cerenkov radiation in medium in which the phase velocity exceeds the velocity of tachyons. Experiments for the detection of tachyons are expected to fail because all of them are founded on the wrong hypothesis that tachyons would always emit Cerenkov radiation even at constant velocity in vacuum or in a usual bradyonic medium.

Acknowledgement

One of the authors (OPSN) is thankful to the CSIR, New Delhi, for the financial assistance.

References

1 Rajput B S, Purohit K D & Negi O P S, *Indian J Pure & Appl Phys*, **19** (1981) 1081.
2 Negi O P S & Rajput B S, *J Math Phys (USA)*, **23** (1982) 1964.
3 Moses H E, *J Math Phys (USA)*, **8** (1967) 1134.
4 Moses H E, *J Math Phys (USA)*, **9** (1968) 16.
5 Antippa A F, *Phys Rev D (USA)*, **11** (1975) 724.
6 Rajput B S, Negi O P S & Purohit K D, *Indian J Pure & Appl Phys*, **20** (1982) 22.
7 Maglic B, *Bull Am Phys Soc (USA)*, **14** (1969) 840.
8 Alvager T & Kreistler M N, *Phys Rev (USA)*, **171** (1968) 1357.
9 Davis M B, Kreistler M N & Alvager T, *Phys Rev (USA)*, **183** (1969) 1132.
10 Ramamurthy P V, *Lett Nuovo Cimento (Italy)*, **1** (1971) 908.
11 Bart D F & Lahava M D, *Phys Rev D (USA)*, **6** (1972) 1817.
12 Clay R W & Crouch P C, *Nature (GB)*, **248** (1971) 28.
13 Wimmel H K, *Nature Phys Sci (GB)*, **236** (1972) 79.
14 Sommerfeld A, *Proc K Ned Akad Wet (Netherlands)*, **7** (1904) 346.
15 Lapedes A S & Jacobs K C, *Nature Phys Sci (GB)*, **235** (1972) 6.
16 Schulman L S, *Nuovo Cimento B (Italy)*, **2** (1971) 38.
17 Rajput B S, *Proceedings of the Einstein centenary symposium, Nagpur, India* Feb. 1980 (Duhita Publisher, Nagpur) 1980, 181.
18 Negi O P S, Chandola H C, Purohit K D & Rajput B S, *Phys Lett B (Netherlands)*, **105** (1981) 281.
19 Lemke H, *Lett Nuovo Cimento (Italy)*, **12** (1975) 342, 619.
20 Lemke H, *Nuovo Cimento (Italy)*, **27A** (1975) 141.
21 Wimmel H K, *Lett Nuovo Cimento (Italy)*, **1** (1971) 645.
22 Wimmel H K, *Lett Nuovo Cimento (Italy)*, **2** (1971) 363, 674.
23 Recami E & Mignani R, *Lett Nuovo Cimento (Italy)*, **7** (1973) 388.
24 Recami E & Mignani R, *Lett Nuovo Cimento (Italy)*, **9** (1974) 362.
25 Recami E & Mignani R, *Ric Nuovo Cimento (Italy)*, **4** (1974) 209.
26 Hamamoto S, *Prog Theor Phys (Japan)*, **48** (1972) 1037.
27 Dhar J & Sudarshan E C G, *Phys Rev (USA)*, **173** (1968) 1622.
28 Marchildon L, Everett A E & Antippa A F, *Nuovo Cimento B (Italy)*, **53** (1979) 253.
29 Everett A E, *Phys Rev D (USA)*, **13** (1976) 795.
30 Lemke H, *Nuovo Cimento 4 (Italy)*, **32** (1976) 169.

Indian Journal of Pure & Applied Physics
Vol. 21, January 1983, pp 33-35

Regge Poles in the Klein-Gordon Equation

ANURADHA BHARGAVA & L K SHARMA*
Department of Applied Physics, Government Engineering College, Jabalpur 482011

Received 19 *April* 1982

The expansions for the Regge trajectories $\alpha(K)$ associated with the scattering of relativistic Klein-Gordon particles in a Yukawa potential have been obtained by the continued fraction method. These expansions have been used for calculating the trajectories on an electronic computer.

1 Introduction

A Regge trajectory may be defined as the path in α-space of a singularity $\alpha(K)$ as K is taken from $+i\infty$ to 0 and then along the positive real axis to $+\infty$. The analytic structure of the Regge trajectories for the Yukawa potential turns out to be orders of magnitude more complicated than the Coulomb trajectories[1-5]. For example, for Yukawa-type potentials, states with different values of the radial quantum number need not be linearly independent, since trajectories with different n may collide; although this usually happens when $\mathrm{Re}\, l < -\frac{1}{2}$, any attempt to write dispersion relations for trajectories[6] requires a knowledge of the analytic structure, even in the unphysical regions. The study of Regge poles is of relevance because they determine the asymptotic behaviour of the S-matrix, when one of its variables is large. This has only been proved in potential scattering[7-9] but it has been shown that it is also true in field theory[10].

In this paper, we have derived the eigenenergy and Regge trajectory expansions for the Yukawa potential using the method of continued fractions for Klein-Gordon particles. This method has also been used for obtaining these expansions for the Yukawa potential in the Schrödinger framework[11]. It may be of interest to note that continued fraction techniques have been applied to various problems in potential scattering[12-15] and in the problems of anharmonic oscillator with polynomial interaction[16-17].

Recently, large-energy asymptotic expansions of eigenenergies and Regge trajectories have been obtained for a general even-power potential in both the Schrödinger[18] and Klein-Gordon[19] framework.

2 Asymptotic Expansion and Continued Fractions for the Regge Trajectories

In this section, after obtaining various coefficients for the asymptotic expansion, the continued fractions for each of the Regge poles of Yukawa potential have been obtained as functions of K. From the coefficients of the power series expansion of $rV(r)$, we obtain corresponding coefficients of the continued fractions. These coefficients then enable us to obtain the desired Regge trajectory expansion. Since at low energies continued fractions converge very slowly, a large number of approximants have to be evaluated. For this purpose a HCL-1800 (8 bit microprocessor based) electronic computer has been used.

The radial part of the Klein-Gordon equation is given by:

$$\frac{d^2\psi(r)}{dr^2} + \left\{(E-V)^2 - m^2 - \frac{l(l+1)}{r^2}\right\}\psi(r) = 0 \qquad (\hbar = c = 1) \qquad \ldots(1)$$

Setting $E^2 = m^2 + k^2$, $K = ik$

$$Z = -2ikr, \quad X = dX\ dZ \qquad \ldots(2)$$

$$U(r) = rV(r)$$

and

$$\psi(r) = e^{ikr} r^{l+1} X(r) \qquad \ldots(3)$$

we obtain

$$Z\ddot{X} + (2l + 2 - Z)\dot{X} - \left\{(l+1) - \frac{Z}{4K^2}(V^2 - 2EV)\right\}X = 0 \qquad \ldots(4)$$

Following Mandelstam[20], we assume that $rV(r)$ is analytic near $r = 0$. Thus power-series expansion can be written as

$$U(r) = \sum_{i=0}^{\infty} M_i(-2r)^i$$

and

$$U^2(r) = \sum_{i=0}^{\infty} M_i M_i(-2r)^{i+1} \qquad \ldots(5)$$

For the wavefunction of nth Regge pole, we write an expansion in a double power-series in Z and K^{-1} as:

$$X^{(n)}(Z, K) = \sum_{p,m=0}^{\infty} F^n_{p,m} K^{-p} Z^m \qquad \ldots(6)$$

Finally, the following power-series eigenenergy expansion in powers of K^{-1} can be written as:

$$\alpha_n(K) = -n + \sum_{p=1}^{\infty} C_p^n K^{-p} \qquad \ldots(7)$$

Substituting expansions (5), (6) and (7) in (4), we get:

$$(m+1)(m+2-2n)F^n_{p,m+1} + (n-1-m)F^n_{p,m}$$
$$= \sum_{t=1}^{p+1} \{-2(m+1)C_t^n F^n_{p-t,m+1} + C_t^n F^n_{p-t,m} - EM_{t-1}F^n_{p-t,m+1-t} - P_t F^n_{p+1-t,m+2-t}\} \qquad \ldots(8)$$

where

$$P_t = \sum_{k=1}^{t} M_{k-1} M_{t-k}, \quad k = s+t \qquad \ldots(9)$$

It is found that a general potential is not consistent with Eq. (8) for making the expansion in powers of Z terminate completely. So we find the terms of some particular order in K^{-1} terminate when considered as a power series in Z. Therefore, we find a $m_0(p, n)$ such that the Ansatz

$$F^n_{p,m} = 0, \quad \text{for} \quad m \geq m_0(p, n), \quad m \neq 0 \qquad \ldots(10)$$

is consistent with Eq. (8). The elements with $m = 0$ are arbitrary normalization constants. By observing the coefficients of the various terms in Eq. (8), we find that there is only one possible Ansatz

$$m_0 = n + p - 1, \quad \text{for} \quad p > 0$$
$$m_0 = n \quad , \quad \text{for} \quad p = 0 \qquad \ldots(11)$$

which is independent of the particular potential.

Eqs (8) and (11) now give recursion formulae from which one can obtain Fs and Cs. For the first Regge pole, the coefficients of the expansion (7) are:

$$C_1^1 = EM_0 + P_2$$
$$C_2^1 = P_1[EM_1 + P_3]$$
$$C_3^1 = \frac{P_1(2+P_1)(EM_2 + P_4)}{2} + 2(EM_0 + P_2)(EM_1 + P_3)$$
$$C_4^1 = (4+P_1)(EM_0 + P_2)(EM_2 + P_4) + P_1(EM_1 + P_3)^2 + \frac{(2+P_1)}{6}(6+P_1) \times (EM_3 + P_5) + 3EM_1(EM_1 + P_3) \qquad \ldots(12)$$

For the second Regge pole, we have

$$C_1^2 = EM_0 + P_2$$
$$C_2^2 = P_1[EM_1 + P_3]$$
$$C_3^2 = \frac{4(1-P_1)}{(2-P_1)}(EM_0 + P_2)(EM_1 + P_3) - 2(2-P_1)\left(1 + \frac{P_1}{4}\right)(EM_2 + P_4)$$
$$C_4^2 = (6+5P_1)(EM_0 + P_2)(EM_2 + P_4) + (5P_1 - 2)(EM_1 + P_3)^2 - \frac{P_1(10+P_1)(2-P_1)(EM_3 + P_5)}{6} \qquad \ldots(13)$$

We have calculated four coefficients of series (7). Higher coefficients can only be calculated with the help of a computer because the series diverges too fast.

Continued fractions—We now apply the theory of continued J-fraction[21]. We can write an expression for $\alpha_n(K)$ as:

$$\alpha_n(K) = -n + \cfrac{a_0}{b_1 + K - \cfrac{a_1}{b_2 + K - \cfrac{a_2}{b_3 + K - \ldots}}} \qquad \ldots(14)$$

The divergence of k^{-1} expansion for $\alpha_n(k)$ which is due to cuts and poles in the k-plane is improved by representing $\alpha_n(K)$ as described above. The coefficients a_i and b_i of continued fraction (14) are obtained by the well known recursion formulae[21]. We have adopted here the procedure given in Ref. 21. After obtaining the coefficients of the asymptotic series, the coefficients of the continued fractions have been obtained. The whole procedure was obtained on HCL-1800 computer. Here the Nth approximant of the continued fraction corresponds to $2N$ terms of the asymptotic series.

We calculate the first Regge trajectory for various Yukawa potentials

$$V(r) = G\exp(-r)/r \qquad \ldots(15)$$

for different small negative values of G. For the second approximant of continued fraction (14), our calculated coefficients are as follows:

$$a_0 = C_1^1$$
$$b_1 = -\frac{C_2^1}{C_1^1}$$
$$a_1 = \frac{C_3^1 C_1^1 - (C_2^1)^2}{(C_1^1)^2}$$
$$b_2 = \frac{C_4^1 (C_1^1)^2 - 2C_1^1 C_2^1 C_3^1 + (C_2^1)^3}{C_1^1 (C_2^1)^2 - (C_1^1)^2 C_3^1} \qquad \ldots(16)$$

For the higher approximants, the coefficients are obtained on the computer. After calculating coefficients of the continued fraction, we can obtain any number of points on the trajectory simply by substituting the appropriate value of $K = ik$ in Eq. (14).

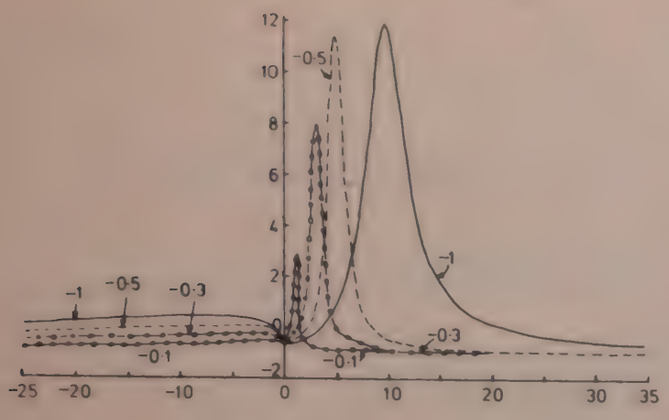

Fig. 1 —First Regge trajectory of the attractive Yukawa potential [Re α_1 as a function of k^2]

The first Regge trajectory of the Yukawa potential — This has been computed for four attractive potentials represented by Eq. (15) ranging from $G = -0.1$ to -1. It is shown in Figs 1 and 2. Fig. 1 gives Re α_1 as a function of k^2. From Fig. 1, it is seen that maxima of the trajectories for different potential strengths shift towards greater energy side as the strength of the potential increases. This observation is in agreement with the corresponding trajectories in the Schrödinger picture. Further, with the increase in the strength of the potential $V(r)$, the values of Re α_1 also increase for the same energy value k^2. It is also easy to infer that Regge trajectories cannot be extrapolated over large distances.

Fig. 2 shows the variation of Im α_1 as a function of Re α_1, i.e. the trajectory in the complex l-plane. We also find from Fig. 2 that the behaviour of these trajectories is in general agreement with the corresponding results already obtained by a perturbation procedure for the Klein-Gordon[22] and Dirac[23] particles. It is also seen that as $k^2 \to \pm \infty$, these trajectories tend to a finite limit. This observation is in conformity with the following well known result[11,20]:

$$\alpha_n(k) \to -n \text{ as } k^2 \to \pm \infty, \; n = 1, 2 \ldots \qquad \ldots(17)$$

Finally, it is found that one can obtain convergence for the complete range of the trajectory.

3 Conclusion

In this paper, we have obtained continued fractions for the Regge trajectories for weak Yukawa potential in the Klein-Gordon framework. The basis of the procedure adopted by us is that we first obtain an asymptotic series, and then sum it by a continued fraction. This technique, besides being applicable in field theory where a power series is known for a function satisfying a dispersion relation, can also be fruitfully employed in different current problems, viz. particle spectroscopy and anharmonic oscillator problems.

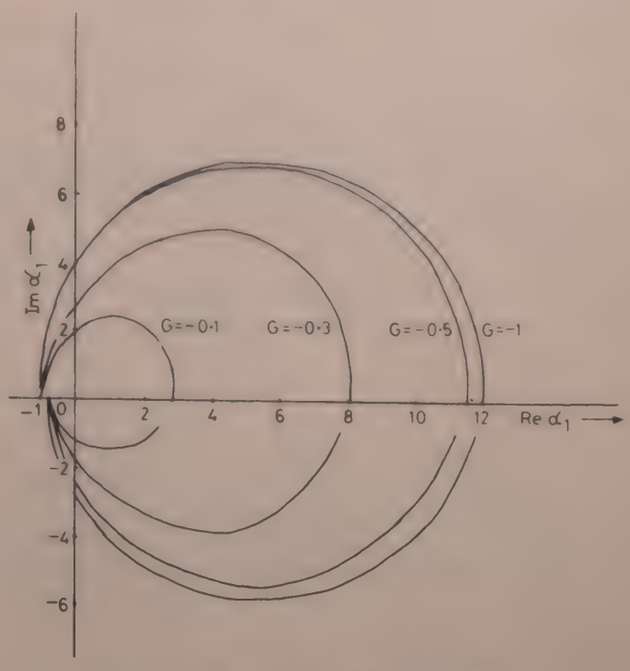

Fig. 2 —First Regge trajectory of the attractive Yukawa potential [Trajectory in the complex l-plane]

Acknowledgement

The authors are grateful to Dr D K Bhargava for his help in computer calculations. One of the authors (AB) thanks the University Grants Commission, New Delhi, for the award of a junior research fellowship.

References

1 Ahmadzadeh A, Burke P G & Tate C, *Phys Rev* (*USA*), **131** (1963) 1315.
2 Bethe H A & Kinoshita T, *Phys Rev* (*USA*), **128** (1962) 1418.
3 Flamm D, *Nuovo Cimento* (*Italy*), **29** (1963) 1080.
4 Warburton A E A, *Nuovo Cimento* (*Italy*), **32** (1964) 122.
5 Masson D, *Nuovo Cimento* (*Italy*), **35** (1965) 125.
6 Frautschi S C, Kaus P & Zachariasen F, *Phys Rev. B* (*USA*), **133** (1964) 1607.
7 Regge T, *Nuovo Cimento* (*Italy*), **14** (1959) 951.
8 Regge T, *Nuovo Cimento* (*Italy*), **18** (1960) 947.
9 Bottino A, Longoni A M & Regge T, *Nuovo Cimento* (*Italy*), **23** (1962) 954.
10 Lovelace C, *Nuovo Cimento* (*Italy*), **25** (1962) 730.
11 Lovelace C & Masson D, *Nuovo Cimento* (*Italy*), **26** (1962) 472.
12 Dyson F J, *Phys Rev* (*USA*), **92** (1953) 1331.
13 Symanzik K, *J Math Phys* (*USA*), **1** (1960) 249.
14 Weinberg S, *Phys Rev.* (*USA*), **124** (1961) 2049.
15 Swalen J D & Pierce L, *J Math Phys* (*USA*), **2** (1961) 736.
16 Singh V, Biswas S N & Datta K, *Phys Rev. D* (*USA*), **18** (1978) 1901.
17 Singh V, Rampal A, Biswas S N & Datta K, *Lett Math Phys* (*USA*), **4** (1980) 131.
18 Sharma L K, Choubey J & Muller-Kirsten H J W, *J Math Phys* (*USA*), **21** (1980) 1533.
19 Sharma L K & Iyer V P, *J Math Phys* (*USA*), **23** (1982) 1185.
20 Mandelstam S, *Ann Phys* (*USA*), **19** (1962) 254.
21 Wall H S, *Analytic theory of continued fractions* (Van Nostrand, Princeton, USA) 1948, Ch. XI.
22 Müller H J W, *Z Phys* (*Germany*), **186** (1965) 79.
23 Müller H J W, *Z Phys* (*Germany*), **183** (1965) 402.

Indian Journal of Pure & Applied Physics
Vol. 21, January 1983, pp 36-38

Theory of Open Circuit Voltage Decay in a *p-n* Junction Device

V K TEWARY*
Birla Institute of Technology and Science, Pilani 333031
and
S C JAIN
Solid State Physics Laboratory, Lucknow Road, Delhi 110007

Received 22 *October* 1981

It is shown that an old but hitherto unused expression due to North accounts for coupling between the diffused layer (emitter) and the base of a *p-n* junction device and explains the non-linear decay of the open circuit voltage as observed in n^+p (or p^+n) solar cells (or diodes) with heavily doped diffused layers. This non-linearity can be used to estimate minority carrier lifetime and band narrowing in the diffused layer caused by its heavy doping.

1 Introduction

There has been a renewed interest in the open circuit voltage decay (OCVD) method of measuring lifetime of the minority carriers in *p-n* junction devices—solar cells or diodes[1-7]. Lindholm and Sah[1] and Lindholm *et al.*[3] have shown that coupling between the diffused layer (emitter) and the base (referred to as *p-n* coupling) makes an important contribution to OCVD and that the OCVD data can be used to estimate minority carrier lifetime and band narrowing in the diffused layer of *p-n* junction devices. In their theoretical analysis they have used a single-lump charge control model which predicts a linear behaviour of OCVD. This is in disagreement with the recent experimental results[4,6-8] which state that in general OCVD is non-linear except at large values of time.

In this paper, we present a more rigorous theory of OCVD which accounts for the *p-n* coupling and explains its non-linear behaviour at small values of times. We show that the minority carrier lifetime and the band narrowing in the emitter caused by its heavy doping can be estimated by analyzing the non-linear part of OCVD and not its linear part which, in disagreement with Lindholm and Sah[1], would only give the lifetime in the base.

2 Theory

We assume that the thicknesses of the emitter and of the base are much larger than those of the corresponding diffusion lengths L_E and L_B. The decay of minority carrier concentration and hence of the open circuit voltage on abruptly terminating the steady-state forward-current in an n^+p device is described by the following differential equations for the emitter and the base respectively.

$$D_E\frac{\partial^2 q_E}{\partial x^2}-\frac{q_E}{\tau_E}=\frac{\partial q_E}{\partial t} \qquad \ldots(1)$$

$$D_B\frac{\partial^2 q_B}{\partial x^2}-\frac{q_B}{\tau_B}=\frac{\partial q_B}{\partial t} \qquad \ldots(2)$$

In Eqs (1) and (2), $q_E(t, x)$ and $q_B(t, x)$ are the excess minority carrier concentrations, D_E and D_B are their diffusion coefficients and τ_E and τ_B are their lifetimes in the emitter and the base respectively. The corresponding initial distributions are

$$\frac{q_E(0, x)}{Q_E}=e^{x/L_E}, \quad \text{for} \quad x\le 0 \qquad \ldots(3)$$

$$\frac{q_B(0, x)}{Q_B}=e^{-x/L_B}, \quad \text{for} \quad x\ge 0 \qquad \ldots(4)$$

where x is measured from the junction and, Q_E and Q_B are the values of q_E and q_B at the junction in the steady state at $t=0$. The thickness of the depletion layer is taken to be negligible. Assuming that the Boltzmann law is valid (see for example Ref. 9) in the time-dependent case also, we write the boundary conditions in the form

$$\frac{q'_E(t)}{q'_B(t)}=\frac{Q_E}{Q_B}, \text{ at } x=0, \text{ for all } t \qquad \ldots(5)$$

where

$$q'_{E,B}(t)=q_{E,B}(t, 0)$$

$$D_E\frac{\partial q_E}{\partial x}-D_B\frac{\partial q_B}{\partial x}=0 \text{ at } x=0, \text{ for all } t \qquad \ldots(6)$$

Eqs (5) and (6) account for the *p-n* coupling in the present theory since they couple the functions q_E and q_B and their derivatives at the junction.

Using the Laplace transform method, we obtain the following result,

$$\frac{q'_E(z)}{Q_E}=\frac{q'_B(z)}{Q_B}=\frac{1}{b-a}[b\,f(a, z)-a\,f(b, \tau z)] \qquad \ldots(7)$$

where

$$f(a, z)=e^{-z}[s(z)-as(a^2z)] \qquad \ldots(8)$$

$$s(z) = e^z \operatorname{erfc} \sqrt{z} \qquad \ldots(9)$$

$$b^2 = \frac{j^2(\tau - 1)}{j^2\tau - 1}, \quad a^2 = \frac{\tau - 1}{j^2\tau - 1} \qquad \ldots(10)$$

$$\tau = \tau_B/\tau_E,\ j = J_B/J_E = L_b Q_{BO}/L_E Q_{EO}\tau,$$

$$z = t/\tau_B \qquad \ldots(11)$$

J_B and J_E are saturation currents and Q_{BO} and Q_{EO} are the thermal minority carrier concentrations in the base and the emitter respectively.

Eq. (7) can be shown to be identical to North's expression for OCVD quoted by Lederhandler and Giacoletto[10]. North's expression has existed for more than 25 years but has never been used. This is presumably because the derivation of this equation and the conditions (5) and (6) under which it holds were not reported. Moreover, the importance of emitter contribution arising due to band-narrowing effects has been recognized only in recent years[1-3]. The function $s(z)$ in Eq. (7) is well known[11] and the form of Eq. (7) is convenient for numerical computations and for treating cases of practical interest. The reduced voltage $V_1(z) = \dfrac{eV(z)}{kT}$ is given by[9]

$$V_1(z) - V_1(0) = \ln \frac{q'_E(z)}{Q_E} = \ln \frac{q'_B(z)}{Q_B} \qquad \ldots(12)$$

Eq. (12) is valid as long as $e^{V_1(z)} \gg 1$ and the effect of the carriers stored in the space charge layer can be neglected. It may be noted that Eq. (7) becomes indeterminate when $a = b$. The limit as $a \to b$ exists and can be easily obtained[10].

3 Results and Discussion

To calculate $V_1(z)$ as a function of reduced time z from Eq. (7), we need only two parameters τ and j, or the parameters a and b [see Eq. (10)]. $[V_1(z) - V_1(0)]$ calculated for some cases of practical interest are shown in Fig. 1 and are discussed below:

I. If the diffusion term in Eq. (1) is ignored and if the effect of decay of carriers in the emitter is neglected, the decay of voltage (curve 1 in Fig. 1) due to recombination of the carriers in the base is given by the linear relation

$$V_1(z) - V_1(0) = -z \qquad \ldots(13)$$

II. If the injection efficiency of the emitter is close to unity, i.e. $j_B \gg j_E$ and if $\tau_B \gg \tau_E$, Eq. (7) reduces to

$$V_1(z) - V_1(0) = -z + \ln s(z) \qquad \ldots(14)$$

except for $t < \tau_E$. Eq. (14) is identical with the expression used by several earlier workers[9], neglecting the contribution of the emitter. The plot of Eq. (14) is shown by curve 2 in Fig. 1. Since the decay of voltage in Si diodes is affected by the charges stored in the space charge layer[2-4] when $V_1(z)$ is smaller than about 15 and also to avoid high injection effects, $V_1(0)$ cannot be chosen larger than about 20, with the result that the range $[V_1(z) - V_1(0) \sim 5]$ in which Eq. (7) can be used is rather small. The diffusion effects dominate in this range, the plot is curved (see curve 2 for small z) and a linear decay law cannot be used[9].

III. The band-narrowing and strong drift-field effects in the emitter of some modern diodes can substantially decrease j (Ref. 2-4). However, if $j^2\tau_B \gg \tau_E$ is still valid but $a \simeq 1/j$ is not negligibly small, Eq. (7) becomes

$$V_1(z) - V_1(0) = \ln \frac{f(a, z)}{1 - a} = -z + \ln \frac{s(z) - as(a^2 z)}{1 - a} \qquad \ldots(15)$$

Curves 3 and 4 show plots of Eq. (15) for $a = 0.5$ and $a = 10$ respectively. These curves show that for small values of z, the curvature, already present in curve 2, increases rapidly as the value of $a \simeq 1/j$ increases.

When $a = 10$, the initial drop $[V_1(z) - V_1(0) = 1.5]$ is practically vertical in curve 4 and can be confused with the well known drop[10] due to the series resistance. In such cases, series resistance should be measured independently and its contribution to the initial decay should be calculated and subtracted from the initial drop to determine the true shape of the curve for small values of time. A fit of the experimental plot with the theory in this range will yield a value of a. The values of J_B and J_E, neglecting the band narrowing, can be calculated from the known dopings of the base and the emitter of the diode, provided τ_B and τ_E are also known.

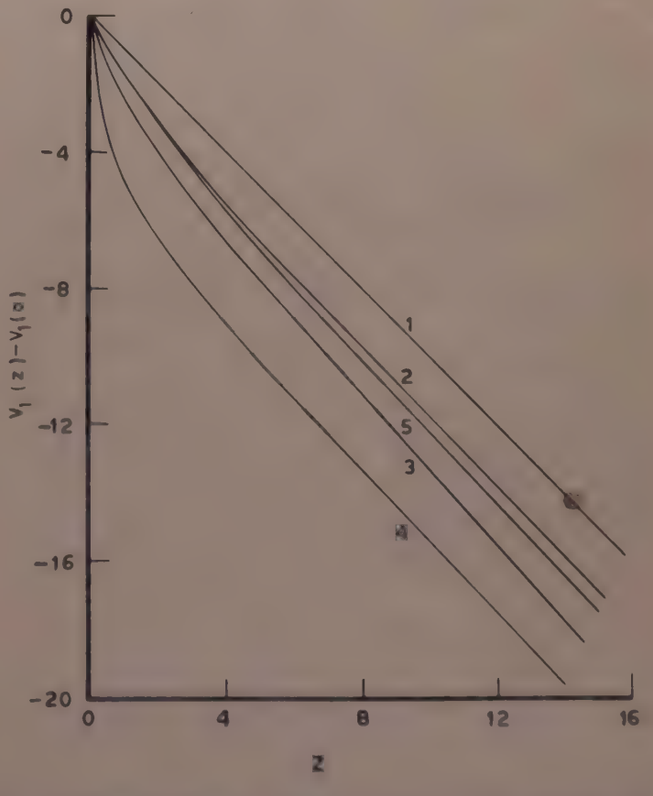

Fig. 1—Reduced voltage $V_1(z)$ as a function of the reduced time z [Curve 1, Eq. (13); curve 2, Eq. (14); curves 3 and 4, Eq. (15) for $a = 0.5$ and $a = 10$ respectively; and curve 5, Eq. (7) for $a = 0.1$ and $b = 0.7$]

The current J_E in the presence of the band narrowing ΔE_g increases as $J_E = J_{E0}\exp(\Delta E_g/kT)$ (Ref. 3) and hence we obtain

$$a = (J_{E0}/J_B)\exp(\Delta E_g/kT) \quad \ldots(16)$$

where J_{E0} is the value of J_E in the absence of band narrowing, i.e. for $\Delta E_g = 0$.

Using experimental values of a and known values of J_B and J_{E0}, ΔE_g can be calculated from the observed OCVD plot for small values of time. If τ_E is negligibly small as compared to τ_B, τ_E must be estimated by an independent method. If $\tau_B/\tau_E > 1$ but τ_E is not negligibly small, τ_B, τ_E and ΔE_g can all be determined from single OCVD plot as discussed in the next paragraph.

IV. We have also calculated the voltage decay plot (curve 5) for $\tau = 1.96$ and $j = 7.0$ (these values correspond to $a = 0.10$ and $b = 0.7$) using the complete Eq. (7). For large values of z, the plot is again roughly a straight line with a slope not very different from unity. Even in this case, when τ_E and τ_B are comparable, the slope of the plot for large values of z is roughly equal to unity. This means that $V(t)$ versus t plots can always be used, for large t, to determine τ_B. A computer fit of Eq. (7) with the experimental plot, for small t, will yield values of τ_E, a and b. The values of a and b can be used to calculate τ and the band narrowing. The value of τ can be compared with τ_B/τ_E determined independently, as discussed above, for self consistency.

Our results differ sharply from those of the earlier workers[1-3] in that we do not obtain a linear decay of $V_1(z)$ for small values of z. According to the earlier workers[1-3], the effect of the emitter is to make the voltage decay more rapid throughout the decay process. According to our results, the effect of the emitter on the decay rate is very large in the beginning but decreases progressively as t increases. Numerical calculations show that this effect and the associated curvature for small z-values do not disappear even if the thickness of the emitter is smaller than L_E (Ref. 7). In any case, since the results of Ref. 11 should apply to the diodes considered here, this cannot be the cause of the discrepancy. This discrepancy can, in fact, be attributed to the nature of approximations made in Ref. 1, viz. the use of the quasi-static approximation and the single-lump model which have very limited validity, particularly because the total charge on either side of the junction (and not the charge density at the junction) is related to the Boltzmann factor in these approximations.

The curvature in the OCVD plot predicted by the analysis in this paper is confirmed by experimental results reported in earlier papers (see for example Ref. 8). The curvature has also been observed recently in silicon diodes[4-6]. Neugroschel *et al.*[4] have attributed the curvature to the effect of carriers stored in the space charge layer. However, this curvature is also observed in germanium diodes[7-9] where the effect of carriers stored in the space charge layer is negligible.

In some cases, the observed $V(t)$ versus t plots are indeed linear[2,3,7] even for small t-values. We feel that the physical processes occurring in such diodes are not presently understood. We hope to publish later a more detailed account of these processes.

Acknowledgement

This work was partly supported by a research grant (at BITS, Pilani) from the Indian National Science Academy, New Delhi.

References

1 Lindholm F A & Sah C T, *J Appl Phys (USA)*, **47** (1976) 4203.
2 Neugroschel A, Lindholm F A & Sah C T, *IEEE Trans Electron Devices (USA)*, **24** (1977) 662.
3 Lindholm F A, Neugroschel A, Sah C T, *et al.*, *IEEE Trans Electron Devices (USA)*, **24** (1977) 402.
4 Neugroschel A, Chen P J, Pao S C & Lindholm F A, *IEEE Trans Electron Devices (USA)*, **25** (1978) 485.
5 Derdouri M, Letureq Ph. & Yague A M, *IEEE Trans Electron Devices (USA)*, **27** (1980) 2097.
6 Mahan J E, Ekstedt T W, Frank R I & Kaplow R, *IEEE Trans Electron Devices (USA)*, **26** (1979) 733.
7 Jain S C, Aggarwal S K & Muralidharan R, Private Communication (1981).
8 Gossick B R, *J Appl Phys (USA)*, **26** (1955) 1356.
9 Nosov Y R, *Switching in semiconductor diodes* (Plenum Press, New York), 1969.
10 Lederhandler S R & Giacoletto L J, *Proc IRE (USA)*, **43** (1955) 477.
11 *Handbook of mathematical functions*, edited by M Abramowitz and I A Stegun (Dover Publications, New York) 1965.

Indian Journal of Pure & Applied Physics
Vol. 21, January 1983, pp 39-43

Scatter Plate Interferometer for Aspherical Surfaces

M V R K MURTY & R P SHUKLA*
Spectroscopy Division, Bhabha Atomic Research Centre, Bombay 400085

Received 26 *April* 1982; *revised received* 21 *August* 1982

A theoretical method to compute shape of the fringes obtained in the scatter plate interferometer for an aspherical surface is presented. A method for making a scatter plate is described. Using this method, several scatter plates are made and used in the testing of a paraboloidal surface.

1 Introduction

The phenomenon of scattering as a means of beam splitting was described by several workers[1-11] for testing of the optical systems. The testing of a concave spherical surface by means of a scatter plate interferometer was described by many workers[2-6]. The scatter fringes are a contour map of the difference between the test surface and the ideal spherical surface. Hence these fringes directly provide the information about the imperfection of the mirror. The centre of the mirror itself serves as an ideal reference mirror and a separate comparison mirror is not required as in the Twyman-Green interferometer. The scatter fringe interferometer was used for testing of a $f/4$ paraboloid by Scottt[7]. Several photographs of the fringe patterns for the paraboloid were also published by Scott[7]. Recently, Rubin and Wyant[9] and Rubin[11] also published the scatter fringe interferograms for a paraboloid. Theoretical shape of the fringes for the aspherical surfaces was not studied by these workers[7,9,11]. The purpose of the present paper is to derive an expression for computing the fringe pattern of a true aspherical surface in the scatter fringe interferometer. Then the deformation of the test surface from the true aspherical surface can be obtained by finding out the difference between the computed fringe pattern and the experimental fringe pattern obtained in the scatter fringe interferometer.

2 Formation of Fringes in the Scatter Plate Interferometer

Fig. 1 illustrates a schematic diagram for finding out the optical path difference (OPD) between the aspherical surface and the spherical surface of radius of curvature equal to the vertex radius of aspherical surface. The equation of the conic surface in (X, Y, Z) coordinate system is given by

$$S^2 - 2rZ + pZ^2 = 0 \qquad \ldots(1)$$

where r is the vertex radius of the surface, Z-axis the axis of revolution, S the distance of the point $P(X, Y)$ from the origin $O(0, 0)$, i.e. $S^2 = X^2 + Y^2$ and p the conic constant. The surface is a conic surface of revolution according to the following conditions:

Hyperboloid $p < 0$
Paraboloid $p = 0$
Ellipsoid rotated about its major axis $1 > p > 0$
Ellipsoid rotated about its minor axis $p > 1$
Sphere $p = 1$

The point $C(r, 0)$ is the vertex centre of curvature of the surface. The dotted curve shows a reference sphere of radius r. If Δ be the distance between the point P on the aspherical surface and point P′ on the spherical surface, then the distance CP is given by the following relation:

$$(CP)^2 = (Z - r)^2 + S^2 = (r + \Delta)^2 \qquad \ldots(2)$$

From Eqs (1) and (2) we have:

$$\Delta^2 + 2r\Delta - \frac{(p-1)}{p}(S^2 - 2rZ) = 0 \qquad \ldots(3)$$

The deviation Δ can be written in the following polynomials in S up to order 12 from Eq. (3).

$$\Delta = -\frac{(p-1)}{8r^3}S^4 - \frac{p(p-1)S^6}{16r^5} - \frac{(5p^2+p-1)(p-1)S^8}{128r^7}$$

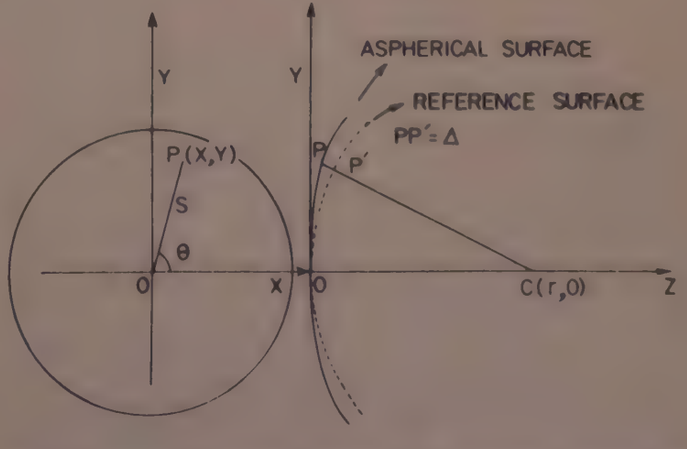

Fig. 1—Schematic diagram showing the difference between the aspherical surface and reference sphere

$$-\frac{[7p^2+2(p-1)]p(p-1)S^{10}}{256r^9}$$

$$-\frac{[7p^2(3p^2+p-1)+(p-1)^2](p-1)}{1024r^{11}}S^{12} \quad \ldots(4)$$

The scatter plate is normally placed near the centre of curvature for testing the optical surface. The OPD between the aspherical wavefront and the spherical wavefront is double the difference between the aspherical and reference sphere. Hence the equation for the OPD is given by:

$$\text{OPD} = 2\Delta + \frac{2(\bar{X})}{r}X + 2\left(\frac{\bar{Y}}{r}\right)\cdot Y + \frac{\bar{Z}(X^2+Y^2)}{r^2} \quad \ldots(5)$$

where $\bar{X}$ is the lateral displacement of the scatter plate in the X-direction from the paraxial focus; $\bar{Y}$ is the lateral displacement of the scatter plate in the Y-direction from the paraxial focus; and $\bar{Z}$ is the longitudinal defocussing of the scatter plate in the Z-direction from the paraxial focus. $\bar{Z}$ is taken to be positive for inside focus.

For constructive interference, Eq. (5) is written as

$$\text{OPD} = -\frac{(p-1)S^4}{4r^3} - \frac{p(p-1)S^6}{8r^5}$$

$$-\frac{(5p^2+p-1)(p-1)}{64r^7}S^8$$

$$-\frac{[7p^2+2(p-1)]p(p-1)}{128r^9}S^{10} - \ldots$$

$$+2\left(\frac{\bar{X}}{r}\right)X + 2\left(\frac{\bar{Y}}{r}\right)Y + \left(\frac{\bar{Z}}{r^2}\right)S^2$$

$$= N\lambda \quad \ldots(6)$$

where $N = 0, \pm 1, \pm 2, \pm 3, \ldots$ (order of interference); and λ = wavelength of light.

Thus the fringe pattern can be computed from Eq. (6) for aspherical mirror of known conic constant and radius for various focal settings of the scatter plate. We have simplified the above equation for the paraboloidal surface of large R-number (R number = radius/diameter). Using the polar coordinates $X = S\cos\theta$, $Y = \sin\theta$ and representing $\bar{X}/r = \alpha$, $\bar{Y}/r = \beta$ as tilt angles, Eq. (6) can be written, for the particular case of parabola, as

$$\frac{S^4}{4r^3} + \left(\frac{\bar{Z}}{r^2}\right)S^2 + 2S\alpha\cos\theta + 2S\beta\sin\theta = N\lambda \quad \ldots(7)$$

Using Eq. (7), several fringe patterns were computed for various modes of focussing. We have chosen the

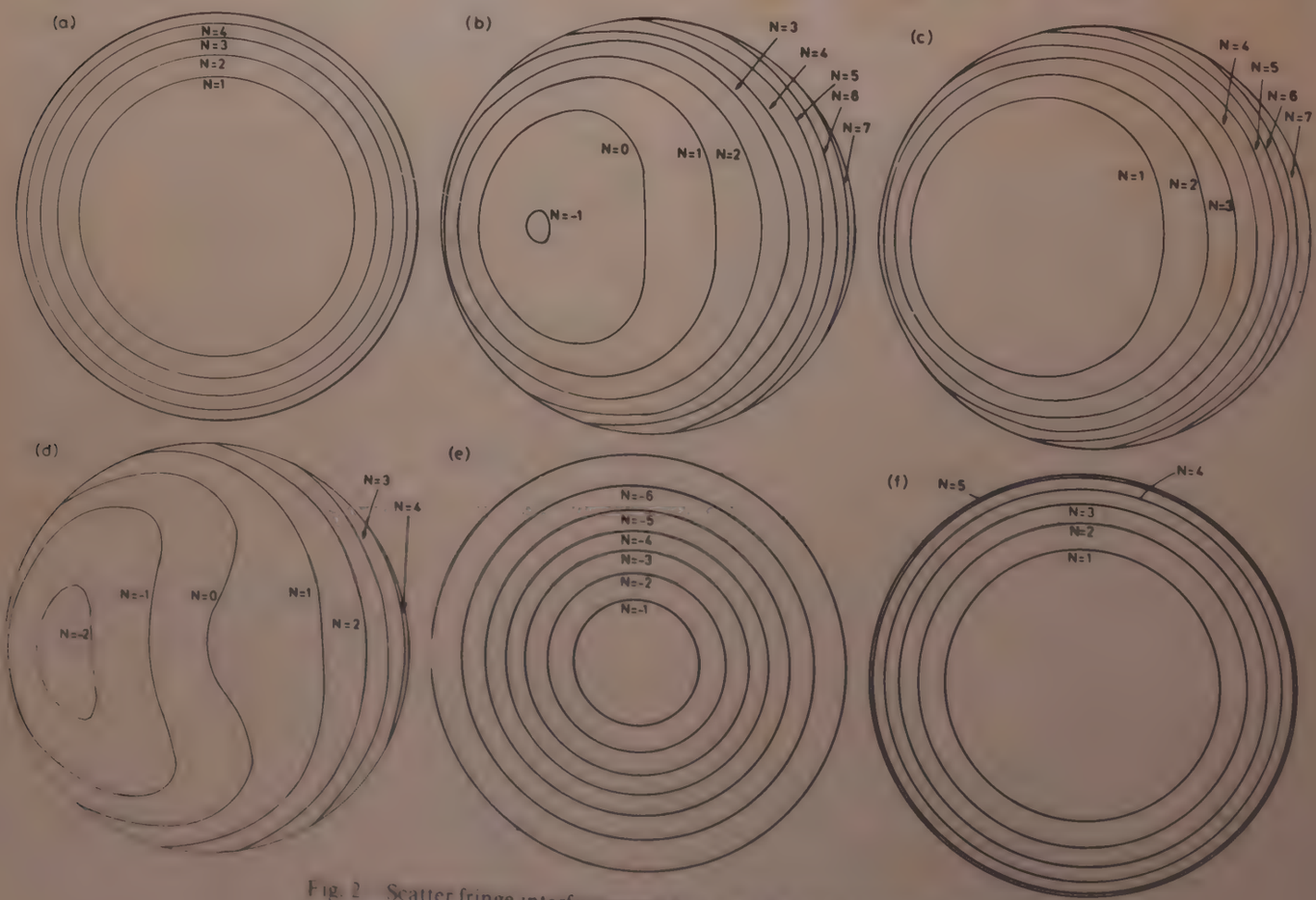

Fig. 2 — Scatter fringe interferograms for a paraboloidal surface of r = 2000 mm and dia = 200 mm for different values of $\bar{Z}$, α and β (a) $\bar{Z}$ = 0, α = 0, β = 0; (b) $\bar{Z}$ = 0, α = 0.0000084 radian and β = 0; (c) $\bar{Z}$ = 0.1 mm, α = 0.0000084 radian and β = 0; (d) $\bar{Z}$ = −0.38 mm, α = 0.0000084 radian and β = 0; (e) $\bar{Z}$ = −3.0 mm, α = 0 and β = 0; and (f) $\bar{Z}$ = 0.1 mm, α = 0 and β = 0.

following parameters for the computation of the fringe pattern. Diameter of the paraboloidal mirror = 20 mm, $r = 2000$ mm and $\lambda = 6328$ Å.

Fig. 2(a) shows the computed interferogram for no longitudinal defocussing ($\bar{Z} = 0$) and $\alpha = \beta = 0$. The fringes are concentric circles of radii proportional to the 4th root of the integer numbers. Fig. 2(b) shows the computed interferogram for no longitudinal defocussing ($\bar{Z} = 0$), tilt angle $\alpha = 0.0000084$ radian and $\beta = 0$.

Fig. 2(c) shows the computed interferogram for $\bar{Z} = 0.1$ mm, $\alpha = 0.0000084$ radian and $\beta = 0$ and Fig. 2(d) shows the computed interferogram for $\bar{Z} = -0.38$ mm, $\alpha = 0.0000084$ radian and $\beta = 0$. Figs 2(e) and 2(f) show the interferograms for $\bar{Z} = -3.0$ mm, $\alpha = 0, \beta = 0$ and $\bar{Z} = 0.1$ mm, $\alpha = 0$ and $\beta = 0$ respectively.

3 Method of Making the Scatter Plate

The scatter plate is a weak diffuser which has inversion symmetry about a central point. The scatter plate is made by double exposing a laser speckle pattern on a photographic plate and rotating the plate through an angle of 180° between the exposures to obtain the inversion symmetry. The doubly exposed photographic plate is processed and bleached. This bleached plate acts as the scatter plate. Houston[8] described a kinematic mounting for a 180° rotation of the photographic plate. An alternative device for rotating the plate through an angle of 180° is presented here. In this device, two gratings of the same frequency are used. One of them is fixed while the other is rotated. When the grating lines are parallel, a uniform broad Moiré fringe is formed between the gratings. We can obtain two angular positions of the rotating grating in one rotation for which the uniform broad fringe is formed. These two angular positions are exactly 180° apart. If the two gratings differ slightly in the frequency, then equispaced fringes parallel to the ruling lines are formed.

The schematic diagram for making the scatter plate is shown in Fig. 3. The beam of light from a He-Ne laser is focussed at the focal point of a collimating lens by means of a microscope objective. A spatial filter is placed at the focus of the microscope objective. The ground glass and photographic plate are placed in the path of the beam with a separation of about 0.07 mm. With laser illumination such a small separation is not necessary. The photographic plate holder is fixed on one end of the shaft which is passing through a bearing block. The bearing block is fixed rigidly to the base. The plate holder is free to rotate about its axis inside the bearing block. A grating of frequency 100 l/mm is fixed at the other end of the shaft. A similar grating is also fixed at the end of the bearing block. For preparing the scatter plate, the shutter is closed and the photographic plate (Agfa 10-E-75) is loaded in a

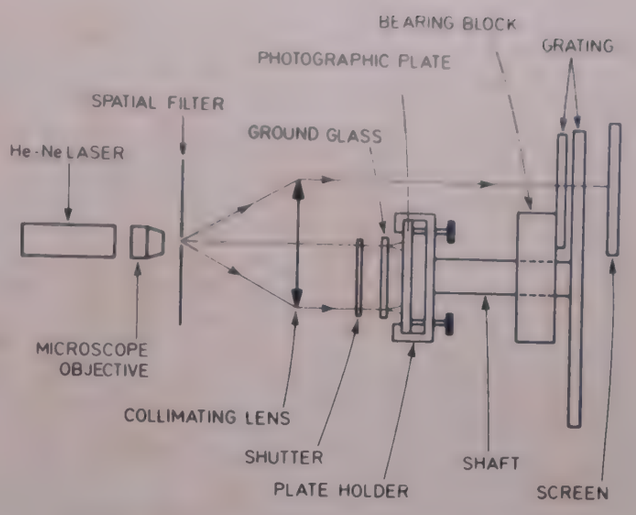

Fig. 3—Schematic diagram showing the experimental set-up for making the scatter plate

completely dark room. The photographic plate holder is rotated until a uniform broad Moiré fringe is seen on the ground glass screen placed in the light path. The shutter is opened to expose the photographic plate. After closing the shutter, the photographic plate is again rotated until a uniform broad fringe is seen on the screen. The shutter is opened for the second exposure of the plate. The doubly exposed photographic plate is developed in Kodak D-19 developer and fixed. The processed plate is bleached by the modified R-10 bleach[12]. Following the above procedure, several scatter plates were made by exposing the photographic plates to various exposures and the scatter plates were tested for the contrast of the fringes. We found that the scatter plates, exposed to optical density in the range 0.35-0.5, gave the fringes of good contrast. The accuracy in the 180° rotation of the plate depends on the straightness of the grating lines and also on the judgement with which the uniform broad or equispaced Moire fringes parallel to the ruling lines can be set in the grating aperture. We used a glass plate ground with aluminium oxide of grade 304 (smoothing powder) as diffuser in order to get the laser speckle pattern.

4 Interferometer

Fig. 4 shows a schematic diagram of a scatter plate interferometer for the testing of a concave surface placed near the centre of curvature. The light from a point source is focussed on the test surface by means of a projection lens. The scatter plate is placed in the path of the beam. The scatter plate scatters part of the light and fills the aperture of the mirror. This scattered light is focussed back on the scatter plate itself by the mirror surface and passes through the plate undeviated. We call it a test beam. The direct unscattered light is reflected back on the scatter plate by a paraxial region of the mirror and it gets scattered after passing through

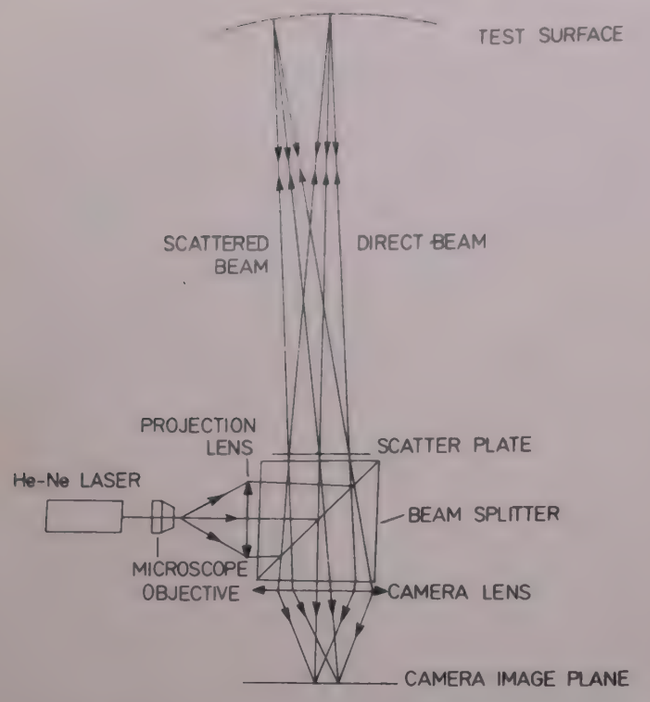

Fig. 4—Schematic diagram showing the scatter plate interferometer for testing of the mirror

the scatter plate. This forms a reference beam of light. The two beams are recombined to produce interference fringe pattern. The fringes are focussed on a screen by a camera lens. In addition to the fringes, a bright spot of light is focussed on the screen which destroys the information about the centre of the mirror and the scattered light reduces the contrast of the fringes to some extent. The interferometer is very sensitive to vibrations and the intensity of the fringes is also low and therefore He-Ne laser is used in order to reduce the exposure time during the photography of the fringes.

We have used a mirror of dia. 95 mm and $r = 1000$ mm for taking the photographs of the fringes in the scatter plate interferometer. The mirror is found to be very close to the parabola. Fig. 5 shows some typical interferograms of the above mentioned mirror taken in various modes of defocussing and tilt angles. The shapes of the fringe contours resemble those of the fringe contours of Fig. 2, even though the fringe patterns of Fig. 2 were plotted for a different radius of curvature and aperture.

5 Procedure for Finding the Deviation of the Aspherical Surface

The deviations of mirror surface are measured along the normal to the surface. The fringe positions are measured along the diameter of the interferogram for a series of values of N. If we denote x_N as the position of the Nth fringe, we obtain (x_1, N_1), (x_2, N_2), $(x_3, N_3) \ldots (x_N, N)$ by measuring the fringe positions. All these values can be fitted by a least-squares

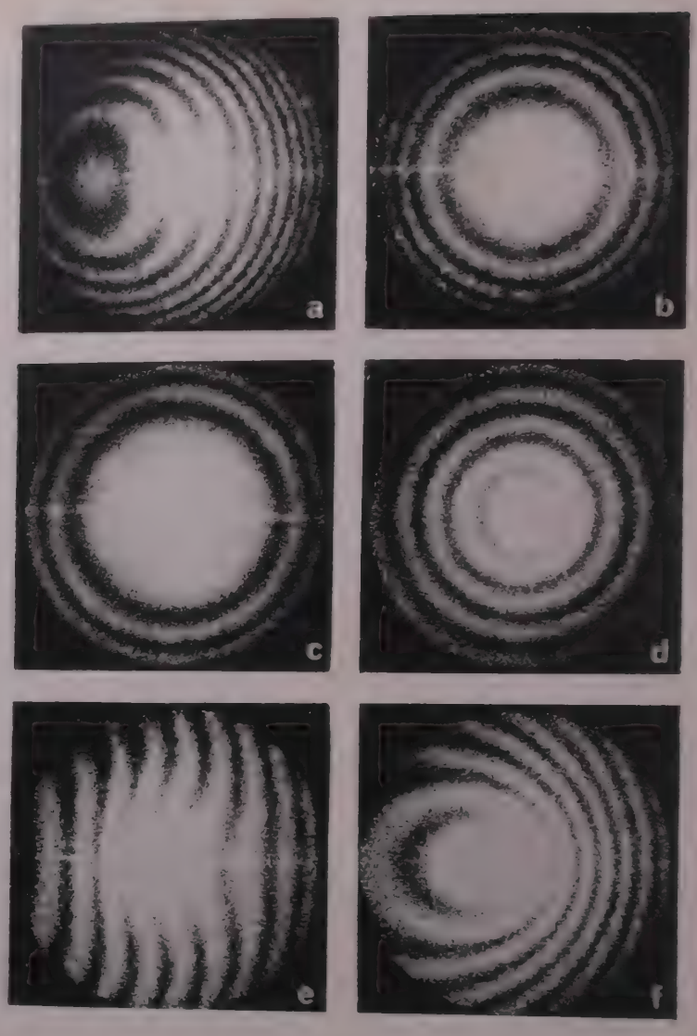

Fig. 5—Scatter fringe interferograms for a paraboloidal surface of r = 1000 mm and dia = 95 mm [(a) defocussing with tilt (inside focus); (b) defocussing without tilt (inside focus); (c) no longitudinal defocussing; (d) defocussing (outside focus); (e) defocussing with slight tilt (outside focus); and (f) defocussing with tilt (outside focus)]

procedure[13] to the polynomial of the following equation [Eq. (8)], and the coefficient A'_n (where $n = 1, 2, 3, 4$) can be found:

$$A'_1 X^4 + A'_2 X^6 + A'_3 X^8 + A'_4 X^{10} + D X^2 + EX = N\lambda \quad \ldots(8)$$

The exact aspheric coefficients are computed by the following relations:

$$A_1 = \frac{(p-1)}{4r^3}, \quad A_2 = \frac{p(p-1)}{8r^5},$$

$$A_3 = (p-1)(5p^2 + p - 1)/64r^7 \text{ and}$$

$$A_4 = \frac{[7p^2 + 2(p-1)]p(p-1)}{128r^9} \quad \ldots(9)$$

and

$$\delta A_n = A_n - A'_n \quad \ldots(10)$$

Thus the difference in the coefficients (δA_n) can be obtained. The deviation (ε) of the test surface from the true aspheric is then calculated from the following equation:

$$\varepsilon = \frac{(\delta A_1)S^4}{2} + \frac{(\delta A_2)S^6}{2} + \frac{(\delta A_3)S^8}{2} + \frac{(\delta A_4)S^{10}}{2} \quad \ldots(11)$$

We have analyzed the interferogram shown in Fig. 5 and found that the deviation of the surface from a parabola is $\lambda/4$.

References

1 Burch J M, *Nature (GB)*, **171** (1953) 889.

2 Burch J M, *J Opt Soc Am (USA)*, **52** (1962) 600(A).

3 Dyson J, Appendix B: *Interferometers* in *Concepts of classical optics* by J B Strong (Freeman, Sanfrancisco, California) 1958, 377.

4 Martin L C, *Technical optics* (Pitman, London) Vol. 2, 1960, 327.

5 Scott R M, *Appl Opt (USA)*, **1** (1960) 396.

6 Shoemaker A H & Murty M V R K, *Appl Opt (USA)*, **5** (1966) 603.

7 Scott R M, *Appl Opt (USA)*, **8** (1969) 531.

8 Houston J B(Jr), *Opt Spectra (USA)*, **4** (1970) 32.

9 Rubin L F & Wyant J C, *J Opt Soc Am (USA)*, **69** (1979) 1305.

10 Rubin L F, *Appl Opt (USA)*, **19** (1980) 1634.

11 Rubin L F, *Opt Eng (USA)*, **19** (1980) 815.

12 Hariharan P & Ramanathan C S, *Appl Opt (USA)*, **10** (1971) 2197.

13 Malacara Hernandez D, *Testing of optical surfaces*, Ph D thesis, The University of Rochester, 1965, 95.

NOTES

Indian Journal of Pure & Applied Physics
Vol. 21, January 1983, pp 44-46

Normal Coordinate Analysis & Thermodynamic Functions of Chloromethyl Formate

R PRASAD*
Department of Chemistry, University of Indore, Indore

Received 23 *June* 1982; *revised received* 18 *October* 1982

The normal coordinate treatment of all the 18 vibrations of chloromethyl formate ($HCOOCH_2Cl$) has been carried out using Urey-Bradley type of force field for in-plane vibrations and simple valence force field for out-of-plane vibrations. The calculated frequencies have been compared with the values reported by Dahlqvist [*Spectrochim Acta Vol. A (GB)*, **36** (1980) 37]. The nature of all the 12 in-plane and 6 out-of-plane vibrations has been discussed in terms of potential energy distribution among symmetry coordinates. Thermodynamic functions for the molecule have also been computed.

The vibrational spectra of chloromethyl formate have been reported by Dahlqvist[1] and the various possible conformations of this molecule have been discussed in detail. It has been concluded that in non-polar CCl_4 solution only the *Z* conformation (chloromethyl group *cis* to carbonyl oxygen) is stable, while a small amount of *E* conformation (chloromethyl group *trans* to carbonyl oxygen atom) coexists in polar CH_3CN solution owing to rotation about C—O bond and that rotation of the chloromethyl group is not free and can oscillate between the *Z*, ap (chlorine atom *trans* to carbonyl oxygen atom) and *Z*, ±SC (chlorine atom *cis* to carbonyl oxygen) conformations. On the basis of comparison with similar molecules[2,3] it has been concluded that *Z*, ap is the most stable conformation. Theoretical CNDO/2 MO calculations have also been carried out for this molecule[1].

In the present study the normal coordinate analysis of the more stable *Z*, ap conformation of chloromethyl formate has been carried out with the main objective of confirming the previously reported assignments of the vibrational spectra and discussing the mixing of vibrations in terms of potential energy distribution among different symmetry coordinates. Thermodynamic functions of the molecule are also reported.

Normal coordinate analysis—The calculations of normal frequencies, according to Wilson's *FG*-matrix method[4], were made on a TDC-316 computer using a programme similar to that of Schachtschneider[5]. The molecule was considered to have a planar carbon-oxygen skeleton with chloromethyl group *cis* to carbonyl oxygen (Fig. 1). Based on C_s symmetry the vibrations were classified into $12A'$ (in-plane) and $6A''$ (out-of-plane) modes. The structural parameters were taken from the microwave work of Curl[6] for methyl formate with a C—Cl bond distance of 1.76 Å and an HCCl bond angle of 113°54′. The symmetry coordinates used for representing different vibrations are given in Table 1.

A Urey-Bradley type intramolecular force field was employed for in-plane vibrations and simple valence force field (SVFF) was used for out-of-plane vibrations. The initial set of force constants were transferred from ethyl formate[7], formic acid[8] and related molecules[8,9]. The final set of force constants which gave the best agreement between observed and calculated frequencies is given in Table 2. The calculated and observed frequencies and the potential energy distribution (PED) among different symmetry coordinates are given in Table 3. As is evident from Table 3, many of the calculated frequencies show a close agreement with the experimentally observed values reported by Dahlqvist[1]. The PED shown in Table 3 leads to some important results. The PED of CH_2 stretching modes among the symmetry coordinates S_5 and S_{13} is almost 100%. Similarly, contribution of C—H stretch to S_2 is, almost 100%. CH_2 bending modes, namely CH_2 scissoring, CH_2 wagging, CH_2 twist and CH_2 rock are also quite independent. Likewise, CH bending modes, namely CH bend and CH out-of-plane bend modes are also quite independent. Two torsional modes, i.e. CO-torsion and O—CH_2Cl torsion, are also quite independent with nominal mixing among themselves. On the other hand, in the case of remaining normal modes the PED is among several symmetry coordinates with high percentage which shows that the frequencies in chloromethyl formate molecule are mixed. It was noted during calculations that CH_2

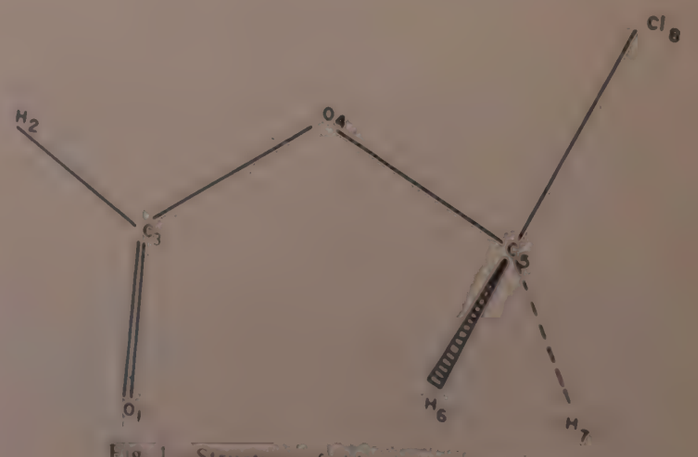

Fig. 1—Structure of chloromethyl formate

Table 1—Symmetry Coordinates for Chloromethyl Formate

Symmetry coordinate	Vibrational mode
A′ vibrations	
$S_1 = \Delta R_{13}$	ν C=O
$S_2 = \Delta R_{23}$	ν C—H
$S_3 = \Delta R_{34}$	ν C—O—C
$S_4 = \Delta R_{45}$	ν C—O– C
$S_5 = \frac{1}{\sqrt{2}}(\Delta R_{56} + \Delta R_{57})$	ν_s CH_2
$S_6 = \Delta R_{58}$	ν C—Cl
$S_7 = \frac{1}{\sqrt{6}}(2\Delta\theta_{134} - \Delta\theta_{132} - \Delta\theta_{234})$	δ O=C—O
$S_8 = \frac{1}{\sqrt{2}}(\Delta\theta_{234} - \Delta\theta_{132})$	δ C—H
$S_9 = \Delta\theta_{345}$	δ C—O—C
$S_{10} = \Delta\theta_{657}$	δ CH_2
$S_{11} = \frac{1}{2}(\Delta\theta_{654} - \Delta\theta_{658} - \Delta\theta_{758} + \Delta\theta_{754})$	ω CH_2
$S_{12} = \Delta\theta_{458}$	δ O—C—Cl
A″ vibrations	
$S_{13} = \frac{1}{\sqrt{2}}(\Delta R_{56} - \Delta R_{57})$	ν_{as} CH_2
$S_{14} = \frac{1}{2}(\Delta\theta_{654} - \Delta\theta_{658} + \Delta\theta_{758} - \Delta\theta_{754})$	τ CH_2
$S_{15} = \frac{1}{2}(\Delta\theta_{654} + \Delta\theta_{658} - \Delta\theta_{758} - \Delta\theta_{754})$	ρ CH_2
$S_{16} = \Delta\gamma_{1432}$	γ CH
$S_{17} = \Delta\tau_{2345}$	τ CO
$S_{18} = \Delta\tau_{3458}$	τ O—CH_2Cl

Table 2—Force Constants (in mdyne/Å) of Chloromethyl Formate

A′ (UBFF)

$K_{13} = 10.70$	$H_{134} = 0.71$	$F_{14} = 1.10$
$K_{23} = 4.20$	$H_{132} = 0.25$	$F_{12} = 0.50$
$K_{34} = 3.00$	$H_{234} = 0.38$	$F_{24} = 0.35$
$K_{45} = 3.00$	$H_{345} = 1.50$	$F_{35} = 0.15$
$K_{56} = 4.80$	$H_{657} = 0.50$	$F_{67} = 0.05$
$K_{57} = 4.80$	$H_{654} = 0.39$	$F_{64} = 0.18$
$K_{58} = 2.60$	$H_{658} = 0.25$	$F_{68} = 0.10$
	$H_{758} = 0.25$	$F_{78} = 0.10$
	$H_{754} = 0.39$	$F_{74} = 0.18$
	$H_{458} = 0.43$	$F_{48} = 1.50$

A″ (SVFF)

$K_{56} = 4.98$	$H_{654} = 0.49$	$H\gamma = 1.42$
$K_{57} = 4.98$	$H_{658} = 0.38$	$H\tau CO = 0.050$
	$H_{758} = 0.38$	$H\tau O—CH_2Cl = 0.030$
	$H_{754} = 0.49$	

Table 3—Observed and Calculated Frequencies and PED for Chloromethyl Formate

Observed frequencies cm^{-1}	Calculated frequencies cm^{-1}	Description*, PED(%)
		A′ vibrations
2990	2982.7	ν_s CH_2(100)
2952	2943	ν CH(100)
1785	1786	ν C=O(77) + δCH(15)
1450	1449	δ CH_2(75) + δC—O—C(5) + ωCH_2(5)
1370	1376	δ CH(83) + ν C=O(11)
1340	1338	ω CH_2(81) + δCH_2(9)
1127	1147	ν_{as} C—O—C(28) + δO=C—O(27) + δC—O—C(26) + ν_sC—O—C(8)
1003	1017	ν_s C—O—C(63) + δC—O—C(10) + δO—C—Cl(15)
758	792	ν_{as} C—O—C(64) + ν C—Cl(27) + δO=C—O(10)
743	709	ν C—Cl(64) + δO=C—O(27) + δO—C—Cl(11)
423	424	δ O—C—Cl(58) + ν_sC—O—C(17)
323	273	δ C—O—C(46) + δO=C—O(26) + δO—C—Cl(20) + νC—Cl(13)
		A″ vibrations
3061	3062	ν_{as} CH_2(100)
1263	1289	τ CH_2(98)
1049	1060	γ CH(88)
946	894	ρ CH_2(98)
228	246	τ CO(82) + τO—CH_2Cl(10) + γCH(8)
68	61	τ O—CH_2Cl(81) + τCO(8)

* ν = stretching, δ = bending, ω = wagging, ρ = rocking, γ = out-of-plane bending, τ = torsion, *s* = symmetric, *as* = asymmetric

Table 4—Thermodynamic Functions (in cal K^{-1} mol^{-1}) of Chloromethyl Formate

Temperature K	$\frac{H^0 - H_0^0}{T}$	$\frac{-(G^0 - H_0^0)}{T}$	S^0	C_p^0
100	9.49	49.98	59.47	11.26
200	11.22	57.90	68.31	14.61
273.15	12.47	60.77	73.24	17.22
298.15	12.91	61.89	74.80	18.16
300	12.94	61.97	74.91	18.23
400	14.73	65.94	80.67	21.90
500	16.49	69.41	85.90	25.12
600	18.16	72.57	90.73	27.78
700	19.69	75.48	95.17	29.97
800	21.09	78.21	99.30	31.77
900	22.37	80.77	103.14	33.28
1000	23.53	83.18	106.76	34.55
1100	24.58	85.48	110.06	35.63
1200	25.54	87.66	113.10	36.54
1300	24.42	89.74	116.16	37.32
1400	27.22	91.72	118.94	37.99
1500	27.96	93.63	121.59	38.57

bending modes were too much dependent on the choice of symmetry coordinates. The symmetry coordinates used by Charles *et al.*[7] to describe such modes for *trans* ethyl formate gave totally absurd results for this molecule. It may be mentioned here that these symmetry coordinates could not produce reasonable results for even *trans* ethyl formate as is evident from the discussion by these authors themselves[7]. For example, their calculations showed that CH_2 wagging modes be assigned to 810 cm^{-1} etc.

The frequencies at 423 cm^{-1} and 323 cm^{-1} have been assigned to δ C—O—C and δ O—C—Cl modes respectively by Dahlqvist[1], but according to the present calculations δ C—O—C mode is having higher contribution in 323 cm^{-1} and δ O—C—Cl mode is having higher contribution in 423 cm^{-1}. It may be mentioned here that δ C—O—C mode in similar molecules like ethyl formate[7] and ethyl chloroformate[7], has been assigned at 325 cm^{-1} and 292 cm^{-1} respectively. In view of the above, the present assignment of δ C—O—C mode at 323 cm^{-1} and that of δ O—C—Cl mode at 423 cm^{-1} seems to be more reasonable. Similarly, calculated frequencies at 1017 cm^{-1} and at 894 cm^{-1} are closer to 1003 cm^{-1} and 946 cm^{-1} respectively. On the basis of PED, these are assigned to C—O—C stretch and CH_2 rock respectively. However, these frequencies are assigned by Dahlqvist[1] to CH_2 rocking and ν C—O—C respectively.

Thermodynamic functions—Thermodynamic functions of chloromethyl formate have been calculated by utilizing standard expressions given by Herzberg[10] and Colthup[11]. Vibrational frequencies have been taken from the work of Dahlqvist[1]. The barrier to rotation along O—CH_2Cl bond as well as about C(0)—O has been computed from a CNDO/2 MO method[1] and found to be quite large. Therefore, the corresponding vibrations are treated as ordinary vibrations for the purpose of calculating vibrational contribution to thermodynamic functions. The symmetry number for overall rotation as well as for internal rotation has been taken to be unity. The principal moments of inertia are calculated as 45.46, 49.08, and 4.15 in units of 10^{-39}g-cm^2. The calculations of total contributions of $(H^0 - H_0^0)/T$; $-(G^0 - H_0^0)/T$, S^0 and C_p^0 at various temperatures (100-1500 K) were made in the rigid rotor harmonic oscillator approximation and these relate to 1 mol of perfect gas at 1 atm pressure, and are presented in Table 4.

References

1 Dahlqvist M G, *Spectrochim Acta A (GB)*, **36** (1980) 37.

2 Laato H, *Ann Univ Turku Ser A1 (Finland)*, (1965) 82, 86.

3 Charles S W, Jones G I L, Owen N L & West L A I, *J Mol Struct (Netherlands)*, **32** (1976) 111.

4 Wilson E B(Jr), *J Chem Phys (USA)*, **7** (1939) 1047; **9** (1941) 76.

5 Schachtschneider J H, *Tech Rep: Vibrational analysis of polyatomic molecules* (Shell Development Co., California), 1964.

6 Curl R F(Jr), *J Chem Phys (USA)*, **30** (1959) 1529.

7 Charles S W, Jones G I L, Owen N L, *et al.*, *J Mol Struct (Netherlands)*, **16** (1973) 225.

8 Nakamoto K & Kishida S, *J Chem Phys (USA)*, **41** (1964) 1554.

9 Zerbi G & Gussoni M, *J Chem Phys (USA)*, **41** (1964) 456.

10 Herzberg G, *Molecular spectra and molecular structure: Infrared and Raman spectra of polyatomic molecules* (Van Nostrand, New York).

11 Colthup N B, Daly L H & Wiberley S E, *Introduction to infrared & Raman spectroscopy* (Academic Press, New York), 1964.

Indian Journal of Pure & Applied Physics
Vol. 21, January 1983, pp 47-48

Effect of Temperature on Dielectric Relaxation Time in Lutidines at Microwave Frequency

OM VIR SINGH*
Department of Physics, University of Jammu, Jammu Tawi 180001

Received 20 *March* 1982; *revised received* 28 *July* 1982

The dielectric constant and dielectric loss in 2,4-, 2,6- and 3,5-lutidines in carbon tetrachloride solution have been measured at 4 different temperatures (T) using various concentrations. The relaxation time (τ) and dipole moment (μ) have been evaluated using Gopala Krishna's method. The expected behaviour of the decrease of τ with the rise in T can be attributed to the decrease in viscosity of the solvent with the rise in temperature. It is most probable that an inductive effect is significant in 2,6-lutidine because of close proximity of two methyl groups to nitrogen atom and it may be the reason for the higher τ value for this compound compared to the other two.

Dielectric relaxation studies give useful information regarding molecular structure, the intermolecular and intramolecular forces in liquids. No systematic dielectric relaxation studies in lutidines (di-methyl pyridine) are available in literature. This note presents the results of measurements of relaxation time of 3 lutidines, viz. 2,4-, 2,6-, and 3,5-lutidines in carbon tetrachloride solution at 4 different temperatures in continuation of our earlier reports[1,2].

The dielectric constant (ε') and dielectric loss (ε'') in these lutidines were determined using their dilute solutions in CCl_4. The measurements were made on X-band microwave bench at a frequency of 9.8 GHz using waveguide transmission technique. VSWR (voltage to standing wave ratio) measurements at various concentrations and temperatures gave dielectric wavelength which was used to calculate ε' and ε'' by using the method of Heston *et al.*[3] The expected error in the measurement of ε' and ε'' was $\pm 1\%$ and $\pm 4\%$ respectively. Different temperatures were obtained with the help of a GDR-made thermostat U-10. The relaxation time (τ) and dipole moment (μ) were calculated by Gopala Krishna's method[4].

The viscosity (η) of CCl_4 at different temperatures was measured with the help of Ostwald viscometer with an accuracy of $\pm 2\%$. For this purpose the viscometer was kept in a temperature bath maintained at desired temperatures.

The values of τ and μ of the studied lutidines are presented in Table 1. The experimental error in the τ values was about $\pm 10\%$.

In the present investigation, the viscosity is varied by varying the temperature but the solvent, viz. CCl_4 remains the same, thus keeping the interaction of the solute and solvent molecules same. It is evident from Table 1 that the value of τ decreases with rise in T for all the 3 compounds. This behaviour seems to be reasonable because the viscosity of the solvent decreases with increase of temperature. It appears that viscosity plays an important role in changing the relaxation time of the polar solute. However, it is observed that the ratio τ/η does not remain constant as required by Debye's relation. This shows the departure of the molecular behaviour from that predicted by Debye's equation. The plot of $\log(\tau T)$ versus $\log\eta$ gives a straight line for all the compounds studied as shown in Fig. 1. This shows that the molecular

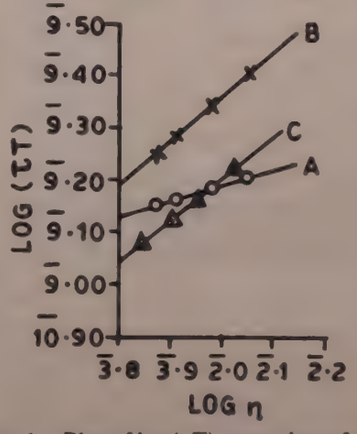

Fig. 1—Plot of $\log(\tau T)$ versus $\log\eta$ for the lutidines studied [A, —O— 2,4-; B, — × — 2,6-, and C, —Δ— 3, 5-lutidine]

Table 1—Relaxation Time (τ) and Dipole Moment (μ) of 2,4-, 2,6- and 3,5-Lutidines in Carbon Tetrachloride Solution at Different Temperatures (T)

T, °C	η, cP	$\tau \times 10^{12}$, sec	μ, D
	2,4-Lutidine		
10	1.13	5.63	2.48
20	0.96	5.12	2.42
30	0.83	4.87	2.54
40	0.74	4.49	2.52
	2,6-Lutidine		
10	1.13	8.81	1.80
20	0.96	7.50	1.78
30	0.83	6.11	2.00
40	0.74	5.65	1.95
	3,5-Lutidine		
15	1.04	5.80	2.56
25	0.90	4.90	2.63
35	0.79	4.31	2.63
45	0.69	3.75	2.68

behaviour of lutidines is consistent with the theory and formula predicted by Krishnaji and Man Singh[5], viz.

$$\tau = (B/T)\eta^x$$

or $\log(\tau T) = \log B + x \log \eta$

where B is a constant of the system and x is a parameter less than 1.

The values of μ so evaluated agree well with those obtained by Higasi's method[6] within experimental error. The μ values evaluated experimentally by Higasi's method at low frequency are 2.55, 1.89 and 2.69 D for 2,4-, 2,6- and 3,5-lutidines respectively.

The comparison of the τ values of lutidines (Table 1) reveals that the rate of change of τ with T is different for the 3 compounds. In other words, for the same change of 10°C in T, τ does not change by the same amount for all the 3 lutidines. The change in τ is most in 2,6-lutidine and least in 2,4-lutidine. These results indicate that the structure of these molecules plays an important role in determining the rate of change of relaxation time with temperature. This is most probably due to the fact that the relaxation mechanism is very much influenced by the relative positions of two methyl groups with respect to the nitrogen atom, in addition to viscosity. In 2,6-lutidine, the two methyl groups are attached in 2,6 positions with respect to the nitrogen atom. Evidently the two methyl groups are relatively closer to the nitrogen atom in this compound as compared to those in the other two compounds. This structure may induce greater intramolecular polarization (essentially orientational polarization) as a result of the pronounced inductive effect of the methyl groups coupled with higher electronegativity of the nitrogen atom. Consequently, 2,6-lutidine takes longer time to revert to the normal state after the removal of applied field, i.e. for relaxation which accounts to higher values of τ in this compound than in the other two compounds. Further investigations are being made in this direction on pure lutidines to evaluate various thermodynamic parameters so that the classification of lutidines may be ascertained.

The author is highly thankful to Prof G P Srivastava and Dr K N Tripathi, Department of Physics and Astrophysics, University of Delhi, and Prof Y Prakash, Head of the Department of Physics, University of Jammu for their guidance and supervision.

References

1 Singh O V, Srivastava G P & Tripathi K N, *Indian J Pure & Appl Phys*, **20** (1982) 66.
2 Singh O V, *Indian J Pure & Appl Phys*, **19** (1981) 1222.
3 Heston W M (Jr), Franklin A D, Hennelly E J & Smyth C P, *J Am Chem Soc (USA)*, **72** (1950) 3443.
4 Gopala Krishna K V, *Trans Faraday Soc (GB)*, **53** (1957) 767.
5 Krishnaji & Man Singh A, *Indian J Pure & Appl Phys*, **2** (1964) 176.
6 Higasi K, *Bull Inst Phys Chem Res Tokyo (Japan)*, **22** (1943) 85.

Indian Journal of Pure & Applied Physics
Vol. 21, January 1983, pp 49-51

Studies on the Metal-Ligand Equatorial & Axial Bond Strengths in Some Copper(II) Complexes of 1-3-Diaminopropane by ESR Technique

G PONTICELLI
Istituto Chimica Generale Inorganica & Analitica, University of Cagliari, via Ospedale 72, 09100 Cagliari, Italy
and
M M AHMED, B A SASTRY*,
S Md ASADULLAH & P SATYANARAYANA
Molecular & Solid State Laboratory, Physics Department, Osmania University, Hyderabad 500007

Received 20 *May* 1982; *revised received* 22 *September* 1982

The *X*-band ESR spectra due to $Cu(tn)_2Cl_2$, $Cu(tn)_2Br_2$, $Cu(tn)_2(NO_3)_2$ and $[Cu(tn)_2NCS]BPh_4$ (tn = 1,3-diaminopropane) in polycrystalline samples and in solutions of N,N′-dimethylformamide have been studied at room and liquid nitrogen temperatures. It is found that two chemically inequivalent molecules are existing in the unit cell of $Cu(tn)_2Br_2$ and the *g* values of $Cu(tn)_2Cl_2$ and $Cu(tn)_2Br_2$ (species A) obtained in polycrystalline samples are close to molecular *g* values. From the estimations of in-plane and axial metal-ligand bond strengths, it is found that the σ-bond is weak when axial bonds are strong.

ESR technique can be employed to detect the nature of the coordinating atoms in copper(II) complexes since spin-Hamiltonian parameters obtained in solid or liquid-solutions of the complexes having different coordinating atoms will be different. The spin-Hamiltonian parameters obtained from the above technique can be used to estimate the metal-ligand bond nature and the influence of the anions on the equatorial bond strengths. In the present studies, a series of copper(II) complexes of 1,3-diaminopropane(tn), viz. (1) $Cu(tn)_2Cl_2$, (2) $Cu(tn)_2(Br_2)$, (3) $Cu(tn)_2(NO_3)_2$, (4) $[Cu(tn)_2NCS]BPh_4$ are studied by ESR technique in polycrystalline and N,N′-dimethylformamide (DMF) solution forms, to get the information mentioned above. Among the complexes under study, only $[Cu(tn)_2NCS]BPh_4$ is studied by IR, optical absorption and molar conductivity techniques[1] and it is found that the chromophore is a square-based pyramid formed with nitrogens. The other three complexes are not studied by any experimental technique.

The above complexes are prepared by using the general procedure described by Ponticelli[2] and Devoto and Ponticelli[1]. The composition of these is confirmed by chemical analysis. The ESR spectra of these complexes both in polycrystalline and solution (10^{-3}M) forms are recorded with a Varian E-4 *X*-band spectrometer. The maximum errors in *g* values and hyperfine line separation are respectively ± 0.001 and ± 2 G. A Unicam SP700 spectrophotometer is used to record optical absorption spectra in solutions.

Fig. 1 shows the EPR spectra of $Cu(tn)_2Cl_2$, $Cu(tn)_2Br_2$ and $Cu(tn)_2(NO_3)_2$ in polycrystalline form. The spectra of $Cu(tn)_2Cl_2$ and $Cu(tn)_2(NO_3)_2$ are indicating axial symmetry. On the other hand, the spectrum of $Cu(tn)_2Br_2$ is indicating two chemically inequivalent species (A, B) with axial symmetry. The ESR spectrum of $[Cu(tn)_2NCS]BPh_4$ is found to be a single asymmetric line and is not shown in Fig. 1. The *g* values of the above anisotropic spectra are calculated using Kneubühl procedure[3] and are given in Table 1. The values of

$$G = (g_3 - 2)/[(g_1 + g_2 - 2)/2]$$

are also calculated from the *g* (g_1, g_2 and g_3) values and are included in Table 1. It is found that when this *G*

Table 1—*G* and *g* Values Obtained in Polycrystalline Samples

Substance	g_1	g_2	g_3	*G*
$Cu(tn)_2Cl_2$	2.040	2.040	2.200	5.00
$Cu(tn)_2Br_2$				
Species A	2.048	2.048	2.216	4.5
Species B	2.048	2.048	2.106	2.2
$Cu(tn)_2(NO_3)_2$	2.066	2.066	2.175	2.65
$Cu(tn)_2NCSBPh_4$	2.065	—	—	—

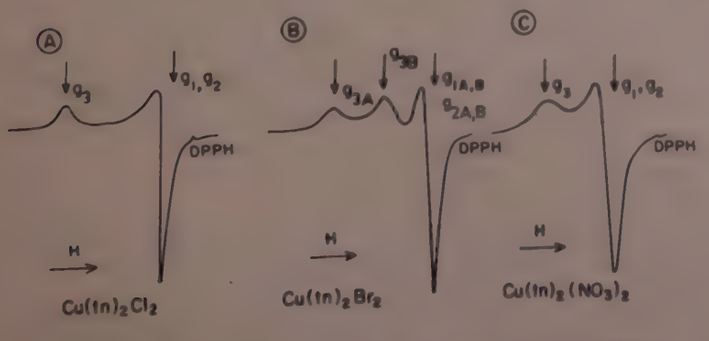

Fig. 1—ESR spectra in polycrystalline samples at 300 K

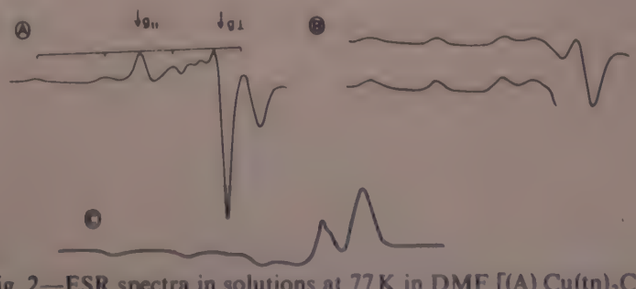

Fig. 2—ESR spectra in solutions at 77 K in DMF [(A) $Cu(tn)_2Cl_2$; (B) $Cu(tn)_2Br_2$; and (C) $Cu(tn)_2(NO_3)_2$]

Table 2—Spin-Hamiltonian Constants of Copper(II) Complexes in DMF Solutions

Substance	g	A MHz	$g_\parallel$	$g_\perp$	$A_\parallel$ MHz	$A_\perp$ MHz	ΔE^* cm^{-1}
**$Cu(tn)_2Cl_2$	2.1036	221.82	2.212	2.042	606.46	43.06	—
$Cu(tn)_2Br_2$	2.112	230.13	2.227	2.054	587.22	64.98	16670
$Cu(tn)_2(NO_3)_2$	2.1085	240.87	2.227	2.049	579.39	84.70	18150
$Cu(tn)_2NCSBPh_4$	2.110	239.56	2.223	2.053	570.41	86.22	—

*Only one optical absorption peak is obtained which is assigned to $B_{2g} \rightarrow B_{1g}$ transition.

**The g and A values correspond to the species indicated in Fig. 2.

value lies in between 5.0 and 3.5, the g values will be near to molecular g values and when they lie outside this range, the g values indicate strong exchange interaction among magnetically inequivalent copper(II) ions in the unit cell[4-7]. Since these G values in the case of $Cu(tn)_2Br_2$ (species B) and $Cu(tn)_2(NO_3)_2$ fall beyond this range, the g values indicate the existence of more than one magnetically inequivalent molecules with exchange interaction among copper(II) ions. Hence these g values represent the overall symmetry of these molecules in the unit cell[8]. The G values in the case of $Cu(tn)_2Cl_2$ and $Cu(tn)_2Br_2$ (species A) are 5.0 and 4.5 respectively (Table 1) and hence the unit cell contains either one or more than one magnetically equivalent molecules.

In all cases except in the case of $Cu(tn)_2Cl_2$, the ESR spectra in the DMF solutions indicated the existence of a single species, whereas in the case of $Cu(tn)_2Cl_2$, more than one species (Fig. 2) are detected in the frozen DMF solutions. It is only possible to get g and A values for one species where the parallel components are clearly visible (Fig. 2) The $g_\parallel$, $g_\perp$, $A_\parallel$ and $A_\perp$ values are obtained from the room and liquid nitrogen temperature spectra as described earlier[9], and are given in Table 2 along with optical absorption values. As can be seen from Tables 1 and 2, g values obtained in DMF solutions and polycrystalline samples of $Cu(tn)_2Cl_2$ and $Cu(tn)_2Br_2$ (species A) are found to be approximately equal indicating that the solvation of this complex in DMF solution is less.

The g and A values of these complexes are characteristic of nitrogen coordination in the principal plane and most probably the apical positions are occupied by the anions. Moreover, these values also indicate a $d_{x^2-y^2}$ ground state for the $3d^1$ hole in all cases. Following the standard procedure of Maki and McGarvey[10] and Kuska *et al.*[11], the σ-bond parameter (α^2), isotropic contact term (K) and fraction of $3d$-character (f^2) in the $3d$-$4s$ ground state are calculated and are given in Table 3. In all cases, the α^2 value obtained from isotropic data is less than the α^2 value obtained from anisotropic data[11]. Therefore, $4s$ mixing in the ground state is obvious. This $4s$ mixing in the ground state is a measure of axial bond strength since the bonding between apical ligands and copper ion occurs through the interaction between metal $4s$ and $4p$ orbitals and ligand orbital[12]. As can be seen from Table 3, the strength of the σ-bond is decreasing in the following order:

$$[Cu(tn)_2NCS]BPh_4 > Cu(tn)_2(NO_3)_2 > Cu(tn)_2Br_2 > Cu(tn)_2Cl_2$$

The $4s$-contribution $(1-f^2)$ in the ground state is varying in the opposite order:

$$[Cu(tn)_2NCS]BPh_4 < Cu(tn)_2(NO_3)_2 < Cu(tn)_2Br_2 < Cu(tn)_2Cl_2$$

This can be explained in the following way. The amount of $4s$ character in the ground state is a measure of the axial field strength[11] and it is found that the equatorial ligands will be driven away from the metal ion due to the action of the axial field[13]. Therefore, as the axial field strength or the $4s$ contribution in the ground state increases, the equatorial bond strengths will be proportionally weakened. Following the procedure of Maki and McGarvey[10], the in-plane π-bond parameters (β_1^2) are calculated using the spin-Hamiltonian constants and optical absorption values given in Table 2. As can be seen from β_1^2 values (Table 3), the in-plane π bond strength is found to increase in an order opposite to that of σ bond strength.

Table 3—Bond Parameters Obtained in Copper(II) Complexes

Substance	α^2	f^2	β_1^2	Isotropic term (K) MHz
$Cu(tn)_2Cl_2$	0.793	0.978	—	−353.72
$Cu(tn)_2Br_2$	0.766	0.987	0.765	−377.07
$Cu(tn)_2(NO_3)_2$	0.741	0.996	0.855	−383.5
$Cu(tn)_2NCSBPh_4$	0.723	0.999	—	−382.6

References

1 Devoto G & Ponticelli G, *J Inorg Nucl Chem (GB)*, 37 (1975) 1153.
2 Ponticelli G, *Inorg Chim Acta (Italy)*, 5 (1971) 461.
3 Kneubwhl F K, *J Chem Phys (USA)*, 33 (1960) 1074.
4 Procter I M, Hathaway B J & Nichols P, *J Chem Soc A (GB)*, (1968) 1678.

5 Tomlinson A A G & Hathaway B J, *J Chem Soc A*, (1968) 1685.
6 Beu M J, Hathaway B J & Fereday R J, *J Chem Soc A (GB)*, (1972) 1229.
7 Tomlinson A A G & Hathaway B J, *J Chem Soc A (GB)*, (1968) 1905.
8 Sastry B A & Sastry G S, *Physica (Netherlands)*, **54** (1971) 20.
9 Sastry B A, Asadullah S Md, Ponticelli G & Massacessi M, *J Chem Phys (USA)*, **70** (1979) 2834.
10 Maki A H & McGarvey B R, *J Chem Phys (USA)*, **29** (1958) 31, 35.
11 Kuska H A, Rogers M R & Drullinger R E, *J Phys Chem (USA)*, **71** (1967) 109.
12 Sastry B A, Asadullah S Md, Ponticelli G & Massacessi M, *Spectro Chim Acta Part A (GB)*, **35** (1979) 817.
13 Barbucci R, Paoletti P & Campbell M J M, *Inorg Chim Acta (Italy)*, **10** (1974) 69.

Indian Journal of Pure & Applied Physics
Vol. 21, January 1983, pp 52-55

Calculation of the Total Stopping Power of Positrons in Various Absorbers—Proposed Empirical Equation

S K GUPTA, O P VARMA†,
D K GUPTA* & R K TYAGI**
Department of Physics, S V College, Aligarh

Received 5 *April* 1982; *revised received* 18 *June* 1982

An empirical equation has been proposed for evaluating the total stopping power of 0.2 to 10.0 MeV positrons in absorbers of atomic number from 1 to 92 and in some compounds including detector materials. The values of total stopping power obtained by using this equation have been found to agree with the theoretically calculated values within 3-4%. Method for calculating the stopping power of positrons theoretically has also been described.

Considerable volume of work exists on the penetration of low, medium and high energy electrons through several absorbers[1-10] and on the evaluation of parameters like stopping power[11,12], c.s.d.a. range difference[13] and range[14], projected range[15], straggling free range[16], maximum range[17] and extrapolated range[18] for electrons. However, the above studies for positrons have been subjected to very little investigation[12,19-23] due to some practical difficulties such as: (i) poor detection technique for positrons, (ii) non-availability of positron sources of suitable lifetime and energy, (iii) the difficulty of getting a collimated beam of positrons without any background radiation and (iv) non-availability of stopping power data because of the poor knowledge of appropriate correction factor like Elwert[24] and Koch-Motz correction[25]. The present work is an attempt in this direction.

In the previous papers[11,13,14] we have reported an empirical equation for the total stopping power of electrons in the energy region 0.2-10.0 MeV for the absorbers of atomic number 1 to 92 as well as for compounds including detector materials. The purpose of the present communication is to obtain a similar equation for positrons and to report a method for the calculation of total stopping power theoretically.

Calculation procedure for total stopping power—The stopping power of positrons, for absorbers and compounds mentioned above, in the energy region of our interest, has not been computed so far. This is, perhaps, because of the scarce experimental knowledge to determine correction factors like the Elwert factor[24] and Coulomb correction[25] etc. For comparison purposes, we have calculated the energy loss due to collisions using Rohrlich and Carlson's expressions[26] which are based on multiple scattering theory, according to which the average energy loss per unit path length of positrons in a medium of density ρ and atomic number Z, can be represented by the expression:

$$\left(-\frac{1}{\rho}\frac{dE}{dx}\right)_{\text{collision}} = \frac{2\pi e^4 N_0 Z}{A mc^2 \beta^2}\left[\ln\left(\frac{T^2}{I^2}\cdot\frac{\gamma+1}{2}\right)+f(\gamma)-\delta\right] \quad \ldots(1)$$

where

$$f(\gamma) = 2\ln 2 - \frac{1}{12}\beta^2\left[23+\frac{14}{(\gamma+1)}+\frac{10}{(\gamma+1)^2}+\frac{4}{(\gamma+1)^3}\right]$$

and $E(=\gamma mc^2)$ is the total incident energy, $T[=(\gamma-1)mc^2]$ is the kinetic energy of the moving positron, δ is the density effect correction while other constants have their usual meanings. We have used Sternheimer formula[27], based on theoretical prediction, for the calculation of density effect correction. The ratios of stopping powers of positrons and electrons in various media (for $Z > 10$) and at various energies have been obtained by interpolating the results of Cu, Ag and Au (Ref. 28). The bremsstrahlung losses were then computed using these ratios and the relevant collision losses of positrons. There may be a possibility of some error due to radiation losses in the values of stopping power of positrons obtained by this method. But in no case it should be significant since, in the energy region 0.2-10.0 MeV, radiation losses are not so prominent as compared to total energy losses.

Since the energy loss of 10 MeV electrons in hydrogen, carbon and neon due to radiation is respectively about 1.99%, 7.94% and 10.8% of the total energy loss and still smaller for low energies, we have computed the stopping power of positrons under the approximation that the radiation loss of positrons in the light materials is the same as that of electrons of initial kinetic energies below 10 MeV. At present there is no evidence (experimental or theoretical) against this approximation.

Empirical equation—In order to avoid the use of complicated expression[28] for total energy loss and to carry out realistic transport calculations (so that various physical quantities such as mean projected range and straggling contribution, etc. may be

† Physics Department, D N College, Hissar.
** Physics Section, Z H College of Engg. & Tech., A M U, Aligarh

Table 1—Numerical Values of Parameters Appearing in Eq. (2)

Z-values	$-S^+$ MeV cm^2/g	a^+	b^+
$2 \le Z \le 10$	0.0546 ± 0.0330		
$10 \le Z \le 30$	0.0242 ± 0.0074	-0.0040	1.8496
$30 \le Z \le 92$	0.0129 ± 0.0038		

Table 2—Comparison of the Theoretically and Empirically Calculated Values of Stopping Power in Metals*

K.E. (MeV)	Theoretical values (MeV-cm^2/g)	Calculated values (MeV-cm^2/g)	Difference (%)
	Carbon		
0.2	2.5397	2.5958	−2.21
0.3	2.1084	2.1113	−0.13
0.5	1.7849	1.7549	1.68
0.8	1.6354	1.5931	2.58
1.0	1.5995	1.5556	2.74
2.0	1.5826	1.5495	2.08
4.0	1.6529	1.6534	−0.03
6.0	1.7234	1.7464	−0.13
8.0	1.7856	1.8231	−2.09
10.0	1.8423	1.8879	−2.47
	Lead		
0.2	1.4935	1.5641	−4.72
0.3	1.2864	1.3035	−1.32
0.5	1.1519	1.1320	1.72
0.8	1.1225	1.0872	3.13
1.0	1.1325	1.0969	3.14
2.0	1.2586	1.2399	1.48
4.0	1.5060	1.5519	−3.05
6.0	1.7881	1.8204	−1.80
8.0	2.0694	2.0547	0.71
10.0	2.3504	2.2642	3.66
	Copper		
0.2	1.9272	2.0421	−5.96
0.3	1.6183	1.6734	−3.40
0.5	1.3959	1.4079	−0.98
0.8	1.3082	1.3022	0.45
1.0	1.2956	1.2844	0.86
2.0	1.3440	1.3302	1.03
4.0	1.4890	1.4906	−0.11
6.0	1.6413	1.6257	0.94
8.0	1.7896	1.7381	2.87
10.0	1.9344	1.8343	5.17
	Uranium		
0.2	1.4383	1.4885	−3.49
0.3	1.2435	1.2444	−0.07
0.5	1.1216	1.0869	3.09
0.8	1.1031	1.0514	4.68
1.0	1.1185	1.0652	3.84
2.0	1.2584	1.2237	2.75
4.0	1.5179	1.5633	−2.98
6.0	1.8153	1.8586	−2.38
8.0	2.1108	2.1191	−0.39
10.0	2.4110	2.3542	2.35

*The calculations have been done for entire range of elemental metals from $Z = 1$ to $Z = 92$.

Table 3—Comparison of Theoretical and Empirically Calculated Values of Stopping Power in Detector Materials*

K.E. (MeV)	Theoretical values (MeV-cm^2/g)	Calculated values (MeV-cm^2/g)	Difference (%)
	Anthracene		
0.2	2.7359	2.8058	−2.55
0.3	2.2706	2.2818	−0.49
0.5	1.9223	1.8958	1.38
0.8	1.7620	1.7202	2.37
1.0	1.7239	1.6792	2.59
2.0	1.7078	1.6708	2.16
4.0	1.7858	1.7805	0.29
6.0	1.8621	1.8791	−0.90
8.0	1.9287	1.9604	−1.64
10.0	1.9888	2.0290	−2.02
	Cadmium telluride		
0.2	1.6799	1.7951	6.98
0.3	1.4255	1.4810	3.89
0.5	1.2517	1.2630	0.90
0.8	1.1954	1.1851	0.85
1.0	1.1949	1.1796	1.27
2.0	1.2814	1.2655	1.23
4.0	1.4755	1.4826	0.48
6.0	1.6882	1.6650	−1.37
8.0	1.8988	1.8192	−4.19
10.0	2.1058	1.9534	−7.23
	Sodium iodide		
0.2	1.7027	1.8441	8.30
0.3	1.4451	1.5187	5.09
0.5	1.2659	1.2911	1.99
0.8	1.2041	1.2067	0.21
1.0	1.2037	1.1983	−0.44
2.0	1.2828	1.2741	−0.86
4.0	1.4624	1.4759	0.92
6.0	1.6566	1.6452	−0.68
8.0	1.8475	1.7875	−3.24
10.0	2.0360	1.9110	−6.13
	Teflon		
0.2	2.3537	2.4488	4.04
0.3	1.9657	1.9931	1.39
0.5	1.6755	1.6589	−0.98
0.8	1.5443	1.5086	−2.30
1.0	1.5144	1.4746	−2.62
2.0	1.5088	1.4746	−2.26
4.0	1.5848	1.5812	0.22
6.0	1.6612	1.6755	0.86
8.0	1.7306	1.7533	1.31
10.0	1.7954	1.8191	1.31

*Calculations were also done for gallium antimonide, gallium arsenide, indium arsenide, indium antimonide, indium phosphonite, aluminium antimonide, antimony selenide, cadmium telluride, zinc telluride, calcium iodide, calcium fluoride, lithium iodide, cesium iodide, *p*-terphenyl, *p*-quaterphenyl, naphthalene, glass and plastic.

Table 4—Comparison of the Theoretical and Empirically Calculated Values of Stopping Power in Compounds*

K.E. (MeV)	Theoretical values (MeV-cm^2 g)	Calculated values (MeV-cm^2 g)	Difference (%)
	Acetylene		
0.2	2.8076	2.8825	−2.66
0.3	2.3299	2.3439	−0.60
0.5	1.9724	1.9472	1.27
0.8	1.8082	1.7666	2.30
1.0	1.7693	1.7244	2.54
2.0	1.7536	1.7152	2.19
4.0	1.8344	1.8270	0.40
6.0	1.9128	1.9275	−0.76
8.0	1.9810	2.0105	−0.14
10.0	2.0423	2.0805	−0.18
	Silver bromide		
0.2	1.7814	1.9083	7.12
0.3	1.5083	1.5702	4.10
0.5	1.3179	1.3327	1.12
0.8	1.2528	1.2429	−0.78
1.0	1.2496	1.2328	−1.35
2.0	1.3306	1.3047	−1.94
4.0	1.5172	1.5024	−0.97
6.0	1.7143	1.6681	−2.69
8.0	1.9061	1.8073	−5.18
10.0	2.0937	1.9276	−7.93
	Stilbene		
0.2	2.7721	2.8446	−2.61
0.3	2.3006	2.3131	−0.54
0.5	1.9476	1.9218	1.32
0.8	1.7854	1.7436	2.33
1.0	1.7468	1.7020	2.56
2.0	1.7310	1.6933	2.18
4.0	1.8104	1.8040	0.35
6.0	1.8878	1.9036	−0.83
8.0	1.9551	1.9857	−1.56
10.0	2.0158	2.0551	−1.94
	Silicon dioxide		
0.2	2.3985	2.4185	0.83
0.3	1.9975	1.9428	−2.73
0.5	1.7016	1.6421	−3.49
0.8	1.5723	1.4963	−4.83
1.0	1.5453	1.4641	−5.25
2.0	1.5565	1.4704	−5.53
4.0	1.6565	1.5852	−4.30
6.0	1.7508	1.6534	−5.56
8.0	1.8353	1.7684	−3.64
10.0	1.9140	1.8385	−3.94

*Calculations have also been made for inorganic compounds including water, lithium carbonate, lithium fluoride, lithium oxide, beryllium oxide, boron carbide, boron oxide, sodium carbonate, sodium nitrate, sodium oxide, magnesium carbonate, magnesium fluoride, magnesium oxide, aluminium oxide, calcium carbonate, calcium sulphate, titanium dioxide, silver chloride and for organic compounds which include hexane, paraffin, polyethylene, toluene, polystyrene, bakelite, makrolon, plexiglass, mylar, polyvinyl acetate, ethylcellulose, cellulose acetate, cellophane, polyoxymethylene, araldite, rilson nylon, hostaflon, polyvinyl chloride, mica, and for some gaseous compounds, viz methane, ethane, propane, butane, ethylene, carbon dioxide and air.

estimated), an empirical equation for the total stopping power of positrons is given as:

$$\left(-\frac{1}{\rho}\frac{dE}{dx}\right)_{\text{total}} = (S^+ Z + 1.3230).\gamma^2/(\gamma^{a^+ Z \pm b^+} - 1.0) \quad \ldots(2)$$

where S^+, a^+ and b^+ are parameters and other constants have their usual meanings. The basis of the derivation of this equation has been discussed elsewhere[29].

The stopping power of positrons in compounds including detector materials has been estimated by replacing Z in Eq. (2) by Z_{eff} (Ref. 14) where $Z_{\text{eff}} = \sum_i f_i Z_i$, and f_i is the fraction by weight of the ith constituent element with atomic number Z_i.

Results and discussion—The computation work of the parameters a^+, b^+ and S^+ has been done with the help of IBM-1130 computer and computed values are tabulated in Table 1 for $Z = 2$ to $Z = 92$. For $Z = 1$ the value of $-S^+$ is 1.3855 and other parameters are the same as given in Table 1. Using these values of parameters in Eq. (2), we have calculated the stopping power of positrons in the energy region 0.2-10.0 MeV for the entire range of metals, for twenty-two detector materials and fifty compounds. Table 2 presents the comparison between the empirically calculated and theoretically obtained values of the stopping power for four metals, viz. carbon, copper, lead and uranium. Table 3 presents similar results for four detector materials, viz. anthracene, sodium iodide, cadmium telluride and teflon. In Table 4 we have compared the theoretically obtained stopping power with empirically calculated results for four compounds (gaseous, inorganic and organic), viz. acetylene, stilbene, silver bromide and silicon dioxide. It can be seen from these tables and other results that Eq. (2) very well reproduces c.s.d.a. stopping power data. A measure of the good validity of Eq. (2) is given by the reciprocal of percentage difference of the stopping power data as obtained from empirical equation and theoretical calculations. It is clear that the c.s.d.a. data for stopping power of positrons in various metals and compounds obtained from both approaches are in good agreement. However, the labour involved in the present approach is extremely reduced as compared to the numerical methods.

The authors are thankful to Dr S C Gupta and Shri N D Grover, Principals, for their encouragement throughout the course of this work. The authors are also grateful to the CSIR, New Delhi (for the award of a post doctoral fellowship to SKG) and to the UGC, New Delhi, for the financial assistance.

References

1 Zerby C D & Keller F L, *Nucl Sci Eng*, **27** (1967) 190.
2 Kanaya K & Okayama S, *J Phys D (GB)*, **5** (1972) 43.
3 Mukoyama T, *Nucl Instrum & Methods (Netherlands)*, **134** (1976) 125.
4 Rao B N S, *Nucl Instrum & Methods (Netherlands)*, **44** (1966) 155.
5 Harder D & Poschet G, *Phys Lett B (Netherlands)*, **24** (1967) 519.
6 Cosslett V E & Thomas R N, *Br J Appl Phys (GB)*, **16** (1965) 779.
7 Batra R K & Sehgal M L, *Nucl Instrum & Methods (Netherlands)*, **102** (1973) 565.
8 Spanel L E, Rupaal A S & Patrick J R, *Phys Rev B (USA)*, **8** (1972) 4072.
9 Tabat T, Ito R & Okabe S, *Nucl Instrum & Methods (Netherlands)*, **103** (1972) 85.
10 Berger M J & Seltzer S M, *Studies in penetration of charged particles through matter*, National Research Council (USA) Publication No. 1133, 1964.
11 Gupta S K & Gupta D K, *Indian J Pure & Appl Phys*, **17** (1979) 775.
12 Batra R K & Sehgal M L, *Nucl Phys A (Netherlands)*, **196** (1972) 638.
13 Gupta S K & Gupta D K, *Jpn J Appl Phys (Japan)*, **19** (1980) 1.
14 Gupta S K & Gupta D K, *J Appl Phys (USA)*, **52** (1981) 1175.
15 Gupta S K & Gupta D K, *Indian J Pure & Appl Phys*, **18** (1980) 461.
16 Takhar P S, Gill T S & Sehgal M L, *Proceedings of the 11th Rare Earth Research conference*, Vol. 1, 1974, 89.
17 Katz L & Penfold A S, *Rev Mod Phys (USA)*, **24** (1952) 28.
18 Tabata T, Ito R, Okabe S & Fujita Y, *Phys Rev B (USA)*, **3** (1971) 572.
19 Gupta S K & Gupta D K, *Continuous slowing down approximation range of* 50 keV-100 MeV *positrons*, paper submitted to the VIth International Conference on Positron Annihilation, Univ. of Texas, Arlington (USA), 1982.
20 Patrick J R & Ruppal A S, *Phys Lett A (Netherlands)*, **35** (1971) 235.
21 Thontadyra S R & Umakanta N, *Phys Rev B (USA)*, **4** (1971) 1632.
22 Gubernator K, *Z Phys (Germany)*, **152** (1958) 183.
23 Seliger H H, *Phys Rev (USA)*, **100** (1955) 1029.
24 Elwert G, *Ann Phys (Germany)*, **34** (1939) 178.
25 Koch H W & Motz J M, *Rev Mod Phys (USA)*, **31** (1959) 29.
26 Rohrlich F & Carlson B C, *Phys Rev (USA)*, **93** (1954) 38.
27 Sternheimer R M & Peierls R F, *Phys Rev B (USA)*, **3** (1971) 3681.
28 Berger M J & Seltzer S M, *Tables of energy losses and ranges of electrons & positrons*, NASA-SP-3012, 1964.
29 Gupta S K, Govil J C, Gupta D K *et al.*, *Int J Appl Rad & Isotope (USA)*, 1982, in press.

Indian Journal of Pure & Applied Physics
Vol. 21, January 1983, pp 56-58

Electronic & Vibrational Spectra of 3-Amino-2-chloropyridine

NITISH K SANYAL*,
S L SRIVASTAVA & (Mrs) ANANDA DEVI
Department of Physics, University of Gorakhpur, Gorakhpur 273001

Received 22 *January* 1980; *accepted* 8 *November* 1982

Results of an investigation on the electronic (3120-2900 Å) and infrared absorption (400-4000 cm^{-1}) spectra of 3-amino-2-chloropyridine are presented. Electronic bands have been analyzed in terms of two ground state (387 and 562 cm^{-1}) and seven excited state (240, 345, 525, 576, 822, 864 and 1187 cm^{-1}) fundamental vibrational frequencies with the 0,0 band at 3052.4 Å. The vibrational spectra have been analyzed in terms of fundamentals, their combinations and overtones. Assignments of the fundamentals in each spectrum have also been proposed.

Spectroscopic studies of pyridine[1] and mono-[2-5] or disubstituted[6-8] pyridines received considerable attention in the recent years due to the importance of pyridine-like molecules in various biological systems.

The present investigation on the electronic and vibrational spectra of 3-amino-2-chloropyridine deals with the spectroscopic changes caused by two strongly perturbing substituents. In the electronic spectrum, only one band system has been photographed under the best possible experimental conditions. The gross structure of the bands is identical to that of the disubstituted benzenes. On this basis, and also due to the strong appearance of the ring stretching mode ν_1, it has been concluded that the system is due to π-π transition and is analogous to the $^1A_{1g} \rightarrow {}^1B_{2u}$ transition observed in benzene. The absence of the n-π transition is most likely due to the large inductive influence exerted by the chlorine atom on the nitrogen atom of the ring. Similar observations have also been made in the electronic spectrum of 2-bromopyridine by Stephenson[9] and in 3-bromopyridine by Misra[3].

In addition to the electronic spectra, the infrared absorption spectra have also been studied. The vibrational assignment of the infrared bands is made on the basis of group frequency approach together with the data available for similar molecules.

Experimental procedure—The electronic absorption spectrum has been photographed on Hilger medium quartz spectrograph using different path-lengths of the absorbing column and optimum heating. Large number of bands appearing in the region (3120-2900 Å) have been obtained at 40 °C with a path-length of 1 m. Bands, in general, are strong and sharp. The accuracy for sharp bands is up to ± 5 cm^{-1} while it drops to ± 10 cm^{-1} in case of weak, broad and diffuse bands. The position of the bands in cm^{-1}, their intensity, their separation from the 0,0 band and their assignment are presented in Table 1.

The infrared absorption spectra of the molecule under consideration have been recorded using a Beckman double-beam spectrophotometer in the region 400-4000 cm^{-1} in KBr phase. The bands in the

Table 1—Analysis of the Electronic Absorption Spectrum of 3-Amino-2-chloropyridine in the Near Ultraviolet Region

Intensity	Position of band (in cm^{-1})	Separation from 0,0 band, cm^{-1}	Assignment
wd	32076	0 − 676	0 − 562 − 122
ms	32190	0 − 562	0 − 562
wb	32216	0 − 536	0 − 890 + 345
wb	32247	0 − 505	0 − 387 − 122
ms	32365	0 − 387	0 − 387
wd	32437	0 − 314.5	0 − 387 + 69
wd	32539	0 − 213	0 − 562 + 345
m	32630	0 − 122	0 − 122
w	32687	0 − 65	0 − 65
s	32752	0	0,0 band
m	32821	0 + 69	0 + 69
mw	32872	0 + 120	0 + 240 − 122
mw	32930	0 + 178	0 + 240 − 65
m	32992	0 + 240	0 + 240
w	33055	0 + 303	0 + 240 + 69
ms	33097	0 + 345	0 + 345
mw	33152	0 + 400	0 + 525 − 122
w	33222	0 + 470	0 + 525 − 65
s	33277	0 + 525	0 + 525
m	33328	0 + 576	0 + 576
mw	33394	0 + 642	0 + 576 + 69
mw	33447	0 + 695	0 + 2 × 345
mw	33501	0 + 749	0 + 822 − 65
mw	33574	0 + 822	0 + 822
ms	33616	0 + 864	0 + 864
w	33670	0 + 918	0 + 345 + 576
mb	33732	0 + 980	0 + 2 × 525 − 69
mb	33801	0 + 1049	0 + 2 × 525
mw	33898	0 + 1146	0 + 2 × 576
mb	33939	0 + 1187	0 + 1187
m	34096	0 + 1344	0 + 525 + 822
mw	34147	0 + 1395	0 + 525 + 864, 822 + 576
w	34200	0 + 1448	0 + 576 + 864
mw	34337	0 + 1585	0 + 3 × 525
mw	34432	0 + 1680	0 + 864 + 822
mw	34457	0 + 1705	0 + 525 + 1187

s = strong, ms = medium strong, m = medium, mb = medium and broad, w = weak, wb = weak and broad, wd = weak and diffuse, mw = medium and weak

region 400-2000 cm^{-1} are accurate up to ± 10 cm^{-1} and to ± 20 cm^{-1} in the region 2000-4000 cm^{-1}.

Discussion—Pyridine, the parent molecule of the present investigation, belongs to C_{2v} point group. The substitution of chlorine atom at position 2 together with the NH_2-group at position 3 reduces the symmetry of the molecule to C_s. As pointed out earlier, the band-system originates from a π-π transition analogous to $^1A_{1g} \rightarrow {}^1B_{2u}$ transition of benzene. The above transition transforms to $A' \rightarrow A'$ which is an allowed one. In view of the allowed nature of the transition, it is expected that the 0,0 band of the system should appear as a strong one. Several photographs have been taken by having a small amount of vapour in the absorbing column for ascertaining the 0,0 band of the system. In view of the nature and the intensity of the bands thus photographed, the strongest band at 3052.4 Å towards the longer wavelength of the spectrum has been taken as the 0,0 band.

As a consequence of the π-π transition, it is expected that the electronic spectrum should consist of the ring vibrations whereas in the vibrational spectrum, in addition to the ring vibrations, the vibrations associated with the remaining three C −H bonds and the two substituents will also appear. Spectroscopic studies of aromatic molecules show that the vibrations associated with the C—H bonds and also with the group are not sensitive to the substitution. Hence, their positions are very nearly fixed in the spectrum. On the basis of the data available in the literature, the vibrations associated with the three C—H bonds together with the NH-bonds of the NH_2-group are assigned and are listed in Table 2. The discussion is limited to ring vibrations only.

Table 2—Analysis of the Infrared Absorption Bands of 3-Amino-2-chloropyridine

Position of band, cm^{-1}		Assignment
387*	(ms)†	ν_6
480	(m)	
555	(ms)	ν_6
610	(w)	
645	(w)	NH_2 out-of-plane wagging
695	(vs)	ν(C—Cl)
730	(vs)	γ(C—H)
795	(vs)	γ(C—H)
830	(w)	
860	(ms)	ν_1 (ring)
970	(ms)	γ(C—H)
1045††	(m)	NH_2 twisting
1055	(s)	ν_{12}
1075	(s)	
1120	(vs)	β(C—H)
1150	(vs)	β(C—H)
1165	(sh)	
1245	(s)	β(C—H)
1280	(s)	ν(C—NH_2)
1290	(vw)	55+730
1325	(vs)	ν_{14}
1360**	(w)	970+387
1395	(sh)	
1420	(sh)	
1440	(vs)	ν_{19}
1455	(w)	1055+387
1470	(s)	ν_{19}
1540	(m)	1150+387
1570	(s)	
1590	(vs)	ν_8
1615††	(s)	NH_2 in-plane bending
1620††	(s)	
1670	(w)	555+1120
1695	(m)	1150+555
1730	(w)	2×860
1760	(w)	1055+695
1800	(m)	1245+555
1860	(m)	1055+795
1930	(m)	1245+695
1980	(w)	1120+860
2015	(w)	1280+730
2120	(w)	1325+795
2170	(w)	1440+730
2250	(w)	1280+970
2650	(w)	2×1325
2730	(w)	1440+1280
2800	(w)	1470+1325
2870	(w)	1620+1245
2960	(w)	1325+1620
3010	(w)	1440+1590
3030	(w)	ν(C—H)
3040	(w)	ν(C—H)
3060	(w)	ν(C—H)
3180	(m)	2×1590
3320	(ms)	ν(N—H) sym.
3465	(vs)	ν(N—H) asym.
3565	(w)	3030+555
3705	(w)	3320+387
3800	(ms)	3060+730

*taken from the ultraviolet absorption spectra

†terms under this column represent the estimated intensities

**band showing doublet structure

††these bands appear under higher concentration

ν = stretching, β = in-plane bending, γ = out-of-plane bending, vs = very strong, s = strong, ms = medium strong, m = medium, w = weak, vw = very weak and sh = shoulder

The strong bands at 33097 and 33277 cm^{-1} towards the shorter wavelength side of the 0,0 band have been found to involve excited state fundamentals 345 and 525 cm^{-1} respectively. The vibration 345 cm^{-1} has been found to be excited up to three quanta. Medium strong bands at 32365 and 32190 cm^{-1} towards the longer wavelength side involve the corresponding two ground state fundamental vibrational frequencies 387 and 562 cm^{-1} respectively. These two vibrations have been assigned as the components of e_{2g} 608 cm^{-1} planar deformation mode of benzene. Out of the two, the 562 cm^{-1} fundamental is in close agreement with the medium strong infrared band at 555 cm^{-1}; the lower component which lies below 400 cm^{-1} could not be traced in the infrared spectrum.

The two vibrations a_{1g} (992 cm^{-1}) and b_{1u} (1010 cm^{-1}) represent the ring breathing and the carbon trigonal bending mode respectively. Under the reduced C_s symmetry, the two vibrations belong to the same symmetry species a'. Since the energies of the two vibrations are very close, there is an appreciable interaction between the two. Consequently, the energy of the two vibrations is expected to be modified. The ring breathing vibration reduces up to 700 cm^{-1} [Ref. 10-12 depending upon the mass of the substituent while the trigonal bending vibration remains in the close vicinity of 1010 cm^{-1}. In the present investigation, the pair of strong bands at 33574 and 33616 cm^{-1} on the shorter wavelength side of the 0,0 band has been found to involve two excited state fundamental vibrations 822 and 864 cm^{-1}. The overtones of these vibrations could not be identified due to their weak intensity in this region. However, combinations of these vibrations have been found. The ground state vibration corresponding to these modes could not be identified in the electronic spectrum because the spectrum does not extend towards the longer wavelength side. However, two strong infrared bands at 860 and 1055 cm^{-1} have been chosen to represent the corresponding ground state values. These two vibrations have been assigned as the ring-stretching (breathing type) and the ring-bending vibrations respectively.

References

1 Kasha M, *Disc Faraday Soc (GB)*, **9** (1950) 14.

2 Sponer H & Rush J H, *J Chem Phys (USA)*, **20** (1952) 1847.

3 Misra T N, *Indian J Phys*, **35** (1961) 420.

4 Pandey S M, *Spectra of some polyatomic molecules*, Ph D thesis, Gorakhpur University, Gorakhpur, 1966.

5 Pandey B R, *Spectra of some substituted benzenes*, Ph D thesis, Gorakhpur University, Gorakhpur, 1966.

6 Tripathi R S & Pandey B R, *Indian J Pure & Appl Phys*, **12** (1974) 64.

7 Marjit D, *Indian J Phys*, **47** (1973) 480.

8 Srivastava S L, Goel R K & Rohitashava, *J Chim Phys (France)*. **75** (11-12) (1978) 1091-5.

9 Stephenson H P, *J Chem Phys (USA)*, **22** (1954) 1077.

10 Randle R R & Whiffen D H, *Proc symposium on molecular spectroscopy* (Institute of Petroleum, London) Part III, 1954.

11 Whiffen D H & Stojilj-Kovic A, *Spectrochim Acta Vol. A (GB)*, **12** (1958) 42.

12 Padhye M R & Viladkar B G, *J Sci & Ind Res (India)*, **18B** (1959) 504.

Indian Journal of Pure & Applied Physics
Vol. 21, January 1983, pp 59-60

Laser Raman & Far Infrared Spectra of DL-Phenyl Alanine

VINAYA KUMAR & P K VERMA*
Department of Physics, Aligarh Muslim University, Aligarh 202 001

Received 1 *May* 1982

The far infrared spectrum of DL-phenyl alanine has been recorded on FIR-30 spectrophotometer. Laser Raman spectrum of the same molecule has been recorded on laser Raman spectrometer (CODERG T800) using 5145 Å as exciting line. Various fundamentals obtained in far infrared and laser Raman spectrum have been correlated and assigned to particular normal modes of vibration. The vibrations observed have been assigned with the help of assignments given for poly-L-alanine.

The far infrared spectrum of poly-L-alanine (hereafter abbreviated as PLA) was measured in the region below 800 cm^{-1} by Miyazawa *et al.*[1]. They have described the various infrared active vibrations of PLA chains and the N-deuterated chains. The *GF* matrix method[2,3] was used for the numerical calculations. The vibrational assignments of the observed frequencies and calculated frequencies are given by Miyazawa *et al.*[1] They have reported the observed frequencies of PLA up to 295 cm^{-1}. Below this region there are no observed frequencies. The frequencies below 295 cm^{-1} have been calculated and have been reported by them[1]. In the present note, far infrared and corresponding laser Raman spectrum have been reported, for the first time for DL-phenyl alanine. Most of the frequencies have been assigned with the help of assignments given for PLA molecule. Combination bands have also been proposed with the help of various observed fundamentals. Some Raman frequencies have been identified corresponding to some far infrared vibrations.

The pure chemical DL-phenyl alanine was obtained from the Nutritional Biochemicals Corp., Ohio, USA in powder form at room temperature. It was used as such without further purification. The far infrared spectrum of DL-phenyl alanine (Fig. 1) was recorded on FIR-30 spectrophotometer in the region 50-500 cm^{-1}. The laser Raman spectrum of the same compound (Fig. 2) has been recorded on the laser Raman spectrometer CODERG T800 using 5145 Å as exciting line having the power 200 mW. Single monochromator was used. Spectral resolution was 2 cm^{-1}.

Raman and infrared spectra of DL-phenyl alanine have been analyzed (Tables 1 and 2) on the basis of infrared spectrum of PLA. The observed and calculated vibrations of PLA have been used in the

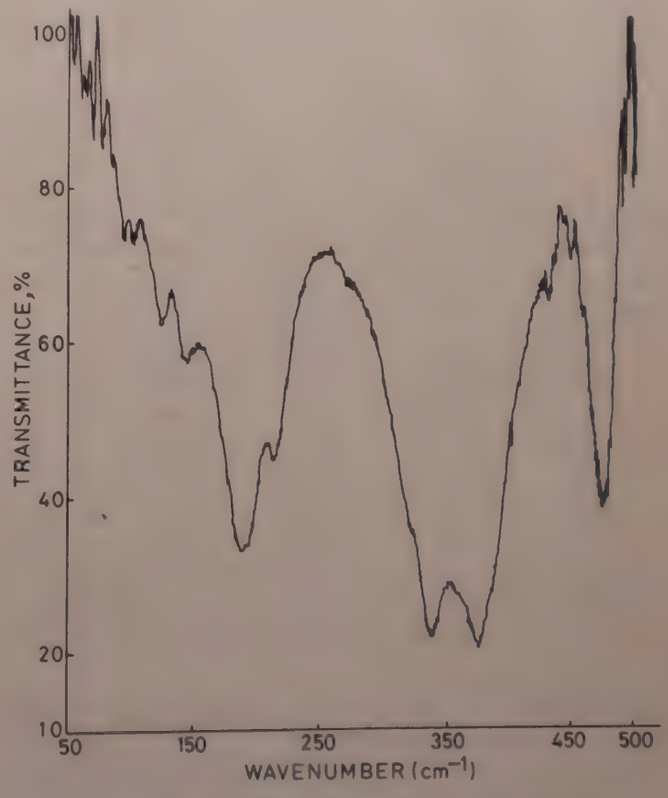

Fig. 1—Far infrared spectrum of DL-phenyl alanine

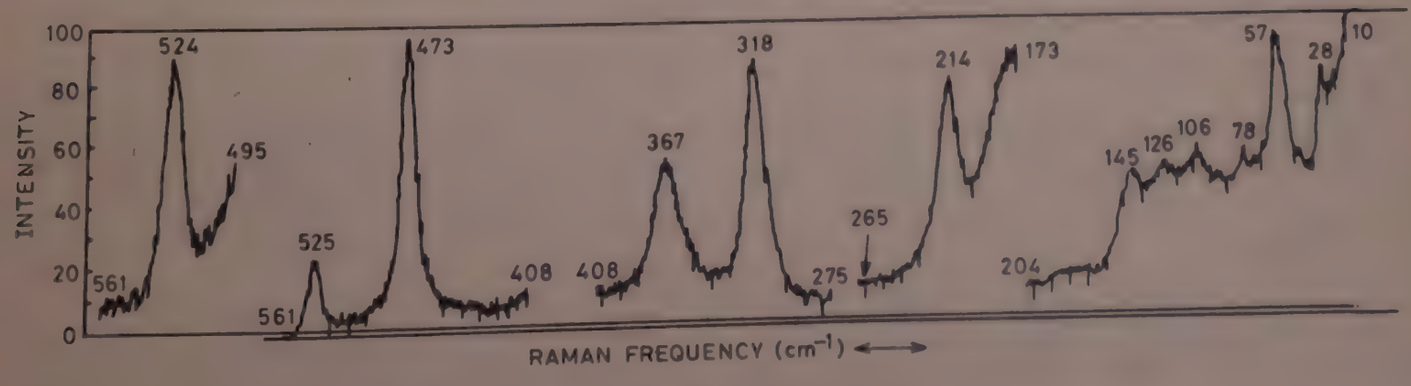

Fig. 2—Laser Raman Spectrum of DL-phenyl alanine

Table 1—Analysis of Far Infrared Spectrum of DL-Phenyl Alanine

Symmetry species	Frequency (cm^{-1})	Rel. int.	Assignment
	57.5	0.2	210-155
	62.5	0.7	
	69.0	0.5	
	73.0	0.2	155-81
a'	81-5	1.0	tCC' Internal rotation
a''	100.0	2.5	tCN "
	110.0	2.5	210-100
a'	133.0	3.4	
a''	155.0	4.1	
a'	210.0	5.4	tCN
	260.0	2.9	210+57.5
a'	353.0	7.2	C—C—CH_2 triognal bending
a'	428.0	3.2	2×210
a'	440.0	2.4	353+100
a''	453.0	2.5	353+100
a''	490.0	1.1	
a'	493.0	0.9	353+133
a''	500.0	0.3	353+155

Table 2—Correlation of Raman Frequencies with the Infrared Frequencies (in cm^{-1}) of DL-Phenyl Alanine

Raman frequencies	Rel. int.	Infrared frequencies	Assignment
57.0	9.3	57.5	210-155
78.0	5.8	81.5	tCC'(a') Internal rotation
106.0	6.1	110.0	210-100
145.0	4.9	155.0	a''
214.0	8.1	210.0	tCN(a')
265.0	1.2	260.0	210+57.5
495.0	5.4	493.0	353+133(a')

assignments of the various normal modes of vibrations observed in DL-phenyl alanine.

The symmetry of the molecule has been taken as C_s because the substituents $CH_2CH(NH_2)COOH$ do not lie in the plane of the molecule. Therefore the plane of the molecule is the only element of symmetry in the present case. In this case two types of vibrations are expected to appear namely, a' and a''. a' vibrations are totally symmetric whereas a'' vibrations are asymmetric.

Vibrational frequency at 81:5 cm^{-1} observed in far infrared spectrum of DL-phenyl alanine has been correlated with the 78 cm^{-1} vibrational frequency observed in laser Raman spectrum. This vibration has been assigned as torsional —CC' vibration of totally symmetric type. In PLA molecule this vibration has been assigned to the same mode of vibration by Miyazawa *et al.*[1] However, they have given a theoretically calculated value of the above mentioned vibration.

The vibrational frequency observed at 110 cm^{-1} in far infrared spectrum of DL-phenyl alanine has been assigned as the difference vibration (210-100). Corresponding to this mode of vibration, a Raman frequency has been observed at 106 cm^{-1}.

The vibrational band observed at 155 cm^{-1} in far infrared spectrum has been correlated with the 145 cm^{-1} frequency obtained in laser Raman spectrum. This frequency is of asymmetric type having the mode of vibration of torsion—NCC'.

The vibration 210 cm^{-1} observed in infrared spectrum has been assigned to torsion CN mode of vibration. The corresponding vibration in Raman spectrum has been obtained at 214 cm^{-1}.

The 260 cm^{-1} vibration has been taken as a combination (210+57.5). The same vibration has been observed at 265 cm^{-1} in laser Raman spectrum.

The vibration at 353 cm^{-1} observed in far infrared spectrum has been assigned as trigonal bending mode of vibration C—C—CH_2.

The 493 cm^{-1} vibration with weak intensity observed in far infrared spectrum has been correlated with the 495 cm^{-1} vibration observed in laser Raman spectrum. This vibration has been assigned as a combination vibration (353+133).

The vibrational frequency at 100 cm^{-1} observed in far infrared spectrum has been assigned as torsional CN mode of vibration. This vibration is of asymmetric type. All other vibrations have been assigned as combinations of the fundamental vibrations.

The authors are extremely grateful to Prof. M Z R Khan for his encouragement during this work. One of the authors (VK) is grateful to the University Grants Commission, New Delhi for financial assistance.

References

1 Miyazawa T, Fukushima K, Sugano S & Masuda Y, in *Conformation of biopolymers*, edited by G N Ramachandran (Academic Press, London) 1967, 557.
2 Wilson E B, *J Chem Phys (USA)*, 7 (1939) 1047.
3 Wilson E B, *J Chem Phys (USA)*, 9 (1941) 76.

Indian Journal of Pure & Applied Physics
Vol. 21, January 1983, pp 61-62

Electronic Absorption Spectrum of 2-Chloro-6-Methyl-Benzonitrile in Vapour Phase

R K GOEL*, S K SHARMA† & S N SHARMA††
Department of Physics, D N College, Meerut 250002

Received 5 December 1981

The near ultraviolet absorption spectrum of 2-chloro-6-methyl-benzonitrile in vapour phase has been recorded and analysed. The spectrum corresponds to the 2600 Å transition in benzene. The 0,0 band has been observed at 34471 cm^{-1}. Strong bands at 130, 283 and 388 cm^{-1} towards the longer wavelength side of the 0,0 band correspond to ground state fundamentals while those at 215, 312, 519, 592, 902, 1028 and 1120 cm^{-1} towards the violet side represent the excited electronic state fundamentals. The assignment of the ground and excited state fundamental frequencies to the probable modes of vibration has also been made.

The analyses of the near ultraviolet absorption spectra of benzonitrile and mono-halogenobenzonitriles have appeared in literature[1-4]. Padhye and Varadarajan[5] have reported on the electronic absorption spectrum of three isomeric tolunitriles wherein the CH_3 group was electron donating and the CN group, electron withdrawing. The present note reports the results of a study on the ultraviolet absorption spectrum of 2-chloro-6-methyl-benzonitrile undertaken with a view to (i) examine the effect of one additional chlorine atom to tolunitrile which may act as electron donating by mesomeric effect and electron withdrawing by inductive effect and (ii) propose a vibrational analysis and assignments to the electronic bands.

The spec-pure chemical, 2-chloro-6-methyl-benzonitrile obtained from M/s Koch-Light Laboratories, England, was used as such. The electronic absorption spectrum in vapour phase was recorded on Beckman DK-2A ratio recording spectrophotometer (scanning time 100 s) at various temperatures (25 to 60°C) using a cell (10 cm path length). 22 Distinct bands were observed and the analysis of the observed bands is given in Table 1. The assignment of the fundamentals to the probable modes of vibration is represented in Table 2.

The molecule under investigation belongs to C_s point group under which the forbidden electronic transition of benzene $^1B_{2u} \leftarrow {}^1A_{1g}$ (2600 Å) becomes A'-A' which is an allowed transition with the transition moment lying in the plane of the molecule. The present spectrum extends from 2790 Å to 2935 Å. The most intense band at 34471 cm^{-1} towards the longer wavelength side, in view of the group theoretical rule

Table 1—Analysis of the Electronic Absorption Bands of 2-Chloro-6-Methyl-Benzonitrile

Int.*	Position of band (cm^{-1})	Separation from 0,0 band cm^{-1}	Assignment
m	34083	0−388	0−388
m	34130	0-341	0−2×283+215
m	34188	0−283	0−283
m	34305	0−166	0−388+215
ms	34341	0−130	0−130
w	34435	0−36	0−36, (0−2×130+215)
vvs	34471	0,0	0,0
s	34686	0+215	0+215
ms	34783	0+312	0+312
mw	34855	0+384	0+519−130
ms	34904	0+433	0+2×215
s	34990	0+519	0+519
s	35063	0+592	0+592
ms	35112	0+641	0+3×215
mw	35224	0+753	0+519+215
w	35311	0+840	0+519+312
ms	35373	0+902	0+902
w	35423	0+952	0+2×215+519
s	35499	0+1028	0+1028
vs	35600	0+1129	0+1129
vs	35689	0+1218	0+902+312
s	35842	0+1351	0+2×519+312

*w: weak, mw: medium weak, m: medium, ms: medium strong, s: strong, vs: very strong, vvs: very, very strong

Table 2—Correlation of Fundamental Vibrational Frequencies of 2-Chloro-6-Methyl-Benzonitrile in Infrared, Raman and Ultraviolet Spectra and Their Assignment

(All values in cm^{-1})

Raman[a]	IR[b]	Electronic spectrum		Assignment*
		Ground state value	Excited state value	
140	—	130	—	γ(C—Cl)
—	299	283	215	γ(C—CN)
390	399	388	312	e_{2u}(404)
580	564	—	519	β(C≡N)
—	723		592	φ(C—C—C)
1092	1077	—	902	ν(C—Cl)
—	1179	—	1028	ν(C—CN)
1234	1209	—	1129	ν(C—CH_3)

*ν: Stretching, β: in-plane bending, γ or φ: out-of-plane deformation
[a]Values from Ref. 6, [b]Values from Ref. 7

†Department of Textile Technology, Indian Institute of Technology, New Delhi 110016.
††Analytical Physics Section, Indian Institute of Petroleum, Dehra Dun 248005.

and Franck-Condon principle, has been identified as the 0,0 band in the present case. The bands with separations 130, 283 and 388 cm^{-1} on the longer wavelength side were taken as the fundamentals of the ground electronic state and these agree well with the corresponding Raman[6] and infrared[7] frequencies of the title compound. Excited state fundamental frequencies can be located at 215, 312, 519, 592, 902, 1028 and 1129 cm^{-1} in the present study.

Green *et al.*[8] have assigned a frequency in the region 200-110 cm^{-1} to C —Cl out-of-plane bending mode in various chloro-substituted benzenes. Thus, the ground state vibration at 130 cm^{-1} has been correlated to the above mode in the present case, which finds support from the corresponding Raman shift[6] at 140 cm^{-1}.

Duncan and Janz[9] and Halverston *et al.*[10] assigned the bands at 226 and 242 cm^{-1} to C—CN out-of-plane bending mode in propionitrile and acrylonitrile respectively. The ground state vibration at 283 cm^{-1} has been correlated to this mode. The corresponding IR frequency was observed at 299 cm^{-1} while the corresponding excited state vibration has been identified at 215 cm^{-1} which has been traced up to three quantas and combine with a good number of fundamentals.

Bishui[11] assigned the C—Cl stretching mode at 1050 and 1070 cm^{-1} in 2,6-dichloroaniline and Sherer and Evans[12] assigned this mode at 1070 and 1152 cm^{-1} in *m*-dichlorobenzene. In view of these, the excited state frequency at 902 cm^{-1} has been correlated to this mode. Its IR analogue has been taken at 1077 cm^{-1} (Table 2).

The upper state fundamental at 1028 cm^{-1} with corresponding IR frequency at 1179 cm^{-1} has been correlated to the C—CN stretching mode, which finds support from the work of Pandey and Singh[3]. Similarly the excited state frequency at 1129 cm^{-1} has been correlated to C—CH_3 stretching mode which has the corresponding IR and Raman frequencies[6,7] at 1209 and 1234 cm^{-1} respectively.

The 0,0 band in case of benzonitrile and *o*-chlorobenzonitrile were found[3] to be respectively at 36516 and 35156 cm^{-1}. In view of the behaviour of tolunitrile, Varadarajan and Parthasarathy[4] concluded that the red shift of 0,0 band is more in case of *o*-chlorobenzonitrile as compared to *m*- and *p*-chlorobenzonitriles. The molecule presently studied has an additional electron donating group CH_3 and thus more red shift is expected in the present case as compared to *o*-chlorobenzonitrile. The 0,0 band observed at 34471 cm^{-1} in the present case shows the red shift compared to that of the 0,0 band of *o*-chlorobenzonitrile, as expected.

The authors are thankful to Prof. Nitish K Sanyal, Head of the Physics Department, Gorakhpur University, for encouragement.

References

1 Hirt R C & Howe J P, *J Chem Phys (USA)*, **16** (1948) 480.
2 Bass M, *J Chem Phys (USA)*, **18** (1950) 1403.
3 Pandey S M & Singh S J, *Indian J Pure & Appl Phys*, **14** (1976) 587.
4 Varadarajan T S & Parthasarathy S, *Indian J Pure & Appl Phys*, **11** (1973) 341.
5 Padhye M R & Varadarajan T S, *J Scient Ind Res (India)*, **21B** (1962) 241.
6 Goel R K, Sharma S D & Jaiswal R M P, *Proc Nat Acad Sci (India)*, **48A** (1978) 251.
7 Goel R K, Sharma S D & Sharma S N, *Indian J Pure & Appl Phys*, **17** (1979) 55.
8 Green J H S, Harrison D J & Kynaston W, *Spectrochim Acta Ser A (GB)*, **27** (1971) 807.
9 Duncan N E & Janz G Z, *J Chem Phys (USA)*, **23** (1955) 434.
10 Halverston F, Stamm R F & Whallen J J, *J Chem Phys (USA)*, **16** (1948) 808.
11 Bishui P K, *Indian J Pure & Appl Phys*, **10** (1972) 637.
12 Sherer J R & Evans J C, *Spectrochim Acta (GB)*, **19** (1963) 1739.

Indian Journal of Pure & Applied Physics
Vol. 21, January 1983, pp 63-64

Ellipsometric Determination of the Distribution of Particles in a Residual Layer

J ASHOK* & P L H VARA PRASAD

Thin Films Research Laboratories, Department of Applied Physics, Andhra University, Waltair 530003

Received 23 *January* 1982; *accepted* 11 *November* 1982

The substrates for most optical thin films are of optical glass, subjected to various stages of grinding, polishing and cleaning. Ellipsometric studies of polish layer on some optical glasses show that the physical properties of polish layer are different from those of the bulk of the glass. The optical constants of the surface layers give an idea of the size and distribution of the particles on the substrate.

The effective refractive index of a substrate can be substantially different from the quoted value depending on the treatment it is subjected to. Various treatments on glass leave some surface layers. Ellipsometric studies of polish layer on some optical glasses showed that the physical properties of polish layer are different from those of the bulk of the glass[1,2]. For the indigenous production of optical and optoelectronic components in India, ellipsometric studies were made on glass substrates at different stages of polishing and cleaning[3,4]; the glass substrates were supplied by the Central Glass and Ceramics Research Institute, Calcutta.

The optical constants of these surface layers are determined ellipsometrically considering them as continuous. In actuality, it is more probable that no continuous layer is present and the surface is covered by a number of minute particles separated by small distances. This disordered placement of minute particles accounts for the surface film. The optical constants of these surface layers give information about the size and distribution of the particles on the substrate.

While the material which forms the surface layers in a number of cases is nonabsorbing, the films themselves are found to exhibit a slight amount of absorption. This is due to granularity in film structure and consequent scattering effects[5]. Thus it is more probable in actuality that no continuous layer is present and the surface is covered by a number of minute particles, separated by small distances.

For a periodic, rough surface like a grating (Fig. 1), the rms roughness or thickness of the film (obtained from a periodic sawtooth profile using the definition of rms value) will be[5]

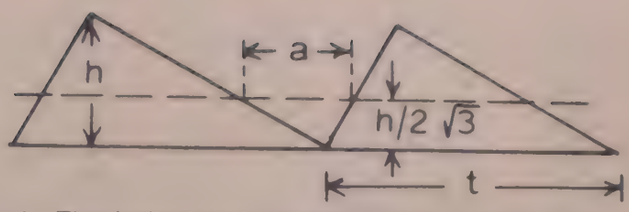

Fig. 1—The distribution of particles in a periodic rough surface—a grating

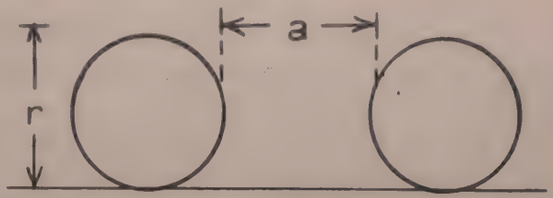

Fig. 2—The distribution of spherical particles in a residual surface layer

$$t = \sigma_{rms} = h/2\sqrt{3} \qquad \ldots(1)$$

where h is the maximum depth of the groove.

The distribution of particles in a residual film under consideration is shown in Fig. 2. The residual layer can be thought of as equivalent to a number of minute spherical particles of diameter r, separated from one another by a small distance a.

For the spherical particles under consideration, the same equation for the equivalent-formed substrate for a grating holds good as the diameter of the spherical particle and the depth of the triangular groove indicate the same maximum deviation from the substrate surface. Thus r can be calculated from the above relation.

The parameter a is the correlation distance or the distance between two particles, as they both indicate the extent of inhomogeneity. In the case of a grating, this parameter is two-dimensional, whereas it is three-dimensional in the case of spherical particles.

It is convenient to measure a by a dimensionless parameter[6] Q, given by

$$Q = 2(k)a \qquad \ldots(2)$$

where $k\left(=\frac{2\pi}{\lambda}\times N\right)$ is the average wavenumber in the medium whose refractive index is N and λ is the wavelength of radiation in the medium.

Q, a measure of inhomogeneity, in turn, can be measured using the reflectivity R of the film, through the relation[7]

$$R = \left[\frac{n-Q}{n+Q}\right]^2 \qquad \ldots(3)$$

where n is the refractive index of the substrate. The reflectivity of a film, in turn, can be calculated from the

Table 1—Distribution of Residual Particles on Polished Glass Surface after Cleaning with Detergent, Ultrasonic Vibrations and Ionic Bombardment (All a and r values are in Å)

No. of strokes given for polishing	Direct from polishing		Detergent cleaning				Ultrasonic cleaning				Ionic cleaning			
			Conc., 50%		Conc., 75%		45 min		60 min		2A		3A	
	a	r	a	r	a	r	a	r	a	r	a	r	a	r
100	173	6114	126	727	145	693	103	703	145	693	117	693	145	693
120	170	5976	126	727	149	624	101	700	149	624	102	700	149	624
140	168	6062	136	727	140	606	123	714	140	606	149	731	140	606
160	175	5976	140	727	140	606	150	731	140	606	103	703	140	606

refractive indices of the film, substrate, medium and the extinction coefficient (K) from the general equations given in any standard textbook[7,8].

Determining the refractive index N_1 of the film, thickness t and K ellipsometrically, we can evaluate Q from which a can be measured.

The film under study is slightly absorbing with very low absorption coefficient. The reflectivity equation for a nonabsorbing film can be readily used in determining the reflectivity of the film since this does not affect considerably the values of a and r. However, the calculated values of a and r with and without considering this slight absorption coefficient do not differ by more than 10-15 Å.

The ellipsometric studies of a residual film on a polished glass (refractive index = 1.5186), cleaned with different normal procedures, have given the following values for different parameters: $t = 175$ Å, $N_1 = 2.125$, $K = 0.0018$, $a = 140$ Å and $r = 606$ Å.

The pattern of the distribution of particles in various residual films, formed on glass substrates at different stages of polishing and cleaning[3,4], is shown in Table 1. The variations are found to be more effective after adequate cleaning. The particle size (r) and the distance between the particles (a) are calculated from the ellipsometrically determined values of optical constants of surface films. The particle size is found to be reducing with the increasing number of strokes and the distance between the particles is increasing with various cleaning treatments. The various cleaning treatments remove some of the particles in a residual layer while the increased number of strokes reduce the particle size.

One of the authors (PLHVP) is grateful to the CSIR, New Delhi, for the financial assistance.

References

1 Sissingh R & Grossmuller J Th, *Phys Z (Germany)*, **27** (1926) 518.

2 Vasicek A, *Kolloid Z (Germany)*, **86** (1936) 288.

3 Ashok J & Vara Prasad P L H, *Indian J Pure & Appl Phys*, **19** (1981) 395.

4 Ashok J & Vara Prasad P L H, *Indian J Pure & Appl Phys*, **20** (1982) 425.

5 Azzam R M A & Bhashara N M, *Phys Rev (USA)*, **5** (1972) 4721.

6 Ross G, *Opt Acta (GB)*, **16** (1969) 95.

7 Vasicek A, *Optics of thin films* (North-Holland, Amsterdam), 1960, 123, 153, 294.

8 Born M & Wolf E, *Principles of optics* (Pergamon Press, Oxford), 1970, 615.

Indian Journal of Pure & Applied Physics
Vol. 21, January 1983, pp 65-66

Ultrasonic Velocity in Binary Liquid Mixtures: *m*-Xylene, *o*-Xylene, CCl_4 & Toluene in Nitrobenzene**

S N JAJOO*, V S DEOGAONKAR & C S ADGAONKAR,
Department of Physics, Vidarbha Mahavidyalaya, Amravati 444 604

Received 22 *March* 1982; *revised received* 4 *September* 1982

Ultrasonic velocities in binary liquid mixtures of nitrobenzene (a strongly polar liquid) with *m*-xylene, *o*-xylene, CCl_4 and toluene (weakly polar liquids) have been calculated theoretically, based on free length theory (FLT) due to Jacobson and collision factor theory (CFT) due to Schaaffs. Comparison of these theoretical values with the experimental ones shows that, in these mixtures, the CFT is preferable to the FLT.

The free length theory (FLT) of Jacobson[1] and the collision factor theory (CFT) of Schaaffs[2] have been applied successfully to binary liquid mixtures by a number of workers[3-7]. In continuation of our previous studies on the binary liquid mixtures of polar + nonpolar molecules[8] and polar + polar molecules[9], it is thought worthwhile to study mixtures having one component a highly polar and the other weakly polar. As such, sound velocities in binary liquid mixtures containing nitrobenzene with *m*-xylene, *o*-xylene, toluene and CCl_4 have been determined experimentally using ultrasonic interferometer (frequency 2 MHz and accuracy ±0.5%). Measurements were carried out at 38°C for the first two and at 36.5°C for the remaining two liquid mixtures. Density measurements were done by density bottle using chemical balance. The error in the measurements of sound velocity was estimated to be 0.08% (average of 10 measurements on *m*-xylene at 38°C).

Theory—According to Schaaffs, the sound velocity in a pure liquid is given by

$$U = U_\infty SB/V_M \qquad \ldots(1)$$

where $U_\infty = 1600$ m/sec; S = collision factor and $\frac{B}{V_M}$ = space filling factor, B is the actual volume of molecules per mole, while V_M is the molar volume.

For binary liquid mixtures this formula was modified by Nutsch-Kuhnekies[10] as:

$$U_{mix} = U_\infty \left[\frac{(X_A S_A + X_B S_B)(X_A B_A + X_B B_B)}{V_M}\right] \qquad \ldots(2)$$

where X represents the molar concentration, and B is given by:

$$B = \tfrac{4}{3}\pi r^3 N \qquad \ldots(3)$$

In Eq. (3), N is the Avogadro number and r the molecular radius.

To calculate r Schaaffs formula was used:

$$r = \alpha\left[1 - \beta\left\{\left(1 + \frac{1}{3\beta}\right)^{\frac{1}{2}} - 1\right\}\right]^{\frac{1}{3}} \qquad \ldots(4)$$

where $\alpha = \left(\frac{3V_M}{16\pi N}\right)^{\frac{1}{3}}$; $\beta = \frac{\gamma RT}{MU^2}$; γ is the ratio of principal specific heats, R the gas constant and M the molecular weight.

According to Eyring and Hirschfelder[11] the intermolecular free length (L_f) in a liquid is given by:

$$L_f = \frac{2V_a}{Y} \qquad \ldots(5)$$

with

$$V_a = V_M - V_0 \qquad \ldots(6)$$

where V_a is the available volume; V_0, volume at 0 K; Y, the surface area per mole.

From the experimental value of the sound velocity, V_a can be calculated from following relation:

$$V_a = V_M\left(1 - \frac{U_{exp}}{U_\infty}\right) \qquad \ldots(7)$$

where K is the temperature dependent constant. For binary liquid mixtures

$$L_{mix} = 2\left[\frac{V_M - (X_A V_0^A + X_B V_0^B)}{X_A Y_A + X_B Y_B}\right] \qquad \ldots(8)$$

Comparison of theoretically evaluated and experimental results—Comparison of the theoretical and experimental values of ultrasonic velocities for the systems under investigation is shown in Figs 1 and 2. Surface areas (Y) and collision factor (S), the adjustable parameters of FLT and CFT are calculated from Eqs (1), (5) and (8) respectively.

An examination of Fig. 1 shows that the agreement between the experimental and theoretical values of ultrasonic velocities is excellent for (*m*-xylene + nitrobenzene) and (*o*-xylene + nitrobenzene) with the deviation being not more than 1.5%. Collision factors of *m*-xylene and *o*-xylene are nearly equal to that for nitrobenzene. Schaaffs has shown that CFT is more applicable for such cases. As shown in Fig. 2, marked deviation of 5% and 3.5% is observed for

**Paper presented to the Physics section of the 69th session of Indian Science Congress Association, held at Mysore in January 1982.

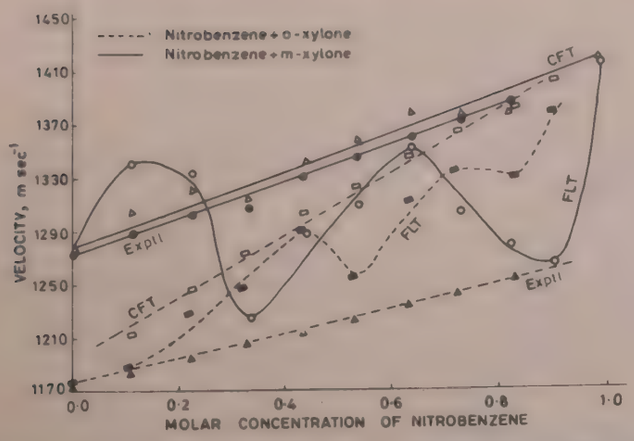

Fig. 1—Comparison of the calculated and experimental values of ultrasonic velocities in mixtures: ———, (Nitrobenzene + *m*-xylene) and -----, (Nitrobenzene + *o*-xylene)

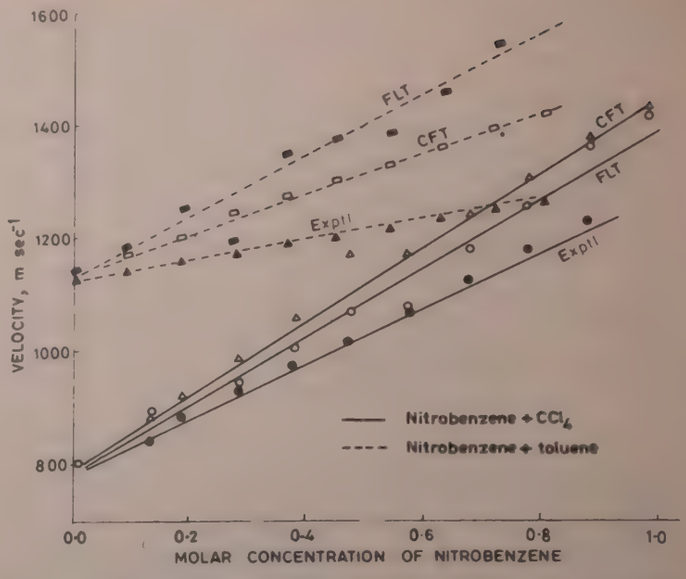

Fig. 2—Same as in Fig. 1 for the mixtures: ———, (Nitrobenzene + CCl_4) and -----, (nitrobenzene + toluene)

(CCl_4 + nitrobenzene) and (toluene + nitrobenzene) respectively. This may possibly be due to large difference in the collision factors of the constituents of the mixtures.

Comparison of experimental values of ultrasonic velocities with those calculated from FLT shows a marked deviation of more than 5% for all the systems except (CCl_4 + nitrobenzene). For this system the deviation is only about 2.5%. This large deviation may possibly be due to high dipole moment of nitrobenzene. Kaulgud and Tarsekar[12] have shown that for systems containing strongly dipolar mixtures FLT is not satisfactory. The same has been observed by us in the systems presently studied.

Hence comparison of the two theories reveals that CFT is better applicable than the FLT for the systems under investigation.

One of the authors (SNJ) is grateful to the University Grants Commission, New Delhi for the financial assistance.

References

1 Jacobson B, *Acta Chem Scand* (*Denmark*), **6** (1952) 1485.

2 Schaaffs W, *Molekularakustik* (Springer-Verlag, Berlin) 1963, Chaps XI and XII.

3 Kaulgud M V, *Acustica* (*Germany*), **10** (1960) 316.

4 Kaulgud M V, *Indian J Phys*, **36** (1962) 577.

5 Sheshadri K & Reddy K C, *J Acoust Soc India*, **4** (1973) 151.

6 Sheshadri K & Reddy K C, *Acustica* (*Germany*), **29** (1973) 59.

7 Mishra R L & Pandey J D, *Indian J Pure & Appl Phys*, **15** (1977) 505.

8 Adgaonkar C S, Jajoo S N & Deogaonkar V S, *Acoustics Lett* (*GB*), **2** (1979) 34.

9 Jajoo S N, Adgaonkar C S & Deogaonkar V S, *Acustica* (*Germany*), **46** (1980) 111.

10 Nutsch-Kuhnekies R, *Acustica* (*Germany*), **15** (1965) Beih 183.

11 Eyring H & Hirschfelder J O, *J Phys Chem* (*USA*), **41** (1937) 249.

12 Kaulgud M V & Tarsekar V K, *Acustica* (*Germany*), **25** (1971) 4.

Indian Journal of Pure & Applied Physics
Vol. 21, January 1983, pp 67-68

Ultrasonic Velocity & Adiabatic Compressibility of Triphenyltin Chloride in Acetone at Various Temperatures

T N SRIVASTAVA*,
R P SINGH & BHAGWAN SWAROOP
Department of Chemistry, Lucknow University, Lucknow 226007

Received 4 *February* 1982; *revised received* 6 *July* 1982

Ultrasonic velocity of solutions of triphenyltin chloride in acetone was measured, for the first time, at 30, 35, 40 and 45°C, using a single-crystal interferometer at a frequency of 2 MHz. The ultrasonic velocity, density and concentration were used to calculate adiabatic compressibility, intermolecular free length, molar sound velocity, specific acoustic impedance, molar volume, apparent molal compressibility and solvation number. The results are interpreted in the light of solute-solvent interaction.

The sound velocity is purely a thermodynamic function and related to other thermodynamic quantities. The determination of some of the parameters on the basis of ultrasonic measurements is reported to be more accurate than that obtained by direct methods.

From the ultrasonic velocity (v)[1,2], adiabatic compressibility (β), intermolecular free length (L_f), molar sound velocity (R), specific acoustic impedance (Z), apparent molal compressibility (φ_K), molar volume (V) and solvation number (S_n) are calculable with the help of the following equations:

$$\beta = \frac{1}{v^2 \rho} \quad \ldots(1)$$

$$Z = v\rho \quad \ldots(2)$$

$$L_f = K\sqrt{\beta} \quad \ldots(3)$$

$$R = V \times v^{\frac{1}{3}} \quad \ldots(4)$$

$$\varphi_K = (\rho_0 \beta - \rho \beta_0)\frac{1000}{\rho_0 C} + \frac{\beta_0 M_2}{\rho_0} \quad \ldots(5)$$

$$V = \frac{\bar{M}}{\rho} \quad \ldots(6)$$

$$S_n = \frac{n_1}{n_2}\left(1 - \frac{\beta}{\beta_0}\right) \quad \ldots(7)$$

where ρ_0 and ρ are the densities of solvent and solution; M_2, molecular weight of the solute; β_0 and β the adiabatic compressibilities of solvent and solution; K, Jacobson's constant[3]; C, concentration in mol/litre and M, effective molecular weight $= \frac{n_1 M_1 + n_2 M_2}{n_1 + n_2}$; n_1 and n_2 are the number of moles of solvent and solute respectively.

In this note, the results of the ultrasonic studies of a simple organometallic system, i.e. triphenyltin chloride (Ph_3SnCl) in acetone, are discussed for the first time. Since organotin derivatives are readily hydrolyzed and their reactions are usually carried out in non-aqueous medium, the choice of a solvent for examining the reactivity is of primary importance. We have, therefore, selected systems containing organotin moieties and non-aqueous solvents of varying polarity for such studies. The results for one such system are reported here.

Experimental details— Triphenyltin chloride was prepared and purified by conventional method[4] and acetone was purified by standard method described by Weissberger[5]. The densities of the liquids were measured by calibrated dilatometer at different temperatures, and v was measured by a single-crystal ultrasonic interferometer at a frequency of 2 MHz at different temperatures. The cell of the interferometer was maintained at different temperatures by circulating water from a thermostatic bath. The error in these measurements is within $\pm 0.05\%$.

Results and discussion—The trends of variation of various parameters, viz. v, β, L_f, R, Z, S_n, and φ_K are presented graphically in Fig. 1 [(A)-(F)]. The graphs indicate that v and Z increase with the increasing C while β, L_f, φ_K and S_n decrease with C. The variation of v in solution depends upon the increase or decrease of L_f after mixing. On the basis of a model for sound propagation proposed by Eyring and Kincaid[6], v should increase if L_f decreases as a result of mixing the two components. They have indicated that L_f is a predominant factor in determining the variation of v in a solution. As shown by Fig. 1(C), L_f decreases on increasing C of Ph_3SnCl which results in the increase of velocity in the same order. The change in L_f, according to Eyring and Kincaid[6], also indicates that there is significant interaction between the solute and solvent molecules due to which structural arrangement is considerably affected.

The data also indicate that the quantity $d\rho/dC$ is positive while $d\beta/dC$ is negative. From Eq. (1), the variation of velocity with solute molarity can be expressed as

$$\frac{dv}{dC} = \frac{v}{2}\left(\frac{1}{\rho}\cdot\frac{d\rho}{dC} + \frac{1}{\beta}\cdot\frac{d\beta}{dC}\right) \quad \ldots(8)$$

Since the negative value of $\frac{1}{\beta}\cdot\frac{d\beta}{dC}$ is greater than $\frac{1}{\rho}\cdot\frac{d\rho}{dC}$, the value of $\frac{dv}{dC}$ is positive. R is, however, independent of temperature.

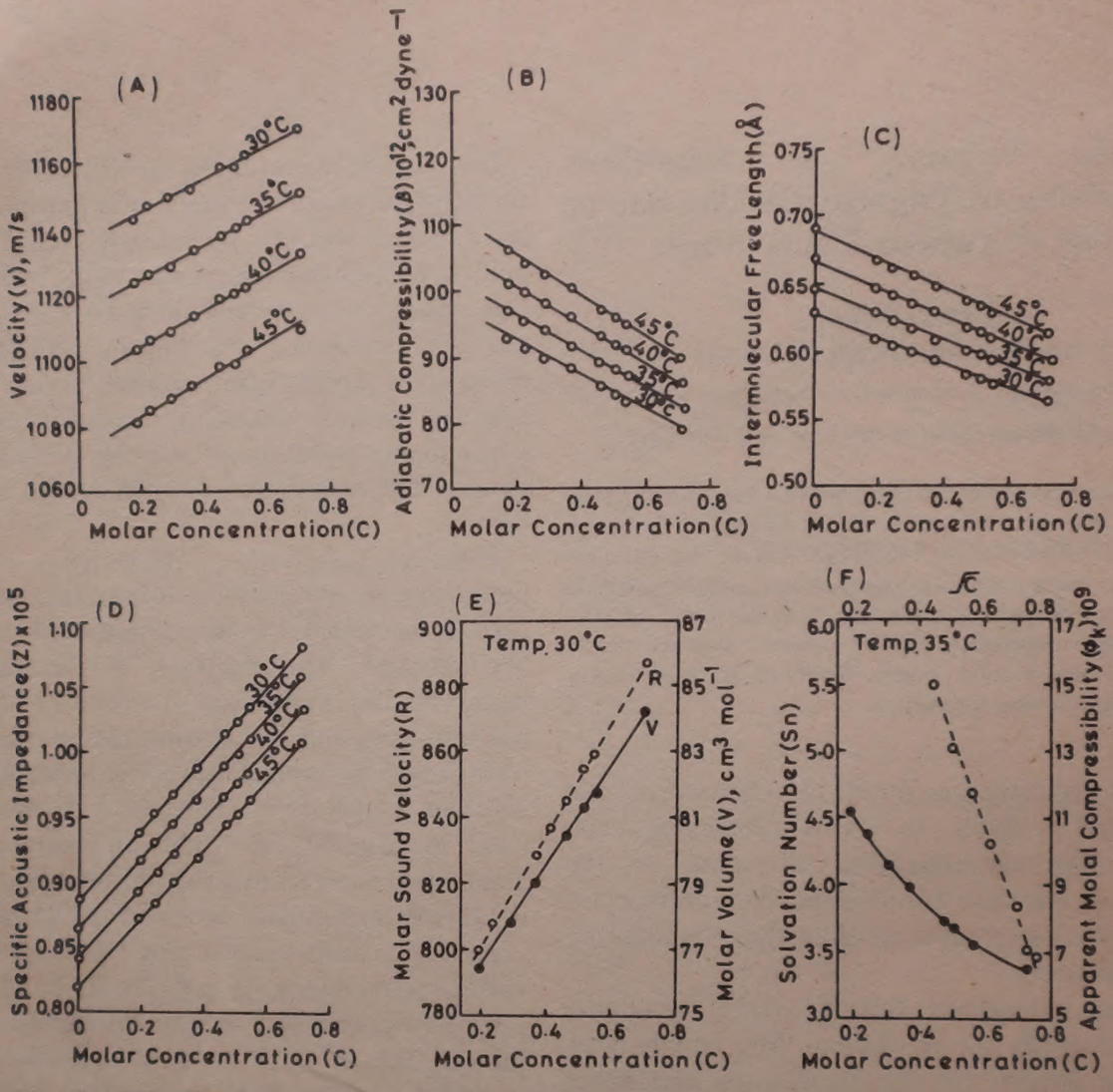

Fig. 1[(A)-(F)]—The molar concentration (C) of Ph_3SnCl versus the various ultrasonic parameters: (A) the ultrasonic velocity (v); (B) the adiabatic compressibility (β); (C) the intermolecular free length (L_f); (D) the specific acoustic impedance (Z); (E) the molar sound velocity (R) and the molar volume (V); and (F), C versus solvation number (S_n) and $\sqrt{C}$ versus apparent molal compressibility (φ_K)

With increase of temperature v decreases due to increase in L_f and average kinetic energy as reported by Mednis[7]. The values of β, L_f, φ_K and S_n also increase while those of Z decrease with the increase of temperature. R is approximately constant and is independent of temperature.

One of the authors (RPS) is thankful to the University Grants Commission, New Delhi for awarding him a teacher research fellowship.

References

1 Prakash O & Prakash S, *J Acoust Soc India*, **6** (1978) 11, 39.
2 Marks G W J, *J Acoust Soc Am (USA)*, **31** (1959) 936.
3 Jacobson B, *Acta Chem Scand (Denmark)*, **6** (1952) 1485.
4 Kocheshkov K A, Nad M M & Aleksandrov A P, *Chem Ber (Germany)*, **67** (1934) 1348.
5 Weissberger A, *Techniques of organic chemistry*: Vol. 7 (Interscience, New York), 2nd Edn, 1959.
6 Eyring H & Kincaid J F, *J Chem Phys (USA)*, **6** (1938) 620.
7 Mednis L, *Akust Zh (USSR)*, **13** (2) (1967) 24.

THE WEALTH OF INDIA

An Encyclopaedia of Indian Raw Materials and Industrial Products, published in two series: **(i) Raw Materials**, and **(ii) Industrial Products**.

RAW MATERIALS

The articles deal with Animal Products, Dyes & Tans, Essential Oils, Fats & Oils, Fibres & Pulps, Foods & Fodders, Drugs, Minerals, Spices & Flavourings, and Timbers and other Forest products. Names in Indian languages, and trade names are provided.

For important crops, their origin, distribution, evolution of cultivated types, and methods of cultivation, harvesting and storage are mentioned in detail. Data regarding area and yield and import and export are provided. Regarding minerals, their occurrence and distribution in the country and modes of exploitation and utilization are given. The articles are well illustrated. Adequate literature references are provided.

Eleven volumes of the series covering letters A – Z have been published.

Vol. I(A-B) Rs. 80.00; Vol. II (C) Rs. 95.00; Vol. III (D-E) Rs. 40.00; Vol. IV (F-G) Rs. 65.00; Vol. IV: Suppl. Fish & Fisheries Rs. 40.00; Vol. V (H-K) Rs. 75.00; Vol. VI (L-M) Rs. 60.00; Vol. VI: Suppl. Livestock Rs. 60.00; Vol. VII (N-Pc) Rs. 30.00; Vol. VIII (Ph-Re) Rs. 86.00; Vol. IX (Rh-So) Rs. 104.00; Vol. X (Sp-W) Rs. 152.00; Vol. XI (X-Z) Rs. 102.00.

INDUSTRIAL PRODUCTS

Includes articles giving a comprehensive account of various large, medium and small scale industries. Some of the major industries included are: Acids, Carriages, Diesel Engines, Fertilizers, Insecticides & Pesticides, Iron & Steel, Paints & Varnishes, Petroleum Refining, Pharmaceuticals, Plastics, Ship & Boat-building, Rubber, Silk, etc.

The articles include an account of the raw materials and their availability, manufacturing processes, and uses of products, and industrial potentialities. Specifications of raw materials as well as finished products and statistical data regarding production, demand, exports, imports, prices, etc., are provided. The articles are suitably illustrated. References to the sources of information are provided.

Nine volumes of the series covering letters A – Z have been published.

Part I (A-B) Rs. 54.00; Part II (C) Rs. 64.00; Part III (D-E) Rs. 25.00; Part IV (F-H) Rs. 25.00; Part V (I-L) Rs. 30.00; Part VI (M-Pi) Rs. 28.00; Part VII (Pl-Sh) Rs. 60.00; Part VIII (Si-Ti) Rs. 66.00; Part IX (To-Z) Rs. 80.00.

HINDI EDITION: BHARAT KI SAMPADA—PRAKRITIK PADARTH

Vols. I to VI and two supplements of Wealth of India—Raw Materials series in Hindi already published.

Published Volumes:

Vol. I (अ-औ) Rs. 38; Vol. II (क) Rs. 36; Vol. III (ख-न) Rs. 36; Vol. IV (प) Rs. 83; Vol. V (फ-मेरे) Rs. 60; Vol. VI (मेल-ह) Rs. 80.

Supplements:

Fish & Fisheries (Matsya & Matsyaki) Rs. 49; Liverstock (*Pashudhan aur Kukkut Palan*) Rs. 34.

Vols. VII to XI under publication.

Please contact:

Manager (Sales & Advertisement)

PUBLICATIONS & INFORMATION DIRECTORATE, CSIR

Hillside Road, New Delhi 110012

RN 7092/63

CSIR PUBLICATIONS

WEALTH OF INDIA

An encyclopaedia of the economic products and industrial resources of India issued in two series

RAW MATERIALS SERIES—contains articles on plant, animal and mineral resources

	Rs	$	£
Vol. I (A-B)	80.00	30.00	13.00
Vol. II (C)	95.00	33.00	17.00
Vol. III (D-E)	40.00	12.00	4.00
Vol. IV (F-G)	65.00	27.00	12.00
Supplement (Fish & Fisheries)	40.00	16.00	7.00
Vol. V (H-K)	75.00	28.00	12.50
Vol. VI (L-M)	90.00	34.00	15.00
Supplement (Livestock)	60.00	18.00	6.00
Vol. VII (N-Pe)	30.00	9.00	3.00
Vol. VIII (Ph-Re)	86.00	32.00	14.00
Vol. IX (Rh-So)	104.00	35.00	19.00
Vol. X (Sp-W)	152.00	65.00	23.00
Vol. XI (X-Z)	102.00	42.00	20.00

INDUSTRIAL PRODUCTS SERIES—deals with major, small-scale and cottage industries

Part I (A-B)	54.00	20.00	9.00
Part II (C)	64.00	24.00	11.00
Part III (D-E)	25.00	7.50	2.50
Part IV (F-H)	25.00	7.50	2.50
Part V (I-L)	30.00	9.00	3.00
Part VI (M-Pi)	28.00	8.00	2.80
Part VII (Pl-Sh)	60.00	18.00	6.00
Part VIII (Si-Ti)	66.00	27.00	10.00
Part IX (To-Z)	80.00	34.00	12.00

BHARAT KI SAMPADA (Hindi Edition of Wealth of India, Raw Materials):

Vol. I	(अ-औ)	38.00	16.00	6.50
Vol. II	(क)	36.00	15.00	6.00
Vol. III	(ख-न)	36.00	15.00	6.00
Vol. IV	(प)	83.00	34.00	16.00
Vol. V	(फ-मेरे)	60.00	22.00	10.00
Vol VI	(मेल-ह)	80.00	27.00	13.00
Livestock (Kukkut Palan)		34.00	15.00	6.00
Fish & Fisheries (Matsya aur Matsyaki)		49.00	21.00	8.00

A Dictionary of Generic & Specific Names of Plants and Animals Useful to Man with their English and Latin pronunciation in Devanagari — 30.00 | 11.00 | 5.00

OTHER PUBLICATIONS

	Rs	$	£
Proceedings seminar on primary communications in Science & Technology in India by Sh. R.N. Sharma & S. Seetharama	52.00	17.50	9.00
Flora of Delhi by J.K. Maheshwari	28.00	8.00	2.80
Indian Fossil Pteridophytes by K.R. Surange	23.00	8.00	2.30
Indian Thysanoptera by T.N. Ananthakrishnan	26.00	8.00	2.60
The Millipede Thyropygus by G. Krishnan	12.00	3.50	1.20
Drug Addiction with special reference to India by R.N. Chopra & I.C. Chopra	12.00	3.50	1.20
Glossary of Indian Medicinal Plants by R.N. Chopra & I.C. Chopra	35.00	13.00	6.00
Fluidization & Related Processes	12.00	4.00	1.20
Evolution of Life by M.S. Randhawa, A.K. Dey, Jagjit Singh & Vishnu Mitre	22.50	7.00	2.25
Collected Scientific Papers of Meghnad Saha	30.00	9.00	3.00
Proteaceae by C. Venkata Rao	34.00	11.00	3.40
Pinus by P. Maheshwari & R.M. Konar	30.00	11.00	5.00
Cellulose Research I	3.00	0.90	0.30
Cellulose Research II	6.00	1.75	0.60
Chemical Process Design	9.00	2.50	0.90
Low Temperature Carbonization of Non-coking Coals & Lignites & Briquetting Coal Fines:			
Vol. I	17.50	5.50	1.75
Vol. II	17.50	5.50	1.75
Nucleic Acids	10.00	3.00	1.00
IGY Symposium: Vol. I	9.00	2.50	0.90
IGY Symposium: Vol. II	9.00	2.50	0.90
CNS Drugs	16.50	5.00	1.65
Kinetics of Electrode Processes & Null Points of Metals	2.50	0.75	0.25
Indian Sardines by R.V. Nair	22.00	7.00	2.20
Termite Problems in India	9.00	3.00	0.90
Loranthaceae by B.M. Johri & S.P. Bhatnagar	32.00	11.00	3.20
Abies and Picea by K.A. Chowdhury	14.00	6.00	2.10
Gnetum by P. Maheshwari and Vimla Vasil	20.00	6.00	2.00
Aquatic Angiosperms by K. Subramanyam	20.00	6.00	2.00
Supplement to Glossary of Indian Medicinal Plants by R.N. Chopra, I.C. Chopra & B.S. Varma	18.00	7.00	3.00
Herbaceous Flora of Dehra Dun by C.R. Babu	144.00	60.00	22.00
Diosgenin and Other Steroid Drug Precursors by Y.R. Chadha & Miss L.V. Asolkar	36.00	13.00	6.00
Research & Development Management by Inder Dev	25.00	10.00	—
Rural Development and Technology—A Status Report-cum-Bibliography by P.R. Bose & V.N. Vashist	100.00	38.00	17.00

Packing and Postage extra

Please contact:

Manager (Sales & Advertisement)
PUBLICATIONS & INFORMATION DIRECTORATE, CSIR
Hillside Road, New Delhi 110012

Printed & Published by D.S. Sastry, Editor, Publications & Information Directorate (PID) Hillside Road, New Delhi 110012, at PID Photocomposition Unit

D(C)540